Stochastic trajectory modelling of atmospheric dispersion

by

Nurul Huda Mohd. Ramli

A thesis submitted in conformity with the requirements for the degree of Doctor of Philosophy.

Department of Mathematics
Faculty of Mathematical & Physical Sciences
University College London

September, 2016

Disclaimer

I, Nurul Huda Mohd. Ramli, confirm that the work presented in this thesis is my own. Where information has been derived from other sources, I confirm that this has been indicated in the thesis.

Signature _____

Date _____

Abstract

The stochastic trajectory-based (Lagrangian) approach has gained increasing importance and sophistication in atmospheric transport and dispersion modelling over the last few decades. State-of-the-art Lagrangian particle dispersion model (LPDMs) are used to compute trajectories of a large number of 'marked' particles and numerically simulate the dispersion of a pollutant (passive tracer) in the turbulent atmosphere. In this thesis, we mainly investigate the stochastic formulation and behaviour of LPDMs in the context of the turbulent atmospheric boundary layer (ABL).

A random flight model (RFM) is a type of LPDM that describes the paths of particles of an air pollutant in a turbulent flow, given a statistical knowledge of the random velocity field. Operational RFMs such as FLEXPART have not taken advantage of modern developments of numerical methods for stochastic differential equations. Chapter 2 of this thesis aims to determine whether current numerical schemes used in operational atmospheric dispersion modelling can be improved. Several commonly used numerical schemes are investigated in a simple one-dimensional dispersion model describing the vertical turbulence in the ABL. Eulerian Fokker-Planck equation (FPE) solutions with the required level of accuracy are used to validate the performance of the RFM numerical schemes. The results allow for optimal time-step selection and recommendations to be made for use in operational models.

RFMs are known to have a finite Lagrangian decorrelation time. Another class of LPDMs are the random displacement models (RDMs), which are essentially the zero decorrelation time limit of the RFMs. In Chapter 3, the problem of shear dispersion in the ABL is revisited, with the aim to improve understanding of how and why the behaviour of RFMs can differ to the RDMs. First, the effective horizontal diffusivity is examined for a tracer in the long-time dispersion in the RFM. Second, with 'poison gas release' problems in mind, a large-deviation approach is used to understand in greater detail the behaviour of the concentration in the tails of the distribution. Results are verified by solving the LPDM equations numerically for a large ensemble of particles.

Chapter 4 discusses methods of kernel density estimation for the optimal construction of particle concentration fields from the trajectory distributions. We demonstrate these methods on a two-dimensional advection-diffusion model (equivalent to the RDM) in a chaotic advection flow. Some well-known techniques of bandwidth selection are briefly discussed and a new approach in constructing a kernel density estimator is developed.

Primary Supervisor: Prof. J. G. Esler
Secondary Supervisor: Prof. E. R. (Ted) Johnson

Acknowledgments

Well I finally made it! A lot of credits goes to my supervisor, Prof. Gavin Esler for his constant support, guidance and encouragement over the course of my PhD. His enthusiasm and expertise have enabled me to study a great research topic. I am very grateful for his enormous patience on the many occasions I walked in to his office and asked a stupid question, and also for his thorough explanations that never fail to point me in the right direction.

I would like to take this opportunity to also thank the lovely members of staff at the UCL Mathematics department for the interesting discussions and support. I also thank UBD Chancellor's scholarship and UCL Studentship for their financial support which have made my studies possible.

Many thanks to my ayah and babu for being the most wonderful parents who always support my dreams and for their guidance and faith. Special thanks go to my boyfriend Youcef for putting up with my (healthy) amount of PhD stress and also for providing emotional support whenever needed and for always believing in me.

Last but not least, a big shout out to my PhD colleagues and friends that have made my four years of PhD an enjoyable experience. Special mention goes to the "KLB survivors" including Adam, Ali, Anna, Belgin, Doaky, Gin, Mart, Olly, Peter (who?), Pietro, Rafael, Rudie, Sam, Scroggs and KLB Scroggsbot. Thank you for the good times and see you all in the next KLB field trip!

Contents

List of Tables

List of Figures

Chapter 1

Introduction

Overview: This introductory chapter provides the reader with an overall view of this thesis. An overview of a simple atmospheric dispersion problem is sketched, as well as the two basic types of reference frames to look at it. More emphasis will be put on the Lagrangian perspective, when Lagrangian models are used and why they are needed. Next a brief mathematical introduction to the theory of stochastic differential equations (SDEs) is given, including the complementary probabilistic approach to stochastic processes represented by Fokker-Planck equation and its relatives. An introduction to the two basic types of Lagrangian stochastic models used to simulate dispersion in the turbulent ABL follows, namely random flight models (RFMs) and random displacement model (RDMs), as well their formulation. After that we take a closer look at why the two models are useful and what flow situations they could be used for. Finally the concept of variance reduction for rare-events in stochastic simulations are briefly discussed, most notably on the splitting method known as Go-with-the-winners (GWTW). The scope of the research will be briefly discussed, and to conclude the chapter an outline for the rest of the thesis will be given.

1.1 The atmosphere

The earth's atmosphere consists of a number of layers, that differ according to the air constituents and temperature profiles (i.e. stratification). Figure 1.1 shows a plot of how the temperature varies with height altitude in the atmosphere. In general, the air grows progressively less dense as we move upward from the troposphere through the stratosphere and the mesosphere to the thermosphere. In the upper reaches of the thermosphere, the air is extremely thin with gas molecules being separated from each other by large distances as compared with the troposphere. Atmospheric dispersion models are mainly used in the troposphere and stratosphere, and are particularly important in the atmospheric boundary layer where three-dimensional turbulence is most prevalent.

1.1.1 Atmospheric boundary layer

The atmospheric boundary layer (ABL) is defined as *"the part of the troposphere that is directly influenced by the presence of the earth's surface, and responds to surface forcings with a timescale of about an hour or less"* (Stull, 1988). Its depth is typically less than 1 km and varies depending on the local meteorology. Turbulence is ubiquitous within the boundary layer and is responsible for efficiently dispersing pollutants and other constituents of the atmosphere. Therefore it plays a crucial role in modulating the weather (temperature, humidity, wind strength, air quality, etc) that we see and experience on the surface.

Turbulence in the ABL can be visualised in the form of irregular swirls called eddies. These eddies have two primary causes: mechanical and thermal, which determine the structure of the ABL, that itself evolves with the diurnal (daily) cycle. Large eddy thermals consists of warm air that rises and cold air to sink due to buoyancy forces, for example from solar heating of the ground during sunny days. Mechanical eddies are generated by wind shear, which can be caused by frictional

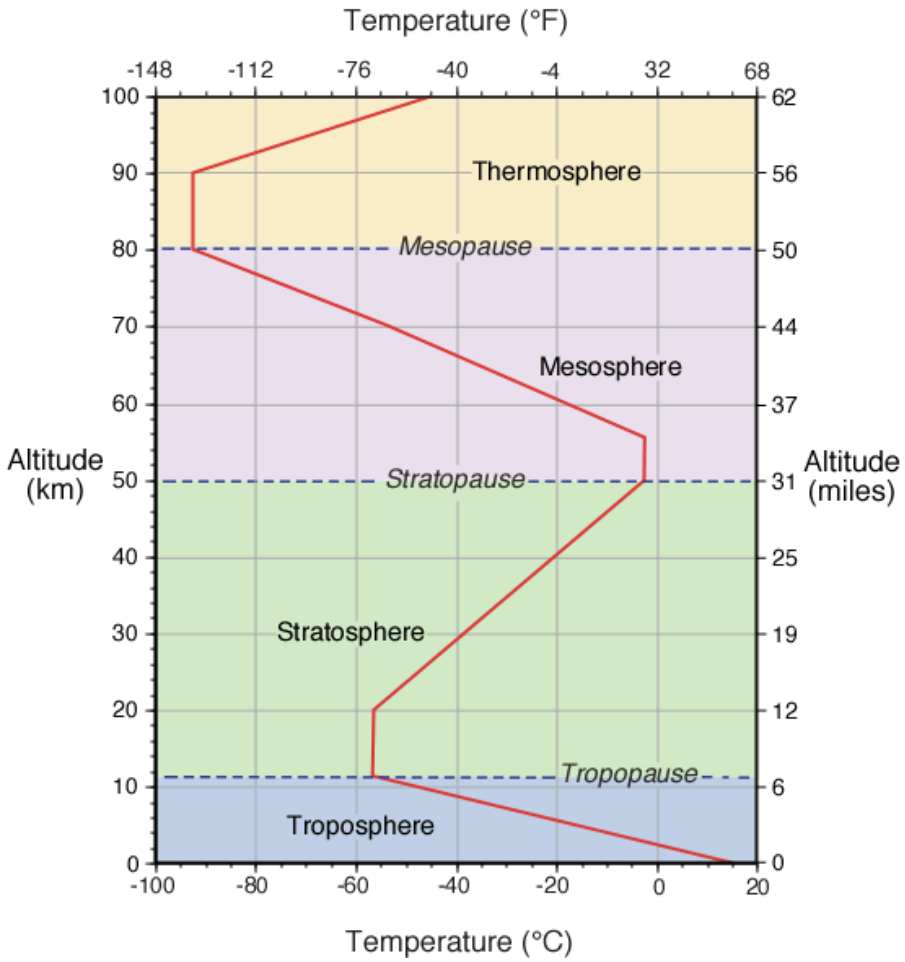

Figure 1.1: Vertical change in average global atmospheric temperature. Variations in the way temperature changes with height indicates the atmosphere is composed of four different layers as labeled above. (Source: PhysicalGeography.net)

drag on the surface roughness of the ground or turbulent wakes from obstacles that deflect the flow, such as trees and buildings. Mechanical turbulence can also take place even if the air is in stable stratification due to the dynamically unstable flow causing the formation and breakdown of waves in the air known as Kelvin-Helmholtz waves. In addition, ABL turbulence may also interact with a large-scale mean flow that is influenced by the Earth's rotation or Coriolis force.

Over land surfaces in particular, the ABL turbulence has a well defined structure influenced by the diurnal cycle of surface heating and cooling, and the presence of clouds. The typical diurnal cycle of the ABL over land is illustrated in Figure 1.2. The three major components of the ABL can be summarised in the following

(i) *Unstable* conditions occur in the daytime when there is strong surface heating from the sun, which produces thermal instability or convection in the form of vigorous thermal updrafts and downdrafts. The region which is strongly dominated by convective motions is often referred to the convective boundary layer or mixed layer. The stable layer at the top, called entrainment zone acts as a lid to the rising thermals and thus restrains the domain of turbulence.

(ii) In contrast, the *stable* conditions occur mostly at night, the turbulence level decrease with height in response to the surface cooling. The top of the stable ABL, $z = h$ is not as sharply defined as the top of the convective layer, but there is a general agreement that h should be the height where turbulence drops to negligible levels.

(iii) In the absence of thermal processes, the ABL is said to be *neutral* which takes place in windy conditions with a complete cloud cover. This condition is sometimes referred to as the Ekman ABL because of the zero buoyancy effects and the dominant turbulence are driven by the frictional and Coriolis forces (see for e.g. §2.12 of Vallis, 2006).

As mentioned above, this chapter serves to provide the reader an overall sketch of

the main motivations of this thesis. More comprehensive descriptions of the ABL physical turbulence and flows can be found in the books of Stull (1988); Garratt (1994); Kaimal and Finnigan (1994).

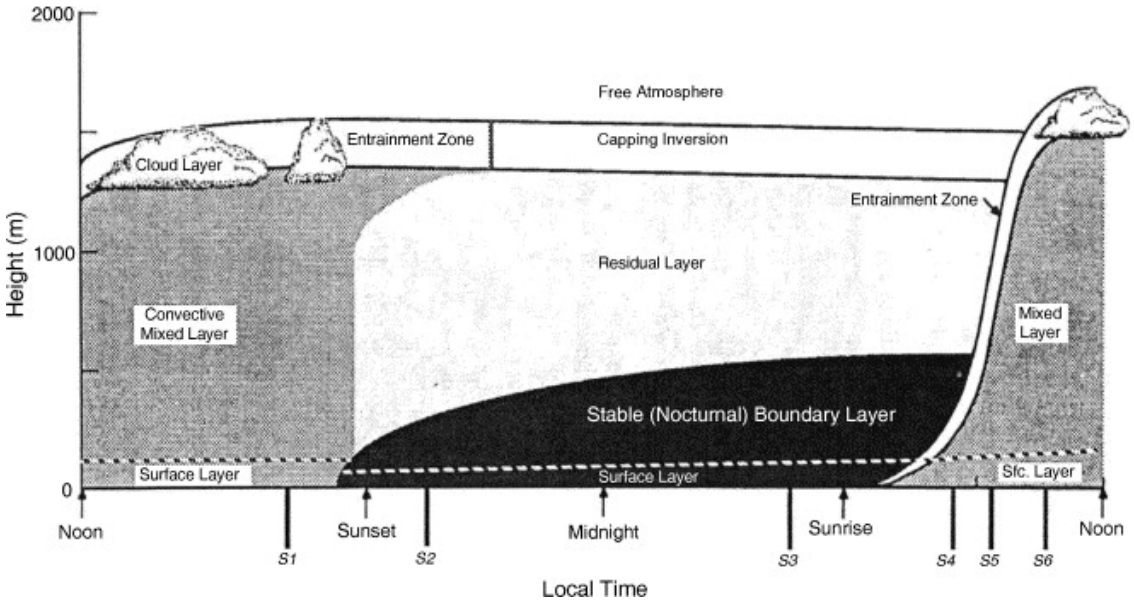

Figure 1.2: Well defined structure of the atmospheric boundary layer in the typical diurnal cycle, adapted from Stull (1988, Fig. 1.7).

1.1.2 Atmospheric dispersion models

Atmospheric dispersion modelling refers to the mathematical description for the transport of particulates or air pollutants in the atmosphere. The term dispersion is used to describe the combination of diffusion (due to turbulent eddy motion) and advection (due to the wind) that occurs near the Earth's surface.

Many models have been developed to stimulate large-scale transport of atmospheric tracers, with a number of potential practical applications at very different scales. These studies are highly significant in efforts of protecting and managing the ambient air quality. An important application of these models is the forecast of volcanic ash clouds in the atmosphere which is vital in the efforts to control air

traffic after major volcanic eruptions. Some examples of these events include Icelandic Grimsvötn volcano (e.g. Witham et al., 2007), Mount Okmok and Kasatochi (D'Amours et al., 2010) in the United States, Icelandic Eyjafjallajökull (e.g. Langmann et al., 2012; Devenish et al., 2011), and more recently, the eruptions of 2014 Mount Sinabung in Indonesia and 2016 Calbucco in Chile. Other important motivations for the development of atmospheric models were the nuclear reactor accidents of the 1986 Chernobyl (Hiroaki and Masamichi, 2008) and the 2011 Fukushima Daiichi (Stohl et al., 2012), which highlighted the need to be able to estimate long-range transport and dispersion in a timely and flexible way.

In recent years, trajectory modelling of atmospheric dispersion, often referred to as Lagrangian particle dispersion models (LPDMs, hereafter) have become increasingly important owing to its simplicity in concept and applicability to complex problems in which more conventional approaches cannot be applied, e.g. Gaussian puff models describing plume dispersion (Weil and Brower, 1984). The stochastic technique is typically implemented in the form of a numerical Monte Carlo method, which uses a large number of hypothetical particles to simulate the transport and dispersion of atmospheric pollutants. The particles are continuously traced in time and space and their population represents the plume structure. Because particle paths are computed independently, Lagrangian simulations can be parallelised with minimal effort. LPDMs are the natural and most powerful tool to describe a wide range of atmospheric dispersion events. Some examples of widely used LPDMs include FLEXible PARTicle dispersion (FLEXPART) model (Stohl et al., 2005), and Stochastic Time-Inverted Lagrangian Transport (STILT) model (Lin et al., 2003). Some models even have hybrid capabilities that combine plume and particle characteristics, such as the UK Met Office's Numerical Atmospheric dispersion Modelling Environment (NAME) (Jones et al., 2007), and TAPM (Hurley et al., 2005).

In the present day, state-of-the-art LPDMs are used in transport and dispersion applications ranging from micrometeorological to global scales. A few examples of

LPDM applications have already been mentioned above, namely predicting the hazards of volcanic ash clouds (Stohl et al., 2011; Devenish et al., 2011; D'Amours et al., 2010) and modelling of nuclear accident scenarios (Stohl et al., 2012). Other variants of the LPDMs are also applied in atmospheric dispersion areas, such as establishing the relationship between emissions of pollutants and air quality downstream (Cassiani et al., 2012), the determination of constraints on chemical emissions via inverse modelling (Seibert and Frank, 2004; Stohl et al., 2010), modelling concentration fluctuations for e.g. through micromixing techniques (Cassiani et al., 2005), and non-passive tracers; such as buoyant plumes (Das and Durbin, 2005) and heavy gases (Anfossi et al., 2010). More fundamentally, applications of LPDMs have been extended from air pollution studies to other topics that are used to address key scientific questions concerning the nature of transport in the atmosphere such as the exchange between the troposphere and stratosphere (Legras et al., 2005; Berthet et al., 2007), including how transport might be influenced by a changing global climate (James et al., 2003a,b). Recently, the model NAME has been used to model the dispersion of wind-borne viruses such as the Bluetongue and Schmallenberg viruses, which are believed to be spread by midges (UK Met Office).

In this study, we will restrict to models of passive material, i.e. neutrally buoyant and non-reactive tracer particles. We have preferred to focus on the Lagrangian modelling of the short range transport (order of ≤ 100 km) of passive tracer in the ABL where the turbulence is inhomogeneous (in the vertical direction z, if not in x and y), possibly non-stationary, and characterised by having a large Reynolds number, $\mathrm{Re} = Uh/\nu$ (where U is a characteristic velocity, h is the ABL height, and ν is the kinematic viscosity of air).

1.1.3 Lagrangian perspective and its advantages

The concentration of a passive tracer $c(\boldsymbol{x}, t)$ released into the air may therefore be described by the advection-diffusion equation, which is a second-order partial differential equation (PDE, hereafter) of parabolic type, which has the form

$$\frac{\partial c}{\partial t} + (\boldsymbol{u} \cdot \nabla)\, c - \nabla \cdot (\boldsymbol{\kappa} \cdot \nabla c) = s(\boldsymbol{x}, t). \tag{1.1}$$

Here $\boldsymbol{u}(\boldsymbol{x}, t)$ is a known smooth incompressible velocity field, $\boldsymbol{\kappa}(\boldsymbol{x}, t)$ is a symmetric diffusivity tensor and $s(\boldsymbol{x}, t)$ a source term. There are generally two different methods of solving this dispersion problem: Eulerian and Lagrangian. The Eulerian solves eq. (1.1) directly on a fixed spatial grid, using deterministic numerical methods (e.g. finite element, finite difference and spectral methods). The Lagrangian method on the other hand follows the trajectories of particles through space at every time step (using stochastic methods or Monte-Carlo simulations), and allows observation of fluctuations in the path of the particles. Figure 1.3 depicts a schematic example of the Eulerian (left panel) and Lagrangian (right panel) methods of a fluid flow in the numerical model.

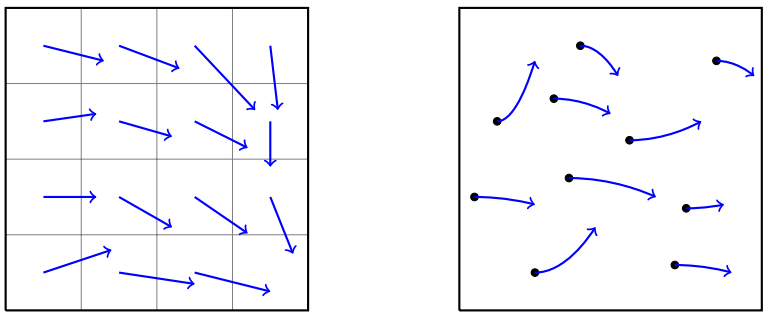

(a) Eulerian (b) Lagrangian

Figure 1.3: Representative examples of the frame of reference using **(a)** the grid-based Eulerian model, and **(b)** particle tracking in the Lagrangian model.

Air parcels simulation in Lagrangian models is the most natural way for dealing with atmospheric flows, as the air in the atmosphere is comprised of molecules being transported. The availability of trajectory information from Lagrangian simulations may serve as key knowledge in addressing scientific question, as illustrated throughout the literature (see the monograph of Lin et al., 2013, for examples). Also, the Lagrangian models offer several advantages over the Eulerian schemes. Among others (Lin et al., 2013), these advantages include:

1) Lagrangian models are computational efficient, especially for problems where the tracer does not occupy the whole model domain (Spivakovskaya et al., 2005). Since the particles are independent, parallel computing can be used to increase efficiency.

2) In the Lagrangian model, since the movement of a constant total number of particles are tracked, mass conservation follows automatically. While Eulerian schemes may not conserve mass (Brasseur et al., 1999).

3) Lagrangian schemes are numerically stable in which the integration time-step is to be determined by accuracy considerations alone. On the other hand Eulerian schemes operate with a necessary limitation of the largest time-step for stability, i.e. the Courant-Friedrichs-Lewy criterion (Courant et al., 1967).

4) The advection step in Eulerian schemes tend to smooth out scalar gradients due to limited grid resolution and inevitable artificial numerical diffusion (Wohltmann and Rex, 2009). By contrast in the grid-less Lagrangian advection step, numerical diffusion is minimized and steep gradients in tracer concentrations are preserved.

A shortcoming of Lagrangian models is that, because particle represent fixed masses of tracer, an additional procedure in reconstructing from particle distribution to concentration field is required. Established methods in statistics include the kernel density estimation (see for e.g. Silverman, 1986; Wand and Jones, 1994),

where its applications in atmospheric problems are well-explored (e.g. Yamada and Bunker, 1988; Uliasz, 1994). The computational cost of Lagrangian models can also be significant, particularly when large particle ensembles are required to get an accurate estimate of the concentration. However with the advances in computer technology and the possibilities of efficient parallel computing today, this is becoming less and less of a problem as better strategies are being developed to overcome these drawbacks.

1.2 Background to stochastic differential equations

Lagrangian models are formulated using stochastic differential equations (SDEs, hereafter). For example, a one-dimensional SDE can be written in the form

$$\mathrm{d}X_t = a(X_t, t)\,\mathrm{d}t + b(X_t, t)\,\mathrm{d}B_t, \tag{1.2}$$

where X_t is a stochastic variable, $a(X_t, t)$ and $b(X_t, t)$ are arbitrary functions. The function $a(X_t, t)$ represents a deterministic or averaged drift term, and $b(X_t, t)$ is (generally) a space-time dependent intensity for the noisy, diffusive term. A thorough introduction to the theory of stochastic calculus can be found in Øksendal (2007, §§2-4) and Kloeden and Platen (1992, §§2-3) and in the context of our mathematical modelling, we briefly outline the random term B_t, known as the Brownian motion (sometimes called Wiener process).

Brownian motion is a term (named after Robert Brown, in 1827) used to describe the phenomenon of the erratic motion of a grain of pollen on a water surface due to its being continually bombarded by water molecules. Wiener process was named after Norbert Wiener, who developed a formal mathematical description of

the continuous-in-time stochastic process behind this phenomenon. In general, a standard Brownian motion (or Wiener Process) B_t has the following properties:

(i) $B_0 = 0$; with probability 1,

(ii) $\langle B_t \rangle = 0$,

(iii) $\mathrm{Var}(B_t - B_s) = t - s$,

for all $0 \leq s \leq t$, where $\langle \cdot \rangle$ denotes the average mean or expectation value. B_t can be described as a Markov process, which is defined as a stochastic process that has zero memory of the past and a future that is a function of the present and some statistical rule for the transition. Therefore it follows that the increments of the Brownian motion, $\mathrm{d}B_t$ are jointly independent and that $\mathrm{d}B_t \sim (\mathrm{d}t)^{1/2}$.

The SDE (1.2) can be re-written as a stochastic integral equation

$$X_t = X_{t_0} + \int_{t_0}^{t} a(X_s, s)\,\mathrm{d}s + \int_{t_0}^{t} b(X_s, s)\,\mathrm{d}B_s, \quad \text{for } \; 0 \leq t_0 \leq t \leq \infty. \tag{1.3}$$

The first integral on the right-hand side is a regular Riemann-Stieltjes integral and the second is a so-called stochastic integral, which can be interpreted in many ways. The two most studied interpretations of the evaluation of this integral are those of Itô (1951) and Stratonovich (1967). For example in the one-dimensional case, assume $\langle |b(x,t)|^2 | \rangle < \infty$ for all $t \in [0, T]$ and let $\mathcal{P}$ be a partition of $[0, T]$, where $0 = t_0 < t_1 < \ldots < t_n = T$. The stochastic integral can be defined as the mean square limit

$$\int_{\mathcal{P}} b(x,t)\,\mathrm{d}B_t = \lim_{\Delta t \to 0} \sum_{i=0}^{n-1} b(x, s_i)\left(B_{t_{i+1}} - B_{t_i}\right), \tag{1.4}$$

with $\Delta t = \max_i(t_{i+1} - t_i)$ and $s_i \in [t_i, t_{i+1}]$. The limit that defines the integral depends on where s_i is taken to lie in interval $[t_i, t_{i+1}]$, and this leads to the two

different stochastic calculi:

$$\begin{aligned} \text{Itô calculus:} \qquad & s_i = t_i \\ \text{Stratonovich calculus:} \qquad & s_i = \tfrac{1}{2}\left(t_i + t_{i+1}\right) \end{aligned}$$

It turns out that the Itô sense provides the easiest way for theoretical calculations because we can obtain simple formulas for the first two moments of the Itô integral and the SDE based on the integral yields a diffusion process as a solution (Arnold, 1974). Practical numerical calculations involving increments Δt and ΔB_t are also simpler with the Itô integral. For these reasons we will only concern ourselves with Itô processes in this thesis and thus assume that all the SDEs considered here-in-after are Itô.

1.2.1 Itô's formula

More importantly, a result that follows from the so-called chain rule for Itô calculus in finding the derivative of a given (smooth) function $f(X_t, t)$ of a random variable X_t, is the Itô's lemma or Itô's formula.

Lemma 1.2.1 (Itô's formula) *Assume that X_t is a drift-diffusion process satisfying the Itô process*

$$dX_t = a(X_t, t)\, dt + b(X_t, t)\, dB_t,$$

and $f(X_t, t)$ is a twice-differentiable function, then

$$df(X_t, t) = \left(\frac{\partial f}{\partial t} + a\,\frac{\partial f}{\partial x} + \frac{1}{2}b^2\,\frac{\partial^2 f}{\partial x^2}\right)\Bigg|_{(X_t,t)} dt + \left(b\,\frac{\partial f}{\partial x}\right)\Bigg|_{(X_t,t)} dB_t.$$

Naturally, this formula can be extended to higher dimensions in which an n-dimensional stochastic variable vector $\boldsymbol{X}_t$ satisfies the matrix-vector SDE system,

$$\mathrm{d}\boldsymbol{X}_t = \boldsymbol{a}(\boldsymbol{X}_t, t)\,\mathrm{d}t + \boldsymbol{b}(\boldsymbol{X}_t, t)\,\mathrm{d}\boldsymbol{B}_t, \tag{1.5}$$

where $\boldsymbol{a}(\boldsymbol{X}_t, t) = (a_1, \ldots, a_n)$ is the drift vector, $\boldsymbol{b}(\boldsymbol{X}_t, t)$ is an $n \times m$ diffusion matrix and $\boldsymbol{B}_t$ denotes an m-dimensional Brownian motion. Similar to Itô's formula for the one-dimensional example above, the multi-dimensional Itô's formula for a given function $f(\boldsymbol{X}_t, t)$ is

$$\mathrm{d}f(\boldsymbol{X}_t, t) = \left(\frac{\partial f}{\partial t} + \boldsymbol{a}^\dagger \nabla f + \frac{1}{2}\mathrm{Tr}\left(\boldsymbol{b}\,\boldsymbol{b}^\dagger\,(\nabla\nabla f)\right)\right)\,\mathrm{d}t + \left(\nabla f^\dagger\,\boldsymbol{b}\right)\,\mathrm{d}\boldsymbol{B}_t, \tag{1.6}$$

where "Tr" denotes the trace or sum of the diagonal components of the inscribed matrix. Details of the Ito's lemma derivation and justification can be found in the books of Kloeden and Platen (1992, §3.3) and Øksendal (2007, §4).

1.2.2 Fokker-Planck equation

The Fokker-Planck equation (FPE, hereafter) or sometimes known as the master equation (see Van Kampen, 2007; Gardiner, 2009, for e.g.), is an advection-diffusion type PDE that describes the time-evolution of the probability density function (PDF), $p(x,t)$ of a stochastic process X_t. Considering the one dimensional example above, where X_t satisfies the SDE (1.2), its transition probability density $p(x,t\big|x_0,t_0)$ is propagated according to the FPE

$$\begin{aligned} \frac{\partial p}{\partial t} &= -\frac{\partial}{\partial x}\left(a(x,t)\,p\right) + \frac{1}{2}\frac{\partial^2}{\partial x^2}\left(b^2(x,t)\,p\right), \\ p(x_0,t_0) &= \delta(x - X_0). \end{aligned} \tag{1.7}$$

More generally in the multi-dimensional case for example the SDE (1.5), the FPE for the PDF $p(\boldsymbol{x}, t)$ of the n-dimensional particle random displacements $\boldsymbol{X}_t$ is found to be

$$\frac{\partial p(\boldsymbol{x},t)}{\partial t} = -\sum_{i=1}^{n} \frac{\partial}{\partial x_i} \left(a_i(\boldsymbol{x},t)\, p(\boldsymbol{x},t)\right) + \frac{1}{2} \sum_{i=1}^{n}\sum_{j=1}^{n} \frac{\partial^2}{\partial x_i \partial x_j} \left(D_{ij}(\boldsymbol{x},t)\, p(\boldsymbol{x},t)\right), \quad (1.8)$$

where

$$D_{ij}(\boldsymbol{x},t) = \sum_{k=1}^{m} b_{ik}(\boldsymbol{x},t) b_{jk}(\boldsymbol{x},t),$$

is the diffusion tensor. Note that variations of the FPEs in more dimensions will provide similar results, see for e.g. Equation (1.24). In the language of statistics, an *invariant measure* of a stochastic process is a measure on $\mathbb{R}^n$ that does not change under the flow of the random variable. The FPE offers a way to find such a measure and in atmospheric applications, the invariant measure is simply the steady state solution of the FPE, i.e. $\partial p/\partial t = 0$.

In order to solve parabolic PDEs such as (1.1) using stochastic methods, one must find the *stochastic representation* of (1.1), which means finding the SDE which has the Fokker-Planck equation given by eq. (1.1). To provide the reader a clear understanding of this concept, we demonstrate the use of the FPE in a simple diffusion problem to follow.

1.2.2.1 A simple example

As an example, we show two different ways of solving a diffusion equation. Let's consider a simple one-dimensional diffusion only (no advection) model of a tracer cloud in a channel with a constant diffusion coefficient κ. The PDE describing the evolution of the tracer concentration, with initial condition $x = 0$ at time $t = 0$, is given by

$$\frac{\partial c}{\partial t} = \kappa \frac{\partial^2 c}{\partial x^2}, \quad \text{where} \quad c(x,0) = \delta(x). \quad (1.9)$$

This equation can be solved analytically, and the exact solution is known to be the heat kernel

$$c(x,t) = \frac{1}{\sqrt{4\pi\kappa\, t}} \exp\left(\frac{-x^2}{4\kappa\, t}\right), \tag{1.10}$$

assuming that the domain is infinite. This solution can also be obtained by

(i) numerically discretizing the diffusion eq. (1.9), or

(ii) using a stochastic approach.

For the stochastic method (ii) of this example, we look at the classical Brownian motion process which can be used to model diffusion as suggested by Einstein in 1905, where the particle positions are randomly disturbed as follows

$$\mathrm{d}X_t = \sigma\, \mathrm{d}B_t, \quad \text{where} \;\; X(0) = X_0. \tag{1.11}$$

Here $\mathrm{d}B_t$ is the increment of standard Brownian motion and σ is the constant diffusion term. The FPE (1.7) that describes the probability density $p(x,t)$ of the positions of particles evolving in time, is given by

$$\begin{aligned} \frac{\partial p}{\partial t} &= \frac{1}{2}\sigma^2 \frac{\partial^2 p}{\partial x^2}, \\ p(x,0) &= \delta(x - X_0). \end{aligned} \tag{1.12}$$

The concentration $c(x,t)$ can be described as the probability that a particle ends up in position x and time t, which is equivalent to the definition of the probability density $p(x,t)$. Substituting $\sigma = \sqrt{2\kappa t}$ and that $p(x,t) = c(x,t)$, it can be concluded that (1.12) describes the same diffusion process of eq. (1.9) and therefore they have the same solution

$$\begin{aligned} p(x,t) &= \frac{1}{\sqrt{2\pi\sigma^2}} \exp\left(\frac{-x^2}{2\,\sigma^2}\right), \\ &= \mathcal{N}(0,\sigma^2), \end{aligned} \tag{1.13}$$

with $\mathcal{N}(0, \sigma^2)$ being the normal distribution of mean zero and variance equatl to σ^2. It can be said that (1.11) is consistent with (1.9), with FPE (1.12) being the Eulerian alternative to the Lagrangian SDE (1.11).

1.3 Lagrangian particle dispersion models

As already noted above, LPDMs adopt the study of stochastic random motion of particles as they are advected by a given turbulent flow. For this reason the Lagrangian approach provides the most natural and simple way of formulating the turbulent dispersion in the ABL than the Eulerian approach. Rodean (1996) published a comprehensive monograph on LPDMs and another notable review written in the same year was by Wilson and Sawford (1996). Lagrangian modelling of mean dispersion in the turbulent ABL normally involves releasing a large number of particles corresponding to different flow realizations with suitable initial conditions, such as a point source. Throughout this thesis, we consider the so-called one-particle modelling, in which the motion of each particle is completely independent of that of other particles. The calculated trajectory distribution simulates the source plume and can be used to compute mean dispersion quantities, such as average concentration.

In this section, we give a detailed formulation of the two commonly used LPDMs in the context of the turbulent ABL. We use the acronyms RFM and RDM; for the random flight model and the random displacement model respectively. In the RDM, the particle trajectory is the vector sum of random incremental changes in displacement plus contributions from the mean wind. By contrast in the RFM, the stochastic incremental changes in particle velocity are integrated in time to define the particle trajectory in space. Note that higher order models in which the

stochastic incremental changes in acceleration are integrated to obtain velocity and displacement are not considered here. The random incremental changes in RDMs are a model for advection by the eddy field, which is unrealistic for times smaller than the Lagrangian velocity decorelation timescale. This motivates the introduction of RFMs, in which the random incremental changes capture a finite decorrelation time. Therefore RFMs give a more realistic representation of eddy velocities and they can be used to deal with more general initial conditions, e.g. plumes with non-zero initial velocities.

Before the early development of the LPDMs in the framework for turbulent dispersion, Taylor (1921) published his pioneering work presenting an exact Lagrangian solution for rate of spread of tracer in unbounded, stationary homogeneous turbulence. His analysis showed that the near-field (small time) behaviour of the root-mean-square particle displacement (as measured by the standard deviation of displacement) is proportional to travel time t, whereas the far-field (large time) behaviour is proportional to $t^{1/2}$. The latter represents the diffusive behaviour in which the size of the plume is larger than the size of the dominant turbulent eddies. Taylor's (1921) results therefore proves that the classic "eddy diffusion" paradigm based on the Fickian theory of molecular diffusion (equivalent to the RDM) are able to represent the far-field, but not the near-field in which the plume size is small compared to the size of the dominant turbulent eddies. In contrast, the RFM for an idealized field of homogeneous and stationary turbulence reproduces the analytical forms of both near- and far-field behaviours of tracer dispersions. Ever since its derivation, Taylor's (1921) result has served to guide turbulent dispersion modelling, however its scope for application to complex real-world flows was limited. See the work of Thomson and Wilson (2013) for a comprehensive account of the history of Lagrangian stochastic modelling for turbulent dispersion, where the authors discuss how the early computational LPDMs started to extend to non-idealized, non-stationary and inhomogeneous turbulence in the lower atmosphere.

1.3.1 The well-mixed criterion

The basis for the derivation and checking consistency of LPDMs in inhomogeneous turbulence (turbulence statistics depend on height) was first laid by Thomson (1987). Thomson demonstrated that the random forcing of the stochastic models must be Gaussian and developed a set of rigorous criteria that the LPDM must satisfy. Most importantly, he showed that if one of the criteria is satisfied the rest will be satisfied too. This criterion is known as the well-mixed condition (WMC, hereafter): *"if the particles are well-mixed in velocity-position space, they should remain so"* (Thomson, 1987).

In simple terms, the WMC means that in a bounded region away from the source, if the distribution of particles become well mixed, then it should remain so for all subsequent times. Particles are said to be well mixed when the joint distribution of the particles matches the assumed distribution for all the particles in the atmosphere in both position and velocity space. In probability terms, the invariant measure of the stochastic process should equal the pre-defined 'atmospheric' distribution of particles in the air, which is taken here to be homogeneous Gaussian distribution. An example of a well-mixed scenario in the ABL could be the steady stable boundary layer over the Antarctic Continent during the long winter nighttime where the diurnal cycle is absent (Garratt, 1994).

As will be seen below, Thomson's (1987) WMC leads to a unique one-dimensional LPDM, and provided the variables in each dimension are assumed to be independent of those in the other dimensions a unique three-dimensional model can be constructed too. However the WMC could also lead to a non-unique multi-dimensional solution if there is a dimensional interdependence of variables, and two distinct models satisfying the WMC with the same flow could yield significantly different dispersion predictions (Sawford and Guest, 1988).

1.3.2 Random flight model (RFM)

In the most general formulation of the RFM, the position and velocity $(\boldsymbol{X}_t, \boldsymbol{U}_t)$ of a particle in three-dimensional space $\boldsymbol{X}_t = (X_t, Y_t, Z_t)$ can be described by the following SDE

$$\mathrm{d}\boldsymbol{U}_t = \boldsymbol{a}(\boldsymbol{X}_t, \boldsymbol{U}_t, t)\ \mathrm{d}t + \boldsymbol{b}(\boldsymbol{X}_t, \boldsymbol{U}_t, t)\ \mathrm{d}\boldsymbol{B}_t, \tag{1.14}$$

where $\boldsymbol{a}$ is the drift term and $\boldsymbol{b}$ is the diffusion tensor. $\boldsymbol{U}_t$ is the turbulent velocity component at time t and $\boldsymbol{B}_t$ is the multi-dimensional Brownian motion (or Wiener process) with mean zero and variance $\mathrm{d}t$, with each component being independent of other components and uncorrelated in time. Simultaneous to (1.14), the particle positions are calculated from

$$\mathrm{d}\boldsymbol{X}_t = \boldsymbol{U}_t\ \mathrm{d}t. \tag{1.15}$$

As will be shown, the choice of $\boldsymbol{a}$ and $\boldsymbol{b}$ in (1.14) is restricted by the assumptions made about the pdf of $\boldsymbol{X}_t$ and $\boldsymbol{U}_t$ in the atmospheric background. Here we assume Gaussian turbulence, meaning that the background atmospheric distribution of air (known as the invariant measure in probability terms) is chosen to be Gaussian in this case. This model choice is strictly valid only for stable and neutral conditions, which are the two ABL profiles that will be considered in this thesis. Under convective (or unstable) conditions, turbulence is skewed and so this assumption is violated (Cassiani et al., 2015).

As often presented in atmospheric dispersion models, it is assumed that changes of flow properties in the horizontal and in time are sufficiently slow and therefore can be neglected. For this reason and for the purpose of derivation of the Lagrangian models in this section, we will consider only one-dimensional dispersion in the vertical motion (Z_t, W_t).

As a starting point, consider the homogeneous isotropic Gaussian turbulence

where the Langevin equation describes the vertical velocity W_t at time t is given by

$$\mathrm{d}W_t = -\frac{W_t}{\tau_w}\,\mathrm{d}t + b_w\,\mathrm{d}\xi_t, \tag{1.16}$$

where ξ_t is the random process in the vertical velocity. Here the initial velocity condition is sampled from a Gaussian distribution with zero mean and variance equal to the variance of the turbulent velocity $\sigma_w^2 = \langle W_t^2 \rangle$ (i.e. $W_0 \sim \mathcal{N}(0, \sigma_w^2)$). From Taylor's (1921) analysis mentioned above, he showed that the rate of increase in time of the ensemble mean spread, measured by the variance of the displacement $\sigma_z^2 = \langle Z_t^2 \rangle$, is given exactly by

$$\frac{\mathrm{d}\sigma_z^2}{\mathrm{d}t} = 2\int_0^t \langle W_{t'} W_{t'+\xi} \rangle\ \mathrm{d}\xi \equiv 2\,\sigma_w^2 \int_0^t R_{ww}(\xi)\,\mathrm{d}\xi,$$

where $R_{ww}(\xi)$ is the Lagrangian velocity autocorrelation function, and denoting the Lagrangian decorrelation time as

$$\tau_w = \int_0^\infty R_{ww}(\xi)\,\mathrm{d}\xi. \tag{1.17}$$

Note that an alternate definition for τ_w (Tennekes, 1979) can be expressed in terms of the Kolmogorov constant C_0 and turbulence kinetic energy dissipation rate ϵ,

$$\tau_w = \frac{2\sigma_w^2}{C_0 \epsilon}.$$

By squaring and taking the ensemble average of eq. (1.16), and applying statistical properties of the velocity W_t and the ξ_t, and finally evaluating the resulting integral we get

$$\langle W_t^2 \rangle = \langle W_0^2 \rangle\ \mathrm{e}^{-2\,t/\tau_w} + \frac{b_w^2\,\tau_w}{2}\left(1 - \mathrm{e}^{-2\,t/\tau_w}\right).$$

As $\sigma_w^2 = \langle W_t^2 \rangle = \langle W_0^2 \rangle$, an expression for the vertical diffusion term in homogeneous

conditions is found to be

$$b_w^2 = \frac{2\sigma_w^2}{\tau_w}, \tag{1.18}$$

where τ_w is the Lagrangian decorrelation time-scale as defined in eq. (1.17).

We now proceed to the main SDEs in the framework for developing the RFM equations for the stochastic variables (Z_t, W_t)

$$\begin{aligned} \mathrm{d}W_t &= a_w(Z_t, W_t, t)\,\mathrm{d}t + b_w(Z_t, W_t, t)\,\mathrm{d}B_t \\ \mathrm{d}Z_t &= W_t\,\mathrm{d}t. \end{aligned} \tag{1.19}$$

Consider now the complementary approach to the SDE (1.19), i.e. the corresponding FPE describing the time-evolution of the probability density $p(z, w, t)$ of the stochastic variables (Z_t, W_t)

$$\frac{\partial p}{\partial t} = -\frac{\partial}{\partial z}(w\,p) - \frac{\partial}{\partial w}\left(a_w(z, w, t)\,p\right) + \frac{1}{2}\frac{\partial^2}{\partial w^2}\left(b_w^2(z, w, t)\,p\right), \tag{1.20}$$

and denote $p_e(z, w)$ as the density distribution for all particles of the air which has assumed Gaussian velocity statistics given by

$$p_e \sim \frac{1}{\sqrt{2\pi\sigma_w^2}} \exp\left(-\frac{w^2}{2\sigma_w^2}\right), \tag{1.21}$$

where σ_w is the standard deviation of the vertical velocity. It should be emphasised that the Gaussian distribution p_e (1.21) is the steady state of eq. (1.24). The solution p_e also known as the invariant measure of (1.25), can be thought as the physical distribution of particles in the background atmosphere in position-velocity space.

With the prescribed b_w and p_e from (1.18) and (1.21) respectively, the deterministic term a_w can be determined by applying the WMC (defined in §1.3.1). Imposing the WMC leads to $p = p_e$, which satisfies the FPE (1.20). By taking the fact that

$\partial p_e/\partial t = 0$ and integrating with respect to w, we get

$$a_w\, p_e = \frac{1}{2}\frac{\partial}{\partial w}\left(b_w^2\, p_e\right) - \int_{-\infty}^{w} \frac{\partial}{\partial z} p_e(z, w')w'\, \mathrm{d}w'. \tag{1.22}$$

Introducing the chosen diffusion term (1.18) into the first term on the right-hand side of (1.22) and inserting the pre-defined p_e distribution (1.21) into the second term, gives

$$a_w(z, w, t) = -\frac{w}{\tau_w} + \sigma_w \frac{\partial \sigma_w}{\partial z} + \frac{w^2}{\sigma_w}\frac{\partial \sigma_w}{\partial z}, \tag{1.23}$$

which is a unique definition of a_w in the vertical one-dimensional model. Subsequently we can use the results (1.18) and (1.23) to redefine the FPE (1.20) as

$$\frac{\partial p}{\partial t} = -\frac{\partial}{\partial w}\left(\left(-\frac{w}{\tau_w} + \frac{1}{2}\left(1 + \left(\frac{w}{\sigma_w}\right)^2\right)\frac{\partial \sigma_w^2}{\partial z}\right) p\right) + \frac{\partial^2}{\partial w^2}\left(\frac{\sigma_w^2}{\tau_w}\, p\right). \tag{1.24}$$

Therefore following the standard stochastic procedure, the vertical RFM equations describing the dispersion in the ABL are defined as

$$\mathrm{d}W_t = \left(-\frac{W_t}{\tau_w} + \frac{1}{2}\left(1 + \frac{W_t^2}{\sigma_w^2}\right)\frac{\partial \sigma_w^2}{\partial z}\right)\mathrm{d}t + \left(\frac{2\sigma_w^2}{\tau_w}\right)^{1/2}\mathrm{d}B_t, \tag{1.25a}$$

$$\mathrm{d}Z_t = W_t\, \mathrm{d}t, \tag{1.25b}$$

which are a set of SDEs that are integrated simultaneously to obtain the displacement $Z(t)$. Physically, it is easy to understand most of the terms in (1.25). Equation (1.25b) is a standard trajectory equation, whereas (1.25a) resembles Ornstein-Uhlenbeck process (see §3.8.4 of Gardiner, 2009, for e.g.), or random walks in quadratic potential wells, which in spatially homogeneous turbulence would result in W_t having 'red noise' frequency spectra. The additional term in (1.25a) is necessary for the model to be well-mixed as discussed above.

1.3.2.1 Change of variables and nondimensionalisation

From the derived RFM equations (1.25), we can obtain a more convenient set of SDEs using Itô's lemma (see theorem 1.2.1) and the change of variables $\Omega_t = W_t/\sigma_w$, given by

$$\begin{aligned} \mathrm{d}\Omega_t &= \left(-\frac{\Omega_t}{\tau_w} + \frac{\partial \sigma_w}{\partial z}\right) \mathrm{d}t + \left(\frac{2}{\tau_w}\right)^{1/2} \mathrm{d}B_t, \\ \mathrm{d}Z_t &= \Omega_t \, \sigma_w \, \mathrm{d}t. \end{aligned} \tag{1.26}$$

The new form of LPDM equations (1.26) has a relatively simple FPE for probability density $p(\omega, z, t)$ of trajectories in (ω, z)-space

$$\frac{\partial p}{\partial t} = -\frac{\partial \left(\omega \sigma_w p\right)}{\partial z} - \frac{\partial}{\partial \omega}\left(\left(-\frac{\omega}{\tau_w} + \frac{\partial \sigma_w}{\partial z}\right) p\right) + \frac{1}{\tau_w}\frac{\partial^2 p}{\partial \omega^2}, \tag{1.27}$$

where $\omega = w/\sigma_w$ explicitly. It is often much simpler to view the eq. (1.27) as a non-dimensional equation given that ω is already a non-dimensional variable. The new rescaled variables are listed in the following table

Variable	Description	Dimensions	Rescaled variable
z	vertical height	L	$\tilde{z} = z/h$
t	time	T	$\tilde{t} = t/T$
σ_w	velocity standard deviation	L T^{-1}	$\tilde{\sigma}_w = \sigma_w/u_*$
τ_L	decorrelation time-scale	T	$\tilde{\tau}_w = \tau_w/T_L$

Here h denotes the ABL height, u_* the surface friction velocity, T_L the Lagrangian time scale, and L and T are the length and time scales. Inserting these rescaled variables into (1.27), the non-dimensionalized model for $\tilde{p}(\tilde{z}, \omega, \tilde{t})$ is found to be

$$\frac{T_L}{T}\,\frac{\partial \tilde{p}}{\partial \tilde{t}} = \frac{1}{\tilde{\tau}_w}\,\frac{\partial}{\partial \omega}\left(-\omega\,\tilde{p} + \frac{\partial \tilde{p}}{\partial \omega}\right) - \varepsilon\,\frac{\partial \tilde{\sigma}_w}{\partial \tilde{z}}\,\tilde{p} - \varepsilon\,\frac{\partial}{\partial \tilde{z}}\left(\omega\,\tilde{\sigma}_w\,\tilde{p}\right), \tag{1.28}$$

where ε is the non-dimensional parameter such that $\varepsilon = u_* T_L/h$. In physical terms, ε can be thought as the time scale ratio between the Lagrangian time scale and the diffusive time scale, i.e. $\varepsilon^2 = T_L/T_D$. The Lagrangian time scale T_L can be understood as the length of time at which a particle ceases to "remember" its initial velocity, and diffusive time scale T_D is the typical time that a particle takes to be transported across the ABL height h due to diffusion. Subsequently, a natural time scale for the system of (1.28) is $T = h/u_*$, which leads to the non-dimensional FPE

$$\frac{\partial \tilde{p}}{\partial \tilde{t}} = \frac{1}{\varepsilon\, \tilde{\tau}_w}\, \frac{\partial}{\partial \omega} \left(-\omega \tilde{p} + \frac{\partial \tilde{p}}{\partial \omega} \right) - \frac{\partial \tilde{\sigma}_w}{\partial \tilde{z}}\, \tilde{p} - \frac{\partial}{\partial \tilde{z}} \left(\omega \tilde{\sigma}_w\, \tilde{p} \right). \tag{1.29}$$

Two distinct behaviours of the particles can be brought to the fore by taking the limits $\varepsilon^2 \ll 1$ (diffusive) and $\varepsilon^2 \to \infty$ (ballistic). The former behaviour is equivalent to taking the limit of zero Lagrangian decorrelation time ($\tau_w \to 0$) of the RFM, often known as the RDM or eddy diffusion model, which is discussed in greater detail below. In contrast, the latter 'ballistic' limit refers to a (bizarre) regime where particles retain their velocity for very long times.

The distinction between the two behaviours above is demonstrated in Figure 1.4 where the paths of five independent particles are tracked by solving the corresponding SDEs to the non-dimensional FPE (1.29) when the appropriate ε-limits are taken. The $\varepsilon^2 \ll 1$ limit in the left panel shows particles moving haphazardly as one would expect to see in a random walk. By contrast in the right panel, the $\varepsilon^2 \gg 1$ limit illustrates the "memory-dominated" spread in which the distance travelled by a particle increases almost linearly in one direction with time, analogous to the ballistic motion of bullets.

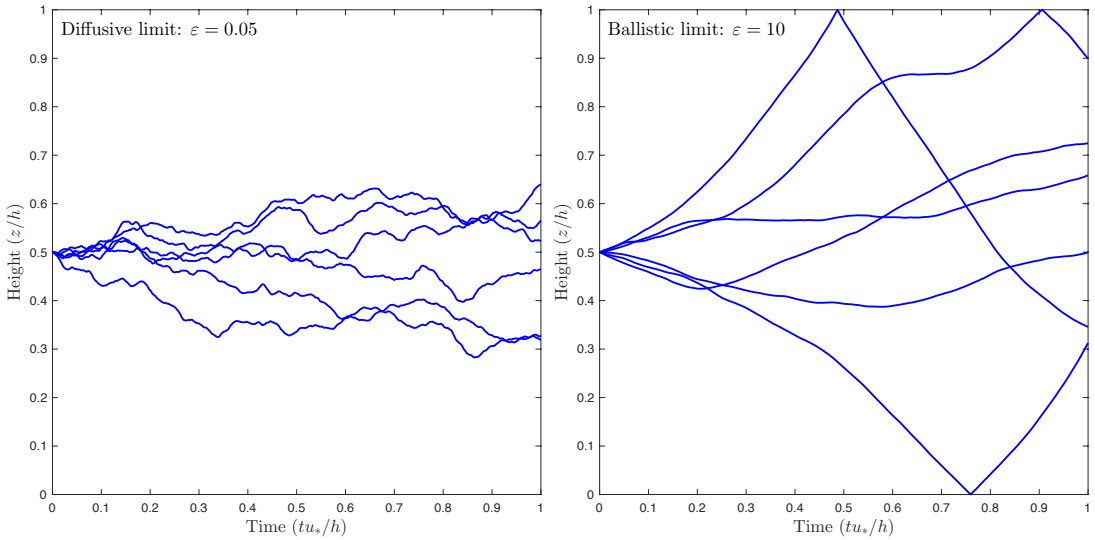

Figure 1.4: Trajectories of five particles illustrating the two ε limit behaviours, from $z_0 = 0.5$ initial release. Left panel: diffusive paths with a small ε limit, $\varepsilon = 0.05$. Right panel: ballistic paths with a large ε limit, $\varepsilon = 10$.

1.3.3 The diffusion limit: random displacement model (RDM)

Here we will show that the RDM is the zero correlation time limit or the diffusion limit of the RFM. In the RDM, the SDE for the displacement of a particle is integrated directly without the need to calculate the particle's velocity. For simplicity, we consider again the one dimensional (vertical) diffusion in the ABL. Under the distinguished limit in which the Lagrangian decorrelation time vanishes and the variance of the velocity fluctuations tend to infinity, the two RFM equations (1.25a) and (1.25b) can be combined and transformed into one equation for the random displacement $Z(t)$ only. The following description of the mathematical transformation from the RFM to the RDM equation is adapted from Rodean (1996, see §6.3).

Starting with the RFM equations (1.25) for the stationary inhomogeneous Gaus-

sian turbulence, we can be rewrite the W-equation (1.25a) in terms of W/σ_w,

$$\mathrm{d}\left(\frac{W_t}{\sigma_w}\right) = \left(-\frac{W_t}{\sigma_w \tau_w} + \frac{\partial \sigma_w}{\partial z}\right) \mathrm{d}t + \left(\frac{2}{\tau_w}\right)^{1/2} \mathrm{d}B_t, \tag{1.30a}$$

and for convenience we repeat the Z-equation (1.25b) for this section too,

$$\mathrm{d}Z_t = W_t \, \mathrm{d}t. \tag{1.30b}$$

We will formally deal with the required limits by rescaling the turbulence

$$\tau_w = \alpha \, T(z), \quad \sigma_w = \beta \, \Sigma(z). \tag{1.31}$$

In order for the turbulence to retain its characteristics, the conditions that $\tau_w(z) \to 0$ with t fixed and $t/\tau_w(z) \to \infty$ with τ_w fixed, are equivalent to taking the following limits on the rescaling constants (de Baas and Troen, 1989)

$$\alpha \to 0, \quad \beta \to \infty \quad \text{such that} \quad \alpha\beta^2 = K(\text{constant}), \tag{1.32}$$

which will guarantee that the eddy diffusivity $\kappa(z) = \sigma_w^2(z)\tau_w(z)$ remains an invariant function of z. Inserting (1.31) into eq. (1.30a), integrating the result and then multiplying throughout by $\alpha\beta$, we get

$$\alpha\left(\frac{W_t}{\Sigma} - \frac{W_0}{\Sigma}\right) = \int_0^t \left(\left(-\frac{W_t}{\Sigma T} + \alpha\beta^2 \frac{\mathrm{d}\Sigma}{\mathrm{d}z}\right) \mathrm{d}t + \left(\frac{2\alpha\beta^2}{T}\right)^{1/2} \mathrm{d}B_t\right). \tag{1.33}$$

Because the velocity W_t is bounded in the statistical sense under the conditions (1.32), therefore the term $W_t/\Sigma - W_0/\Sigma$ on the left-hand side of (1.33) remains bounded in the "mean square" sense for all time. The left-hand side then vanishes when $\alpha \to 0$ as required in (1.32). We proceed by combining (1.32) and (1.33) with

the result that

$$\int_{z_0}^{Z_t} \frac{\mathrm{d}Z'_t}{\Sigma(Z'_t)T(Z'_t)} = \int_0^t \left(K\frac{\mathrm{d}\Sigma}{\mathrm{d}z}\,\mathrm{d}t + \left(\frac{2K}{T}\right)^{1/2} \mathrm{d}B_t \right), \tag{1.34}$$

where the left-hand side is obtained by substituting the SDE (1.30b) and z_0 is the release point. Following closely from Rodean (p. 29 of 1996), we differentiate both sides using the rules of Itô calculus to convert (1.34) back into a SDE,

$$\frac{\mathrm{d}Z_t}{\Sigma T} - \frac{1}{2}\left(\frac{\mathrm{d}Z_t}{\Sigma T}\right)^2 \frac{\mathrm{d}}{\mathrm{d}z}(\Sigma T) = K\frac{\mathrm{d}\Sigma}{\mathrm{d}z}\,\mathrm{d}t + \left(\frac{2K}{T}\right)^{1/2} \mathrm{d}B_t. \tag{1.35}$$

This is of the quadratic equation for $\mathrm{d}Z_t$ of the form $A(\mathrm{d}Z_t)^2 + B(\mathrm{d}Z_t) + C = 0$, where we set

$$A = \frac{1}{2}(\Sigma T)^{-1}\frac{\mathrm{d}}{\mathrm{d}z}(\Sigma T), \quad B = -1, \quad C = (\Sigma T)\left(K\frac{\mathrm{d}\Sigma}{\mathrm{d}z}\,\mathrm{d}t + \left(\frac{2K}{T}\right)^{1/2} \mathrm{d}B_t \right),$$

which means that we can select the root $\mathrm{d}Z_t = \left(1 - (1 - 4AC)^{1/2}\right)/2A$. To prepare the solution to the quadratic equation (1.35), we expand $(1-4AC)^{1/2}$ in the infinite series

$$(1 - 4AC)^{1/2} = 1 - \frac{4AC}{2} - \frac{(4AC)^2}{8} - \ldots,$$

and retain only the first three terms to get the solution $\mathrm{d}Z_t = C + AC^2$. This is done in accord with the rules of Itò calculus that terms involving $\langle \mathrm{d}B_t \rangle^2$ be retained, because

$$(\mathrm{d}t)^2 = 0, \quad \langle \mathrm{d}B_t\,\mathrm{d}t \rangle = 0, \quad \text{and} \quad \langle \mathrm{d}B_t \rangle^2 = \mathrm{d}t.$$

Applying these results, we obtain

$$\begin{aligned} \mathrm{d}Z_t &= (\Sigma T)\left(K\frac{\mathrm{d}\Sigma}{\mathrm{d}z}\,\mathrm{d}t + \left(\frac{2K}{T}\right)^{1/2}\mathrm{d}B_t\right) + \Sigma K\frac{\mathrm{d}\,(\Sigma T)}{\mathrm{d}z}\,\mathrm{d}t, \\ &= \left(2K\Sigma T\,\frac{\mathrm{d}\Sigma}{\mathrm{d}z} + K\Sigma^2\,\frac{\mathrm{d}T}{\mathrm{d}z}\right)\,\mathrm{d}t + (\Sigma T)\left(\frac{2K}{T}\right)^{1/2}\mathrm{d}B_t. \end{aligned}$$

Substituting $K = \alpha\beta^2$ and transforming back into their turbulence statistics (1.31), we finally obtain the following SDE for the RDM

$$\mathrm{d}Z_t = \frac{\partial}{\partial z}\left(\kappa_w\right)\,\mathrm{d}t + \left(2\,\kappa_w\right)^{1/2}\mathrm{d}B_t, \tag{1.36}$$

where $\kappa_w(z) = \sigma_w^2(z)\tau_w(z)$ is the diffusivity term. Finally the FPE that describes the evolution of the particle density distribution $p(z,t)$ that is consistent with the RDM equation (1.36) is found to be

$$\frac{\partial p}{\partial t} = \frac{\partial}{\partial z}\left(\kappa_w\,\frac{\partial p}{\partial z}\right). \tag{1.37}$$

Other derivations of the RDM are also available, for e.g. see the papers of Durbin (1983) and Boughton et al. (1987) who determined the drift and diffusion terms by checking the consistency of the FPE under the eddy diffusion closure.

1.3.4 Applicability of RFMs and RDMs

Going back to Taylor's (1921) results as mentioned in the beginning of this section, in which he showed the diffusion rate in two asymptotic limits:

$$\langle Z_t^2\rangle = \begin{cases} \sigma_w^2\,t^2, & t \ll \tau_w \quad \text{(near-field)}, \\ 2\,\kappa_w\,t, & t \gg \tau_w \quad \text{(far-field)}. \end{cases} \tag{1.38}$$

Because of the limiting conditions imposed in the transformation from eq. (1.25)

to eq. (1.36): $\tau_w \to 0$ with t fixed and $t \to \infty$ with τ_w fixed, the time scales for which the RDM is applicable are much greater than the local decorrelation time, i.e. $t \gg \tau_w$, which is exactly the far-field regime above. This is when the dispersion is dominated by the diffusion term and the spread of the the particle concentration is slower and grows only as $t^{1/2}$. In the near-field $t \ll \tau_w$, the dispersion is dominated by the drift term (persistence in the particle velocities) and the concentration grows linearly with time t.

As highlighted above, the RDMs are able to model the far-field accurately and on the other hand, RFMs can capture the physics of the turbulence in the near-field regime (close to the sources where turbulence is non-diffusive) and also in the far-field regime further from the source. This is one of the fundamental advantages of the RFM, in which it provides a more realistic model representation of the turbulent velocity fluctuations. Moreover, RFMs can capture effects due to non-Gaussian velocity statistics in unstable ABL conditions, and are valid for all time scales (except below the Kolmogorov timescale, where viscosity becomes relevant; (Monin and Yaglom, 1977)).

Nevertheless, the RDM has the appeal of its simple implementation in integrating only one equation for displacement. RDMs can generally be integrated with longer time-steps than RFMs, because in RFMs the time-step is limited by the local Lagrangian time-scale (i.e. $\Delta t \ll \tau_w$). This has been shown to be a required condition to resolve the turbulent velocity fluctuations in the RFM. In this case, the RDM becomes the more convenient and flexible option than RFMs.

To help the reader gain better understanding of the behaviour of the RFM and RDM, Figure 1.5 shows a graphic illustration of the typical particle paths of each model. Here six particles are released from the same locations in a (X, Z) domain, and each coloured line represents each particle trajectory plotted in time. The particles can be seen to independently experience the random walk (RDM) process (1.36) in the left panel and the short time $t \ll \tau_w$ behaviour of the RFM process

(1.25) in the right panel.

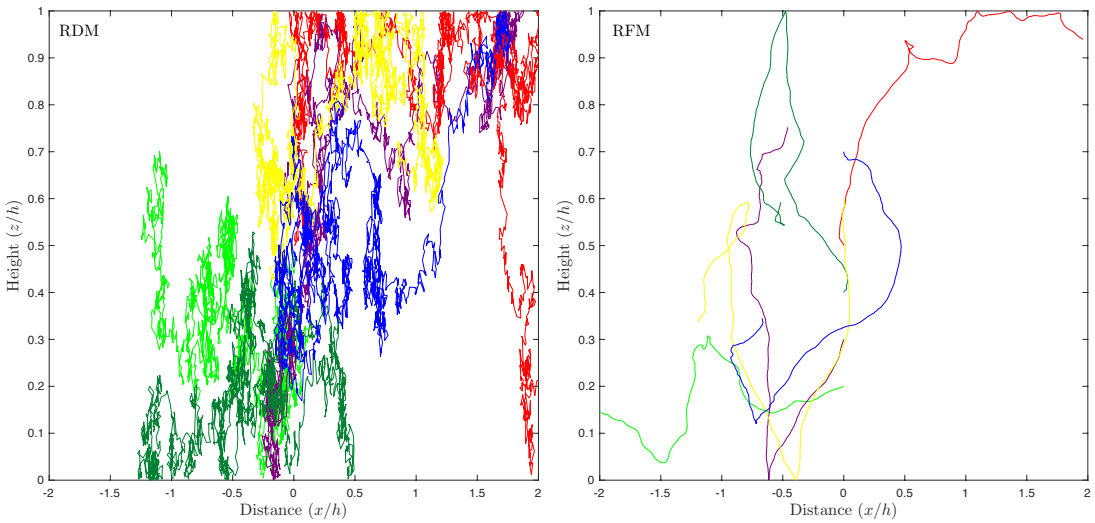

Figure 1.5: The typical paths of six independent two-dimensional trajectories in the diffusive limit or RDM (left panel) and with finite (τ_u, τ_w) limit in the LPDM (right panel).

1.3.5 Turbulence parameterisations

In order to select a specific LPDM suitable for realistic ABL conditions, it is necessary to use suitable profiles for (i) variance of the turbulent velocity fluctuations (e.g. σ_w^2), and (ii) the local Lagrangian decorrelation time-scale (e.g. τ_w). The inputs are generally assumed as functions of z (for inhomogeneous flows) and their gradients are continuous, and they are also assumed to be horizontally homogeneous. Lagrangian stochastic models have traditionally been driven by semi-empirical parameterisations of flow and turbulence quantities, often involving similarity relationships (see §12 of Rodean, 1996). Such parameterisations are constantly under development based on new and better observational studies.

For the purposes of the present work, we will use empirical turbulence parameterisations for the stable (black shaded area of the diurnal cycle in Figure 1.2) and

neutral ABL conditions only. The situation in the unstable or convective boundary layer is more complex as the vertical velocity statistics are non-Gaussian due to the organised motion consisting of updrafts and downdrafts (see e.g. Cassiani et al., 2015). To capture the essential physics of the convective ABL therefore requires a considerably more complicated test case, hence the convective ABL is not considered here. For simplicity, stationary (time-independent) turbulence profiles are used here which is a reasonable approximation in most circumstances, as ABL turbulent statistics tend to evolve on a time-scales longer than the homogenisation timescale h/u_*. In light of the diurnal cycle (Figure 1.2), temporal variations of the ABL height h can be adapted into our non-dimensionalised time scale h/u_*, where u_* is the surface friction velocity.

Profiles of turbulent $(\sigma_u, \sigma_v, \sigma_w)$ and (τ_u, τ_v, τ_w) for the stable and neutral ABL used here are adapted from Hanna (1982), which have been obtained through empirical fits to observed data. They are derived from boundary layer parameters ABL height h and friction velocity u_*, as listed in the following table. Here-in-after we consider nondimensionalised models throughout under the domain $0 \leq \tilde{z} \leq 1$ where $\tilde{z} = z/h$ (see §1.3.2.1 for details) and drop the tildes for convenience. Here subscripts u and v denote the along-wind and the cross-wind components, w refer to the vertical component of the turbulent velocities, and f is the Coriolis parameter (typically $\sim 10^{-4}$ rad/s). In the practical implementation of our study models, minor modifications are taken in practice to the spatial domain as Hanna's (1982) scheme does not always yield smooth profiles, especially at the ABL top and bottom boundaries.

Condition	$\sigma(z)$	$\tau(z)$
Stable	$\sigma_u = 2.0\,(1-z)$ $\sigma_v = \sigma_w$ $\sigma_w = 1.3\,(1-z)$	$\tau_u = 0.15\,z^{1/2}/\sigma_u$ $\tau_v = 0.07\,z^{1/2}/\sigma_v$ $\tau_w = 0.1\,z^{4/5}/\sigma_w$
Neutral	$\sigma_u = 2.0\exp(-2z/\epsilon)$ $\sigma_v = \sigma_w$ $\sigma_w = 1.3\exp(-2z/\epsilon)$	$\tau_u = \tau_v = \tau_w$ $\tau_w = \dfrac{z}{2\sigma_w(1+15z/\epsilon)}$

The nondimensional profiles of the velocity standard deviation $\sigma(z)$ and Lagrangian decorrelation time-scale $\tau(z)$ suitable for (i) a stable ABL, and (ii) a neutral ABL (e.g. Hanna, 1982). The non-dimensional parameter $\epsilon = u_*/fh$ is a boundary layer Rossby number.

1.3.6 The boundary conditions

An important issue that a modeller must encounter in using the stochastic dispersion models is the boundary condition problem: How do we treat the particle trajectories near the boundaries of the ABL? The following discussion is concerned with the boundaries at the bottom ($z = 0$), that generally corresponds to the land or water surface, and the top ($z = h$) of the turbulent ABL, for the dimensional model eq. (1.24).

There are a few papers in the literature that discussed the boundary conditions in great detail, Rodean (1996, §11) gives a comprehensive historical review of the few above-mentioned papers. One paper worthy of study is that of Wilson et al. (1993), who found that the perfect reflection algorithm is exactly consistent with the WMC in the one-dimensional model for homogeneous Gaussian turbulence (for the lengthy mathematical analysis, see the appendix to chapter 11 of Rodean, 1996). Another pioneering work is by Thomson et al. (1997) in which they extended the reflection algorithms to the case where there is a discontinuity in turbulence levels

across an interface such as the ABL top. In the RFM (1.24), boundary conditions consistent with perfect reflection above are

$$p(w,0,t) = p(-w,0,t), \quad p(w,h,t) = p(-w,h,t), \tag{1.39}$$

where $z = 0$ corresponds to the ground surface and $z = h$ is a non-penetrable inversion layer at the top of the ABL. In probabilistic terms, this is equivalent to the reflection condition $W_t \to -W_t$ being applied at the boundaries in solving the SDEs (1.25).

In the numerical simulation of the RFM (1.25), the reflection condition can be explicitly implemented in the following algorithm. If a particle travels from an allowed state (Z_{t_j}, W_{t_j}, t_j) to a forbidden state $(Z^*, W^*, t_j + \Delta t)$ on the other side of the boundaries, i.e. below $Z = 0$ or above $Z = h$, then

(*a*) $Z_{t_j+\Delta t}$ must be reflected back into the domain, at an appropriate distance above $Z = 0$ or below $Z = h$, and

(*b*) the velocity direction is reversed, $W_{t_j+\Delta t} = -W^*$.

Provided that the discrete time-step is kept sufficiently small, specifically $\Delta t \ll \tau_w(z)$ throughout the flow, the WMC is approximately met to an acceptable level of accuracy.

1.4 Rare-event simulation

Suppose we are interested in the concentration of a tracer at a single location in our model. There are many possible applications of this scenario, for instance, consider an unexpected volcanic eruption in a 'source' location, and suppose that we are only interested in the concentration of ash clouds in the area of an airport or a flight corridor (the 'receptor'). Alternatively, the source could be a poison chemical

release and the receptor an isolated population centre. For practical reasons a grid-based Eulerian model designed to calculate the full spatial solution of the tracer concentration, is evidently inefficient. A Lagrangian model on the other hand will offer greater efficiency in certain flow set ups, provided that a sufficient number of trajectories reach the receptor region. In the examples described above, it is more likely that only a few percentage of the simulated trajectories will end up in the target area or in other words, the flow of particles from source to receptor is weak in a certain sense. This is known as a rare-event simulation in statistics.

1.4.1 Variance reduction

Importance sampling is a variance reduction technique developed for Monte Carlo simulation or SDEs (see for e.g. Kloeden and Platen, 1992; Øksendal, 2007). It is based on the concept that the trajectories are steered in the direction of the rare-event by adjusting the particle paths and correcting the resultant output by weighing them with suitable likelihood ratios. These methods are well-understood and widely used in mathematical finance and statistical physics. In the context of atmosphere-ocean advection-diffusion problems, importance sampling methods were used in simple parallel flows, to obtain far-field concentrations in Taylor dispersion problems (Haynes and Vanneste, 2014). However importance sampling can turn out to be a more difficult problem especially in complex model systems.

More recently, Esler (2015) developed a robust adaptive trajectory algorithm for problems in the chaotic advection regime, based on the 'splitting' method known as the 'go-with-the-winners' (GWTW) (Grassberger, 1997, 2002). Roughly speaking, the idea behind the splitting method is to clone the trajectories that approach the receptor region of interest and let the others die. We give a brief introduction to the GWTW method in the following section and also extend the method to the RFM of the turbulent ABL dispersion in Chapter 3. More modern splitting method can

be found in the paper of Cérou and Guyader (2007) for example.

Suppose our interest is in the expected value that a pollutant tracer ends up in a receptor region R at time $t = T$, denoted by μ. Let $I_R(\boldsymbol{X}_t)$ be the indicator function of the event that particle $\boldsymbol{X}_t^{(i)}$ reaches region R at time t,

$$I_R(\boldsymbol{X}_t) = \begin{cases} 1 & \boldsymbol{X}_t^{(i)} \in R, \\ 0 & \text{otherwise.} \end{cases} \tag{1.40}$$

Therefore the expected value μ is $\mu = \mathbb{E}\left(I_R(\boldsymbol{X}_T)\right)$. There are several available approaches to evaluate this expectation, one option is to simulate N independent trajectories forward in time to time $t = T$. Since we are only interested in the expectation, a weak order numerical scheme for SDEs (for e.g. Euler-Maruyama (Maruyama, 1955)) can be used to obtain solutions of the random variable $\boldsymbol{X}_T$, and subsequently use the estimator

$$\tilde{\mu} = \frac{1}{N} \sum_{i=1}^{N} I_R(\boldsymbol{X}_T^{(i)}), \tag{1.41}$$

often called the naive Monte-Carlo (NMC) estimator, which is just the average mean of N independent simulations of the random variable $I_R(\boldsymbol{X}_T)$ from the forward Monte-Carlo method. The strong law of large numbers ensures that $\tilde{\mu} \to \mu$ almost surely as $N \to \infty$.

However for the scenarios described above when μ is small, most samples of $I_R(\boldsymbol{X}_T)$ would be zero, while rare samples equaling one would be observed. This means N would have to be quite large for a reliable estimate of small μ, which can

be shown explicitly using the statistical error i.e. the variation in the mean,

$$\begin{aligned}
(\Delta\tilde{\mu})^2 &\approx \frac{1}{N}\mathrm{Var}\left(I_R(\boldsymbol{X}_T)\right), \\
&\approx \frac{1}{N}\sum_{j=1}^{2} P(I_j(\boldsymbol{X}_T))\left(I_j(\boldsymbol{X}_T)-\mu\right)^2, \\
&\approx \frac{1}{N}\left(p(1-p)^2+(1-p)p^2\right) \\
\Delta\tilde{\mu} &\approx \sqrt{\frac{p(1-p)}{N}}, \qquad (1.42)
\end{aligned}$$

where p is the probability the tracer ensemble $\boldsymbol{X}_T$ reaches the region R, and $\mu = \sum_j I_j(\boldsymbol{X}_T)P(I_j(\boldsymbol{X}_T)) = p$. In particular, the width of the confidence interval, $[\tilde{\mu} \pm \Delta\tilde{\mu}]$ decreases only with order $N^{-1/2}$ as $N \to \infty$. Hence, in order to obtain sufficiently small confidence intervals it is important to begin with a small variance (i.e. $p(1-p)$) in the random variable $I_R(\boldsymbol{X}_T)$. This is a big drawback of the forward simulation method, which leads to the second possibility of constructing other estimators which have nearly the same expectation, but smaller variance.

One way to construct such an estimator will be described in the next section which involves a modified Monte Carlo process $\tilde{\boldsymbol{X}}_t$ and correcting weights Θ_t. The weights are chosen strategically so that their expectation value is the same as that of $I_R(\boldsymbol{X}_T)$, i.e.

$$\mathbb{E}\left(\Theta_T\, I_R(\tilde{\boldsymbol{X}}_T)\right) = \mathbb{E}\left(I_R(\boldsymbol{X}_T)\right). \qquad (1.43)$$

1.4.2 Grassberger's GWTW branching process

The go-with-the-winners (GWTW) splitting method (Grassberger, 1997, 2002) can be described as a branching process that is applied to the trajectory ensemble $\{\boldsymbol{X}_t^{(i)},\ i = 1, \ldots, N\}$ at discrete time intervals. Initially, trajectories are assigned weight Θ_0 evaluated depending on the SDE problem at hand. The ensemble for the SDE is then integrated forwards from $t = 0$ and subsequently, the GWTW

trajectory weights Θ_t are updated according to the following algorithm at branching time $t_j = j\,\Delta t$ $(j = 1, 2, 3, \ldots)$. The implementation of the algorithm proceeds as follows:

(a) Each trajectory in the ensemble is assigned a score $S_{t_j}^{(i)}$ using a scoring algorithm. The trajectories are then ordered in a sequence by decreasing score.

(b) Considering the last $N/2$ trajectories in the sequence (i.e. trajectories with the lowest scores), we call the trajectory with the mth lowest score a 'loser' if its score is less than one-third of the score with the mth highest score. Count the total number of losers and denote it by L.

(c) The weights of the L loser trajectories are then, either doubled $\Theta_{t_j} \to 2\Theta_{t_j}$ or set to zero $\Theta_{t_j} \to 0$, randomly with probability one-half. The W $(\approx L/2)$ trajectories with scores zero are then removed from the ensemble.

(d) The W trajectories with the highest scores or the first W trajectories in the ordered sequence, are called the 'winners'. Each winner $\boldsymbol{X}_{t_j}^{(k)}$ is then cloned where an additional trajectory is created: $\boldsymbol{X}_{t_j}^{(l)} = \boldsymbol{X}_{t_j}^{(k)}$, and each clone will have half the weight of its parent, i.e. $\Theta_{t_j}/2$.

A schematic diagram of the algorithm steps $(a) - (d)$ for choosing the typical loser and winner trajectories in the ordered sequence at branching time t_j, is shown in Figure 1.6 below. Variance reduction of the score distribution $\{S_{t_j}^{(i)}, i = 1, \ldots, N\}$ occurs here because a loser trajectory (red) is identified if their score is less than around half of the ensemble average score, and will either be doubled in score or removed completely. Any trajectory with a score much greater than two or three times the ensemble mean will be identified as the winner (green), and split into two trajectories with each clone having half of its weight. The two clones will subsequently follow different Brownian motions in the next integration time. The same number of winners being cloned and losers being removed in the algorithm ensures

that the number of trajectories N in the ensemble is kept constant. Moreover, implementing the steps $(a)-(d)$ at sufficiently frequent time intervals in the GWTW process $\tilde{\boldsymbol{X}}_t$ will ultimately ensure that the distribution of all scores S_t remain within a factor of two or so of the ensemble mean $\langle S_t \rangle$. Crucially, this is achieved without changing the overall expectation value of the process as is required in (1.43).

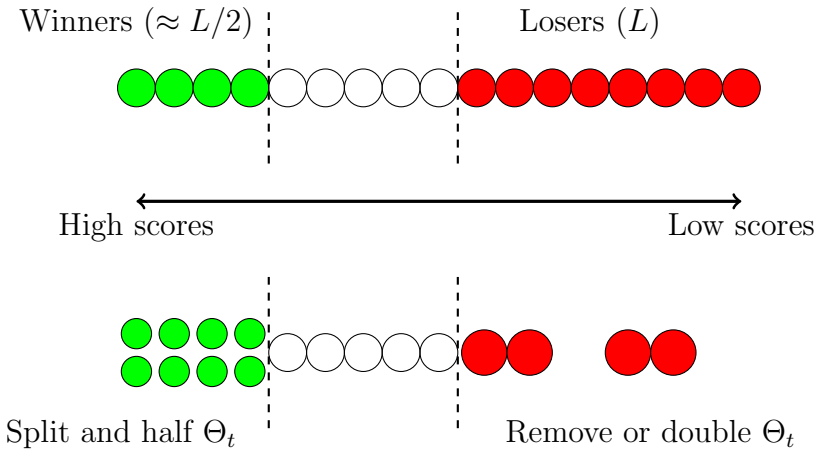

Figure 1.6: The GWTW splitting method for selecting the L losers and the $W(\approx L/2)$ winner trajectories according to their decreasing score sequence. Losers are either removed or doubled in weight with probability one-half and the winners are split with half the original weight.

The difficulty of using this method is the choice of scoring algorithm which drives the effectiveness of the GWTW process. An ideal scoring algorithm at time t suggested by Esler (2015, Eq. (3.21)) is

$$S_t = \Theta_t \, c^*(\boldsymbol{X}_t, t),$$

which is simply the product of the trajectory weight and the local value of the adjoint solution of the FPE.

1.5 Scope and outline of thesis

In this introductory chapter we discussed the background theory that leads to the formulation of two types of LPDMs which are widely used to model single particle dispersion in the turbulent ABL, namely the RFM and RDM. Depending on the relative importance of accuracy versus efficiency of computation, an educated decision on the choice of model should be made based on the discussions above. As already stated, the success of Lagrangian approach has reached a wide range of dispersion applications, and this has led to its further development including hybrid models that take advantage of the capabilities of both Lagrangian and Eulerian approaches, to enhance computational efficiency in operational systems e.g. HYSPLIT (Draxler et al., 1997) and NAME (Jones et al., 2007). However, there is always scope for further developments, including research on parameterisations of turbulent statistics or on boundary condition algorithms.

In Chapter 2, we contribute to the development of LPDMs in the aspect of assessing the stochastic numerical methods of RFMs for operational use in the context of the turbulent ABL dispersion. A series of one-dimensional turbulent ABL test problems are introduced and a rigorous methodology for the evaluation of integration schemes for Lagrangian models is presented. The FPE is solved numerically using a finite-difference discretisation in physical space, and a Hermite function expansion in velocity space. Numerical convergence errors in the FPE solutions are shown to be much less than the statistical error associated with a practical-sized ensemble ($N = 10^6$) of trajectory solutions, hence the former can be used to validate the latter. The test problems are then used to evaluate commonly used integration schemes. The results allow for optimal time-step selection for each scheme at a required level of accuracy, consequently recommendations are made for use in operational models.

The aim of of Chapter 3 is to improve understanding of how and why the be-

haviour of RFMs in the ABL can differ from simpler RDMs (or eddy diffusivity models). To demonstrate this, we examine the shear disperion, sometimes known as Taylor-Aris dispersion (Taylor, 1953; Aris, 1956) that develops over the depth of the ABL after the tracer homogenization (well-mixed) period in the long-time dispersion. Saffman's (1962) analysis for the bounded one-dimensional vertical diffusion becomes relevant for understanding the effective horizontal diffusivity in the ABL over a period of a few hours. Next, we look at the evolution of the behaviour of concentrations in the tails of a distribution which can be described mathematically by large deviation theory. The large deviation results are verified by solving the LPDM equations numerically for a large ensemble of particles. Turbulent statistics relevant to stable and neutral boundary layer conditions are considered.

Chapter 4 discusses methods of kernel density estimation for the estimation of particle concentrations in trajectory models. In this chapter we consider a simple two-dimensional RDM to describe the advection-diffusion flow in a chaotic advection regime. We have selected this model because the easily implemented numerical method to solve its Eulerian FPE provides very accurate solutions for the particle concentration, which can be used to assess our kernel density methods from the Lagrangian trajectory models. Some well-known techniques of bandwidth selection are briefly discussed, and then a new approach using Green's function to construct a more accurate kernel density estimator is proposed.

The concluding Chapter 5 describes an overview of the achievements in this dissertation. A discussion of the presented results as well as some recommendations and future improvements can also be found in this chapter. Hermite polynomial (also known as Gram-Charlier type A) expansions are used to simplify the numerical methodology of our problems in this thesis, a list of some useful formulas are moved to Appendix A.

Chapter 2

Quantitative Evaluation of numerical schemes for RFMs

2.1 Introduction

Although the numerical analysis of solution techniques for SDEs (e.g. Kloeden and Platen, 1992; Milstein and Tretyakov, 2004) is a mature subject in mathematics, RFMs have not, generally speaking, exploited developments in the subject, and are typically formulated using numerical schemes adapted from those used for ordinary differential equations (see e.g. Stohl et al., 2005). Validation of RFMs has focussed instead on direct comparison with observational data (Stohl et al., 1998; Ryall and Maryon, 1998). Our contention is that observational comparison, while clearly a necessary aspect of model development, will be insufficient if any uncertainty exists concerning the accuracy of the numerical solution of the underlying equations. The aim of this chapter is to introduce a rigorous framework for the testing and evaluation of numerical schemes for RFMs. This chapter is a slightly extended version of our published paper in the Geoscientific Model Development (Mohd. Ramli and Esler, 2016).

The framework is based on a standard one-dimensional dispersion model problem (Rodean, 1996; Wilson and Sawford, 1996), modelling the vertical dispersion of air parcels in the ABL. Vertical profiles of turbulent statistics representative of both stable and neutral conditions will be considered, and the RFM equations will be of the 'well-mixed' class (Thomson, 1987), meaning that long time probability distribution of the solutions (the invariant measure of the SDEs) is given by a pre-specified 'atmospheric' distribution (taken here to be uniform in physical space and Gaussian in velocity space). Hence the model problem, while idealised, captures key elements of the physics of dispersion in the stable and neutral ABL.

Our approach to evaluating a given RFM numerical scheme is to cross-validate its performance against a numerical solution of the corresponding FPE (see e.g. Gardiner, 2009). The FPE describes the time evolution of the probability density function (pdf) of the stochastic process, and is formulated in position-velocity space, so in the context of the current problem of dispersion in one spatial dimension, is a partial differential equation in 2+1 dimensions. Note that in three spatial dimensions in which the FPE is a 6+1 dimensional PDE, it will be computationally impractical in most circumstances to obtain accurate solutions to the FPE, and consequently RFMs will be the only practical tool to solve the problem.

A solution method based on a Hermite function expansion is introduced in order to obtain accurate solutions of the FPE with computational efficiency. Evaluation of the RFM scheme proceeds by a comparison of pdfs in an appropriate error norm, where the RFM pdf is generated from an ensemble of solutions, using the kernel density method (e.g. Silverman, 1986; Wand and Jones, 1994). The performance of various schemes are evaluated, as a function of time-step Δt, including the textbook (basic) Euler-Maruyama scheme, the second-order and third-order weak Runge-Kutta scheme of Platen (see §15.1 of Kloeden and Platen, 1992), the 'small-noise' second-order Runge-Kutta method of Honeycutt (Honeycutt, 1992), the 'long time-step' scheme used operationally in FLEXPART (Stohl et al., 2005) and a suggested

improvement to this last scheme.

The outline of this chapter is as follows. In §2.2, the SDEs describing the evolution of particle trajectories in the RFM are introduced, together with the corresponding FPE. A numerical solution scheme for the FPE is described and solutions are obtained and benchmarked for a number of test cases. In §2.3, the methodology for using the FPE solution to assess specific numerical schemes for the RFM is presented, and in §2.4 this methodology is then applied to specific schemes discussed above. In §2.5 the consequences of our findings are discussed and conclusions are drawn.

2.2 The model problem

2.2.1 RFM formulation

Consider a horizontally homogeneous turbulent ABL of uniform density, with a vertical velocity distribution that is Gaussian with zero mean and standard deviation $\sigma_w(z)$, and which has a Lagrangian decorrelation time-scale $\tau_w(z)$. The canonical SDE model (e.g. Rodean, 1996; Wilson and Sawford, 1996) for one-dimensional vertical dispersion in the ABL is exactly as eq. (1.25) and repeated here for convenience:

$$\begin{aligned} \mathrm{d}W_t &= \left(-\frac{W_t}{\tau_w} + \frac{1}{2}\left(1 + \left(\frac{W_t}{\sigma_w}\right)^2\right)\frac{\partial \sigma_w^2}{\partial z}\right)\mathrm{d}t + \left(\frac{2\sigma_w^2}{\tau_w}\right)^{1/2}\mathrm{d}B_t, \qquad (2.1) \\ \mathrm{d}Z_t &= W_t\,\mathrm{d}t. \end{aligned}$$

Here we use W_t and Z_t to denote the vertical velocity and height of a given air parcel at time t. Both are stochastic variables, with each individual realisation determined by that of the Brownian (or Wiener) process B_t. Further $\sigma_w = \sigma_w(Z_t)$ and $\tau_w = \tau_w(Z_t)$ are the values of $\sigma_w(z)$ and $\tau_w(z)$ local to the parcel.

In operational RFMs, such as FLEXPART, appropriate vertical profiles for $\sigma_w(z)$

and $\tau_w(z)$ are specified based on empirical fits to observations of different ABL conditions, as discussed in chapter 1.3.5. The equation set (2.1) is typically augmented with reflecting boundary conditions at the Earth's surface and at the ABL top (see Thomson et al., 1997, for detailed discussion of the top boundary condition). For definiteness, for our test-case runs, the initial velocity for (2.1) at $t = 0$ is sampled from a normal distribution $W_0 \sim \mathcal{N}(0, \sigma_w^2(z_0))$ and, for ease of comparison to the FPE results below, the initial position is sampled from a distribution $Z_0 \sim \mathcal{N}(z_0, \sigma_z^2)$ centred on an initial height z_0 with standard deviation σ_z.

For the purposes of numerical solution, it is more convenient (e.g. see §3.1 of Rodean, 1996) to use Itô's lemma to express (2.1) in terms of the variables $\Omega_t = W_t/\sigma_w(Z_t)$ and Z_t, leading to

$$\begin{aligned} \mathrm{d}\Omega_t &= \left(-\frac{\Omega_t}{\tau_w} + \frac{\partial \sigma_w}{\partial z}\right)\mathrm{d}t + \left(\frac{2}{\tau_w}\right)^{1/2}\mathrm{d}B_t, & \Omega_0 &\sim \mathcal{N}(0,1) \\ \mathrm{d}Z_t &= \Omega_t \sigma_w \,\mathrm{d}t, & Z_0 &\sim \mathcal{N}(z_0, \sigma_z^2). \end{aligned} \tag{2.2}$$

The simpler form (2.2) is exactly equivalent to (2.1). Moreover, the FPE of (2.2) has a considerably simpler form than the corresponding FPE of (2.1), a fact which will prove useful below. It is simplest to view equation (2.2) as a non-dimensional equation, given that in particular Ω_t is already a non-dimensional variable. The natural non-dimensionalisation has length, velocity and timescales of ABL height h, surface friction velocity u_*, and h/u_* respectively. Under this non-dimensionalisation, the spatial domain for (2.2) is $0 \leq Z_t \leq 1$.

To specify our test-case problems it is necessary to choose suitable (non-dimensional) profiles for $\sigma_w(z)$ and $\tau_w(z)$. Here we choose to focus on three such profiles, two of which are widely used (Hanna, 1982; Stohl et al., 2005) empirical fits to observed statistics in stable and neutral conditions respectively. The third has $\tau_w(z)$ constant and a linear profile for $\sigma_w(z)$, and is used to demonstrate a new RFM scheme introduced below. The details of the profiles used are given in Table 2.1 and plot-

ted in Figure 2.1. The profiles of the vertical velocity variances $\sigma_w^2(z)$ and their spatial derivatives $\mathrm{d}\sigma_w^2/\mathrm{d}z$ are also plotted in Figure 2.2. These terms appear in (2.1) which ensure that the particles become well-mixed in the domain over time, as discussed in §1.3.1. Here we modify the profiles of turbulent statistics for the stable and neutral ABL conditions, introduced in chapter 1.3.5 as $\bar{\sigma}_w(z)$ and $\bar{\tau}_w(z)$, where $Z_m(z) = z_b + z(1-2z_b)$ and $z_b = 0.05$ are chosen to avoid singular behaviour at the ABL top and bottom. This is necessary because in Hanna's original profiles either $\sigma_w \to 0$ or $\tau_w \to 0$ as $z \to 0, 1$ with neither type of behaviour being physical.

In §2.4 large ensembles of numerical solutions of equation (2.2) will be calculated using different numerical integration schemes. The accuracy of each numerical scheme, as a function of time-step Δt, will be assessed by comparison with the corresponding solution of the FPE, to be detailed next.

	$\sigma_w(z)$	$\tau_w(z)$	Modified $\bar{\sigma}_w(z)$	Modified $\bar{\tau}_w(z)$
Constant τ_w	$0.5\,(1+z)$	Constant	–	–
Stable	$1.3\,(1-z)$	$\dfrac{0.1z^{4/5}}{\sigma_w}$	$\sigma_w(Z_m(z))$	$\tau_w(Z_m(z))$
Neutral	$1.3\exp(-2z/\epsilon)$	$\dfrac{z}{2\sigma_w(1+15z/\epsilon)}$	$\sigma_w(Z_m(z))$	$\tau_w(Z_m(z))$

Table 2.1: The non-dimensional profiles of $\sigma_w(z)$ and $\tau_w(z)$ suitable for (i) a constant τ_w profile, (ii) a stable ABL, and (iii) a neutral ABL (e.g. Hanna, 1982). The non-dimensional parameter $\epsilon = u_*/fh$ is a boundary layer Rossby number (the value $\epsilon = 0.8$ is taken in the test case). For the purposes of numerical stability (see text), in practice the modified profiles $\bar{\sigma}_w(z)$ and $\bar{\tau}_w(z)$ are used, where $Z_m(z) = z_b + z(1-2z_b)$ is chosen to avoid singular behaviour at the boundaries ($z_b = 0.05$).

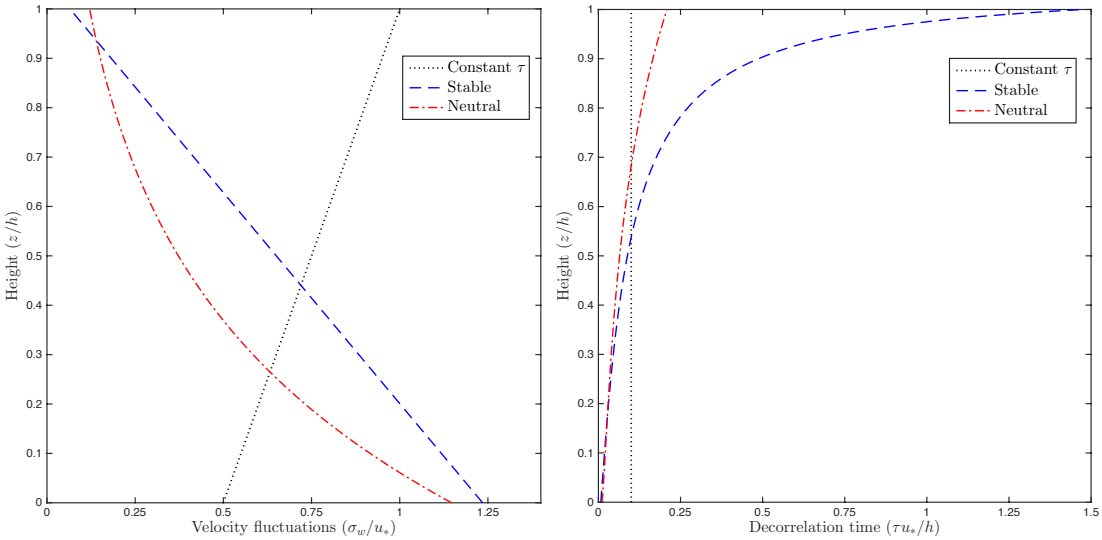

Figure 2.1: Vertical profiles of vertical velocity fluctuations $\bar{\sigma}_w(z)$ (left panel) and vertical velocity Lagrangian decorrelation time $\bar{\tau}_w(z)$ (right panel) used in the test-case problems (see Table 2.1). The dimensions for $\bar{\sigma}_w$ and $\bar{\tau}_w$ are frictional velocity u_* and h/u_* respectively, where h is the ABL height.

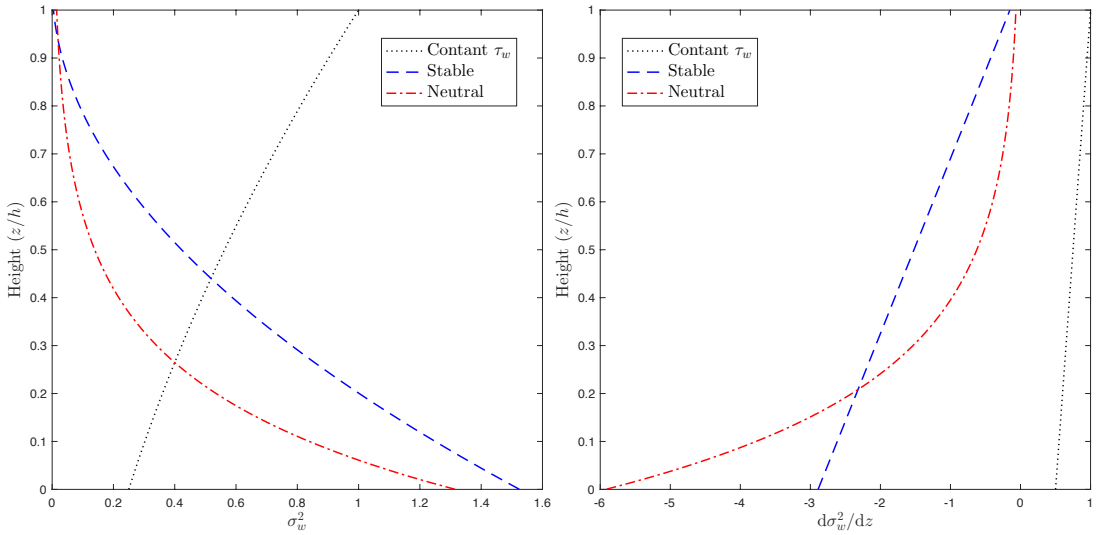

Figure 2.2: Vertical profiles of vertical velocity variances $\bar{\sigma}_w^2(z)$ (left panel) and their derivatives $\mathrm{d}\bar{\sigma}_w^2/\mathrm{d}z$ (right panel) used in the test-case problems (see Table 2.1).

2.2.2 FPE formulation

Following the standard procedure in stochastic calculus, (e.g. §3.4.1 of Gardiner, 2009), the FPE which describes the time evolution of the probability density $p(\omega, z, t)$ of (Ω_t, Z_t) in (2.2) can be obtained as

$$\frac{\partial p}{\partial t} = -\frac{\partial \left(\omega \sigma_w p\right)}{\partial z} - \frac{\partial}{\partial \omega}\left(\left(-\frac{\omega}{\tau_w} + \frac{\partial \sigma_w}{\partial z}\right) p\right) + \frac{1}{\tau_w}\frac{\partial^2 p}{\partial \omega^2}. \tag{2.3}$$

Explicitly, here $\omega = w/\sigma_w$. The initial conditions consistent with those given in eq. (2.2) are (for $\sigma_z \ll 1$ and z_0 not near the boundaries)

$$p(\omega, z, 0) = \frac{1}{2\pi\sigma_z} \exp\left(-\frac{\omega^2}{2} - \frac{(z - z_0)^2}{2\sigma_z^2}\right). \tag{2.4}$$

The FPE (2.3) also requires boundary conditions at $z = 0, 1$ which are consistent with the reflecting boundary conditions for the RFM. The boundary conditions consistent with reflection are

$$p(\omega, 0, t) = p(-\omega, 0, t), \quad p(\omega, 1, t) = p(-\omega, 1, t). \tag{2.5}$$

which in probabilistic terms is equivalent to the reflection condition $\Omega_t \to -\Omega_t$ being applied at the boundaries. Wilson et al. (1993) found that this perfect reflection algorithm is exactly consistent with the 'well-mixed constraint' in homogeneous Gaussian turbulence (see also the appendix of §11 of Rodean, 1996).

Equations (2.3)-(2.5) constitute a well-defined initial-value problem which is suitable for numerical solution. An important quantity obtained from the solution $p(\omega, z, t)$ is the physical concentration of parcels given by

$$c(z, t) = \int_{-\infty}^{\infty} p(\omega, z, t)\, \mathrm{d}\omega. \tag{2.6}$$

In general, tracer concentrations and the marginal probability given in eq. (2.6)

can differ by a normalisation constant. The concentration $c(z,t)$ will be our main benchmark quantity in §2.4 below.

2.3 Numerical solution of the FPE

2.3.1 The Hermite expansion for the FPE

The non-dimensionalised FPE (2.3) is a hypo-elliptic differential equation defined on $\mathbb{R} \times [0,1]$. Our approach to its numerical solution is to seek a solution based on the following Hermite polynomial expansion

$$p(\omega, z, t) = \frac{1}{\sqrt{2\pi}} \sum_{k=0}^{\infty} C_k(z,t)\, \mathrm{He}_k(\omega)\, \mathrm{e}^{-\omega^2/2}. \tag{2.7}$$

Here the functions $C_k(z,t)$ denote the projection, at the vertical level and time (z,t), of $p(\omega,z,t)$ onto the (probabilists') Hermite function $\mathrm{He}_k(\omega)\mathrm{e}^{-\omega^2/2}/\sqrt{2\pi}$ where $\mathrm{He}_k(\omega)$ is the Hermite polynomial defined by

$$\mathrm{He}_k(\omega) = (-1)^k\, \mathrm{e}^{\omega^2/2} \frac{\mathrm{d}^k}{\mathrm{d}\omega^k} \mathrm{e}^{-\omega^2/2}. \tag{2.8}$$

Notice that it follows that the particle concentration (2.6) satisfies $c(z,t) = C_0(z,t)$.

Before inserting the expansion (2.7) into the FPE (2.3) it is helpful to rewrite the FPE in the form

$$\frac{\partial p}{\partial t} = \frac{1}{\tau_w} \left(\frac{\partial^2 p}{\partial \omega^2} + \omega \frac{\partial p}{\partial \omega} + p \right) - \frac{\partial}{\partial \omega} \left(\frac{\partial \sigma_w}{\partial z} p \right) - \frac{\partial \left(\omega \sigma_w p \right)}{\partial z}. \tag{2.9}$$

In this form the Hermite function identity (A.3) can be used to evaluate the first term on the right-hand side. Further, the second and third terms on the right-hand side can be simplified using the derivative and recursion formulae for Hermite polynomials (A.6)-(A.7). After some working the result is (using the convention

$C_{-1} \equiv 0$)

$$\sum_{k=0}^{\infty} \mathrm{He}_k(\omega) \mathrm{e}^{-\omega^2/2} \left(\frac{\partial C_k}{\partial t} + \frac{k}{\tau_w} C_k + (k+1) \frac{\partial}{\partial z} \left(\sigma_w C_{k+1} \right) + \sigma_w \frac{\partial C_{k-1}}{\partial z} \right) = 0. \quad (2.10)$$

Using the orthogonality property of Hermite functions (A.4) it follows that

$$\begin{aligned} \frac{\partial C_0}{\partial t} &= -\frac{\partial}{\partial z} \left(\sigma_w C_1 \right) \\ \frac{\partial C_k}{\partial t} &= -\frac{k}{\tau_w} C_k - (k+1) \frac{\partial}{\partial z} \left(\sigma_w C_{k+1} \right) - \sigma_w \frac{\partial C_{k-1}}{\partial z}, \qquad \text{for } k \geq 1. \end{aligned} \quad (2.11)$$

The system (2.11) constitutes an infinite system of coupled 1+1 dimensional first-order partial differential equations for the coefficients C_k. For a numerical solution this series can be truncated as we describe below.

The initial conditions for (2.11) are easily obtained from (2.4) using the orthogonality property,

$$C_0(z,0) = \frac{1}{\sqrt{2\pi}\sigma_z} \exp\left(-\frac{(z-z_0)^2}{2\sigma_z^2} \right), \qquad C_k(z,0) = 0 \quad (\text{for } k \geq 1). \quad (2.12)$$

The boundary conditions can be obtained using the symmetry $\mathrm{He}_k(\omega) = (-1)^k \mathrm{He}_k(-\omega)$. Substituting the expansion (2.7) into the boundary condition (2.5), it follows that

$$\sum_{k \text{ odd}} C_k(z,t) \mathrm{He}_k(\omega) \frac{\mathrm{e}^{-\omega^2/2}}{\sqrt{2\pi}} = 0, \text{ at } z = 0, 1, \quad (2.13)$$

and consequently

$$C_k(0,t) = C_k(1,t) = 0, \quad \text{for } k \text{ odd}. \quad (2.14)$$

It may seem surprising that the even equations have no boundary condition and the odd equations take two boundary conditions. However, as the system (2.11) consists of *first-order* PDEs it is clear that the total number of boundary conditions will be correct, provided that the series is truncated at $k = K$ odd.

It is worth noting that the series (2.11) can also be truncated at $K = 0$ by using an (approximate) quasi-stationary balance in the $k = 1$ equation of the form

$$C_1 = -\sigma_w \tau_w \frac{\partial C_0}{\partial z}, \tag{2.15}$$

which results in the diffusion equation

$$\frac{\partial C_0}{\partial t} = \frac{\partial}{\partial z}\left(\sigma_w^2 \tau_w \frac{\partial C_0}{\partial z}\right), \quad \frac{\partial C_0}{\partial z}(0,t) = \frac{\partial C_0}{\partial z}(1,t) = 0. \tag{2.16}$$

It is well known that the RFM (2.1) can be approximated by a random walk ('random displacement' or RDM) model (see §1.3.3 for details)

$$\mathrm{d}Z_t = \frac{\partial}{\partial z}\left(\sigma_w^2 \tau_w\right) \mathrm{d}t + \left(2\sigma_w^2 \tau_w\right)^{1/2} \mathrm{d}B_t \tag{2.17}$$

Equation (2.16) is simply the FPE of the RDM model (2.17), with the diffusivity κ of the RDM being $\kappa = \sigma_w^2 \tau_w$. Note that the RDM model can be derived formally from the RFM in the distinguished limit of a short decorrelation time, $\sigma_w \to \infty$, $\tau_w \to 0$ with $\sigma_w^2 \tau_w = \kappa$ finite (for e.g. §6.3 of Rodean, 1996). It is much easier to obtain accurate solutions of (2.17), compared to (2.1) at relatively large time-steps; hence, an interesting question concerns when exactly it is preferable to solve (2.17) rather than (2.1). This question is best answered by quantifying the difference between the solution of (2.16) and (2.11) and using this difference as a benchmark for assessing the errors in RFM calculations, as will be done in §2.4 below.

2.3.2 The numerical method and benchmark solutions

Based on the analysis above, (2.3) can be solved numerically by integrating the system (2.11) with boundary conditions (2.14), truncated at $k = K$ odd.

Our approach is to use a standard finite-difference discretisation with N_z grid points, equally spaced with $\Delta z = 1/N_z$, on a staggered cell-centred grid (i.e. $z_i = (i - 1/2)\,\Delta z$, for $i = 1, \ldots, N_z$) in order to apply the boundary conditions at $z = 0, 1$ systematically, described as follows.

The FPE (2.3) is solved numerically by integrating (2.11) using the central finite difference method

$$\frac{\partial C_k}{\partial t}(z_i) = -\frac{k}{\tau(z_i)} C_k(z_i) - (k+1)\,\frac{\sigma_w(z_{i+1}) C_{k+1}(z_{i+1}) - \sigma_w(z_{i-1}) C_{k+1}(z_{i-1})}{2\Delta z} - \sigma_w(z_i)\frac{C_{k-1}(z_{i+1}) - C_{k-1}(z_{i-1})}{2\Delta z}. \quad (2.18)$$

Careful treatment is necessary at the boundaries. For k odd, the physical boundary conditions $C_k(0,t) = C_k(1,t) = 0$ imply the following substitutions for the values at the virtual points at $z = z_0$ and $z = z_{N_z+1}$,

$$C_{k_{\text{odd}}}(z_0) = -C_{k_{\text{odd}}}(z_1)$$
$$C_{k_{\text{odd}}}(z_{N_z+1}) = -C_{k_{\text{odd}}}(z_{N_z}).$$

For k even, the equation itself with k odd requires

$$C_{k_{\text{even}}}(z_0) = C_{k_{\text{even}}}(z_1)$$
$$C_{k_{\text{even}}}(z_{N_z+1}) = C_{k_{\text{even}}}(z_{N_z}).$$

These substitutions allow the right-hand side of eq. (2.18) to be expressed as a $N_z K \times N_z K$ matrix equation and completes the discretisation. The MATLAB source code of the FPE solver can be found online via GitHub and by searching for the repository "MRE FPE solver" (https://github.com/nhramli/MRE-FPEsolver.git).

The set (2.11) are stiff and a naive solution method would have the time-step Δt bounded above by $\Delta t \lesssim \text{Min}_z \tau_w(z)/K$, i.e. the timescale of exponential decay

of the highest Hermite function mode. However, considerably longer time-steps can be used if an exponential time-stepping scheme is chosen. Our choice is the 'Exponential Time-Differencing fourth-order Runge-Kutta' (ETDRK4) scheme of Kassam and Trefethen (2005), with the 'linear' operator in that scheme taken to be first term on the right-hand side of (2.11) only, because it is this first term that is responsible for the stiffness of (2.11).

To obtain our benchmark solutions of (2.11) and therefore (2.3), tests of the convergence of the solutions as both Δt and Δz are decreased and K is increased, have been performed. For all three case studies, it was found to be adequate to take $K = 19$ to obtain fully converged solutions, because the Hermite series was found to converge rapidly i.e. $|C_{19}| \lesssim 10^{-16}$ everywhere in the domain. Comparison of a sequence of solutions with $\Delta z = 1/N_z$ with $N_z = 2^7, 2^8, ..., 2^{12}$ revealed quadratic convergence with Δz as expected for our scheme. Fig. 2.3 shows the relative error $\mathcal{E}_j(t)$, with reference to the next-highest resolution solution, in the L_2-norm for the mean concentration $c(z,t)$ at fixed times, for the two test cases. That is,

$$\mathcal{E}_j(t) = \left(\int_0^1 \left(C_0^j(z,t) - C_0^{j+1}(z,t) \right)^2 \, \mathrm{d}z \right)^{1/2} \tag{2.19}$$

where $C_0^j(z,t)$ denotes the solution with $N_z = 2^j$. First convergence in L_2-norm (second-order in L_1-norm) is evident from the slope of the graphs in Fig. 2.3. For example, typical numerical errors at $N_z = 2^{12}$ (highest resolution) are $\mathcal{E}_{12}(t_1) = 9.7 \times 10^{-5}$ (stable boundary layer at $t_1 = h/u_*$) and 1.3×10^{-4} (neutral boundary layer at $t_1 = 3\,h/u_*$) respectively. The numerical accuracy above is sufficient for benchmarking our RFM solutions, because the statistical error associated with reasonable-sized ensembles ($N = 10^6$) of the RFM is of order $\mathcal{E}(t_1) \approx 10^{-2}$, as will be discussed below.

Figure 2.4 shows snapshots of the particle concentration $c(z,t)$ for each of the three FPE benchmark solutions described above. The left panel shows the constant

τ_w case, middle panel shows the stable ABL case and the right panel the neutral ABL. In all three cases particles are initialised close to $z = z_0 = 1/2$ and disperse to become well-mixed throughout the ABL at late times. The neutral and stable cases differ in that mixing is rather more rapid (in terms of the dimensional timescale h/u_*) for the stable case compared to the neutral case. Also, in the neutral case mixing is relatively slow towards the top the ABL where the amplitude of turbulent fluctuations decays exponentially.

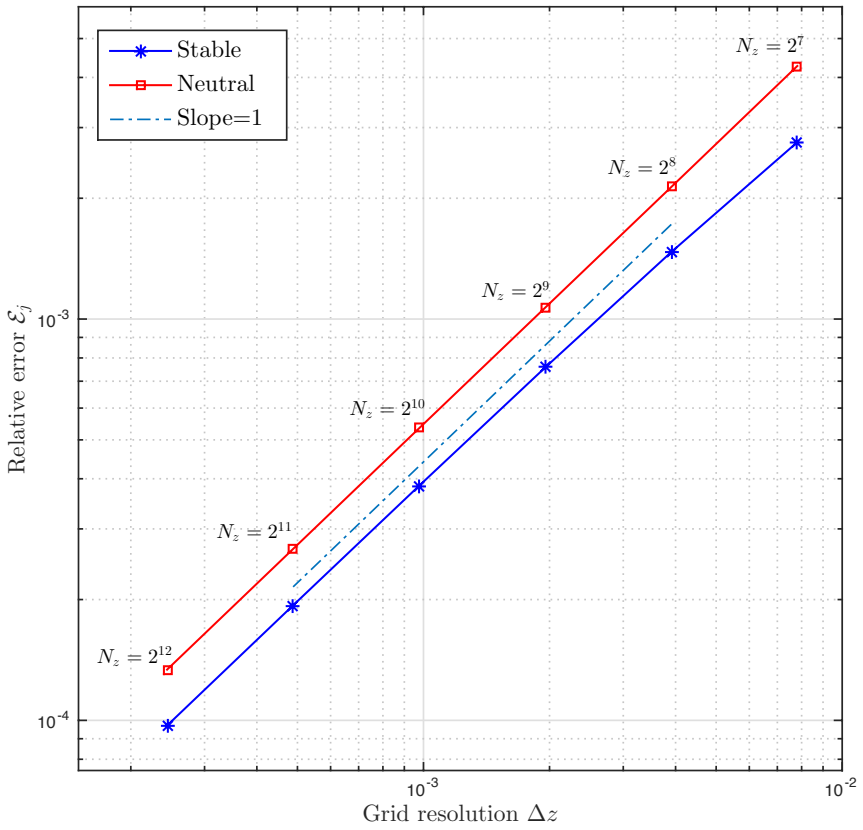

Figure 2.3: Relative error $\mathcal{E}_j$ (see eqn. 2.19) of the FPE solutions as a function of grid resolution $\Delta z = 2^{-j}$ for $j = 7, 8, ..., 12$ for the two test-case problems. Stars: stable ABL ($\mathcal{E}_j(t = 1)$). Squares: neutral ABL ($\mathcal{E}_j(t = 3)$).

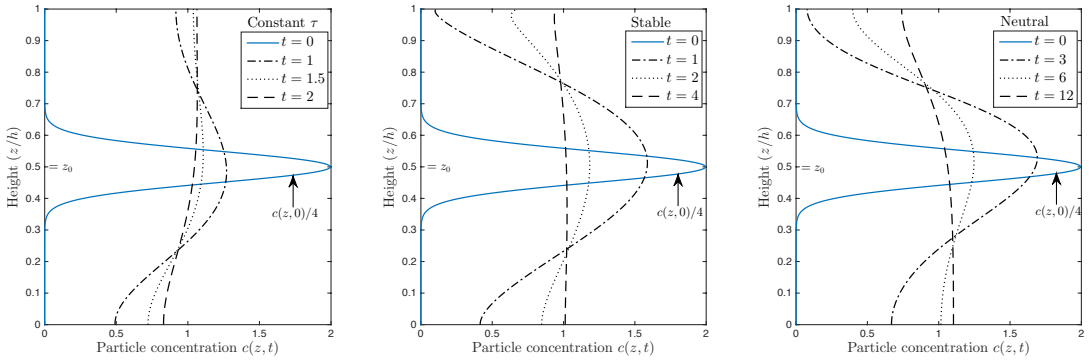

Figure 2.4: Snapshots of particle concentration $c(z,t)$ from the numerical FPE solutions for the three test-case problems. Left: Constant τ_w ($t = 0, 1, 1.5, 2\,h/u_*$). Center: Stable ABL ($t = 0, 1, 2, 4\,h/u_*$). Right: Neutral ABL ($t = 0, 3, 6, 12\,h/u_*$). For clarity $c(z,0)/4$ is plotted (instead of $c(z,0)$) for the initial condition at $t = 0$ in both panels.

2.4 Evaluation of numerical schemes for RFMs

In this section, a range of textbook, commonly used and new numerical schemes for RFMs will first be introduced, and then evaluated using the FPE solutions described above as a benchmark. The task is somewhat simplified because the equation set (2.2) is time-independent (autonomous). Note that it may be necessary to modify some of the schemes described below if an ABL with time-dependent statistics is to be modelled with the same formal accuracy (see the model problem studied in Chapter 4, for e.g.).

In the terminology of SDE numerical schemes, we are able to use 'weak' schemes (convergent in probability) in addition to 'strong' schemes (convergent in path), because we are primarily interested in the concentration of particles, which can be obtained from the pdf $p(\omega, z, t)$. In our type of model application, we are particularly interested in convergence in the weak sense, so that is what we will pay

most attention to when investigating the different numerical schemes. By definition (Kloeden and Platen, 1992), the discrete approximation $\overline{Z}_t$ using a given scheme is said to converge with weak order β to the solution Z_t of (2.2) as $\Delta t \to 0$ if for each positive polynomial g, there exists a positive constant k, such that

$$|\langle g(Z_t)\rangle - \langle g(\overline{Z}_t)\rangle| \leq k\,(\Delta t)^{\beta}.$$

The rate of convergence of a scheme, as measured by the quantities which depend on the pdf such as the concentration $c(z,t)$, with respect to the time-step Δt is known as its 'weak' order (see e.g. chapter 9 of Kloeden and Platen, 1992). The weak order is the relevant measure of comparison between schemes for our study, and should not be confused with the 'strong' order of a scheme, which refers to the rate of convergence of solution paths with respect to specific stochastic realisations.

It is important to note, however, that it is by no means obvious that a given scheme will attain its formal weak order when solving (2.2). This is because the assumptions under which the weak order of each scheme is derived are not met in the case of (2.2) because of the reflection boundary conditions. It is therefore necessary to solve (2.2) explicitly to assess each scheme.

2.4.1 RFM numerical schemes

Tables 2.2 - 2.3 summarise the SDE numerical schemes to be investigated. The first, most obvious scheme to test is the Euler-Maruyama (E-M) scheme (Maruyama, 1955), i.e. the simplest and lowest order time-stepping scheme for SDEs. Next, as with ordinary differential equations (ODEs), it is possible to construct schemes with higher orders of formal accuracy in the spirit of Runge-Kutta schemes for ODEs. Here we test the performance of Platen's 'explicit order 2.0 weak scheme' (EXPLICIT 2.0) and 'explicit order 3.0 weak scheme' (EXPLICIT 3.0) (see chapter 15 of Kloeden and Platen, 1992). In common with schemes for ODEs, higher order

schemes are somewhat more complicated to implement, and are more computationally expensive per time-step Δt. The advantage, however, is that the schemes have weak order Δt^2 (EXPLICIT 2.0) and Δt^3 (EXPLICIT 3.0) compared to Δt for E-M.

A single candidate from a second class of schemes, the so-called 'small-noise' schemes, to be investigated is the HON-SRKII scheme of Honeycutt (1992). Small-noise schemes typically have the same weak order (Δt) as E-M (see e.g. discussion in §3 of Milstein and Tretyakov, 2004), but the schemes are designed so that the leading-order error depends on the 'noise amplitude' in the equation, which in many practical situations is sufficiently small that higher-order convergence is observed in practice (at least for intermediate length time-steps, see discussion below). The HON-SRKII scheme will be shown below to converge with global error $\sim \Delta t^2$ in this intermediate time-step regime.

A third class of schemes to be investigated are designed to work well with long time-steps. Such schemes are of interest operationally, because the practical advantages of calculating large ensembles efficiently are thought to outweigh the disadvantage of loss of accuracy due to time-stepping errors. The model FLEXPART (Stohl et al., 2005), for example, switches between using E-M and a long time-stepping scheme due to Legg and Raupach (1982, LEGGRAUP). It is of some interest to verify that long time-stepping schemes such as LEGGRAUP do indeed outperform E-M at operationally relevant values of Δt. In fact, we review the derivation of the LEGGRAUP scheme in the next section, and show that additional care is needed to couple the velocity and position equations. A corrected scheme (LONGSTEP) is derived and is then compared with the schemes listed above in §2.4.2.

2.4.1.1 Derivation of LONGSTEP scheme

Here we derive a new long time-step scheme LONGSTEP. The scheme is designed to give acceptable results when integrating eq. (2.2) using time-steps $\Delta t \gtrsim \text{Min } \tau(z)$, for use in operational models. The starting point for the scheme is the velocity

update equation for the LEGGRAUP scheme (see Table 2.2)

$$\Omega_{n+1} = R_n\,\Omega_n + \sigma'_n\,\tau_n(1-R_n) + \left(1-R_n^2\right)^{1/2}\,\Delta_n, \tag{2.20}$$

where $\tau_n = \tau(Z_n)$, $\sigma'_n = (\partial\sigma_w/\partial z)(Z_n)$, $R_n = \exp\left(-\Delta t/\tau_n\right)$ and $\Delta_n \sim \mathcal{N}(0,1)$ is a random variable drawn from a Gaussian distribution with zero mean and unit variance. This scheme is obtained by first transforming (2.2) using Itô's lemma to obtain

$$\mathrm{d}\left(\Omega_t \mathrm{e}^{t/\tau}\right) = \mathrm{e}^{t/\tau}\frac{\partial\sigma_w}{\partial z}\,\mathrm{d}t + \mathrm{e}^{t/\tau}\left(\frac{2}{\tau}\right)^{1/2}\mathrm{d}B_t.$$

If both τ and $\partial\sigma_w/\partial z$ are taken to be constant (i.e. $\sigma_w(z) = \sigma_0 + \sigma'_0 z$) , this equation can be integrated to give

$$\Omega_t = \Omega_0\,\mathrm{e}^{-t/\tau} + \sigma'_0\,\tau(z)\left(1-\mathrm{e}^{-t/\tau}\right) + \left(\frac{2}{\tau}\right)^{1/2}\int_0^t \mathrm{e}^{(s-t)/\tau}\,\mathrm{d}B_s. \tag{2.21}$$

Stochastic integrals of the form

$$\int_0^t f(s)\,\mathrm{d}B_s \sim \mathcal{N}\left(0, \int_0^t f(s)^2\,\mathrm{d}s\right),$$

hence the final term in (2.21) can be replaced by a Gaussian random variable to give

$$\Omega_t = \Omega_0\,\mathrm{e}^{-t/\tau} + \sigma'_0\,\tau\left(1-\mathrm{e}^{-t/\tau}\right) + \alpha_1(t)\,\Delta_1, \tag{2.22}$$

where $\Delta_1 \sim \mathcal{N}(0,1)$ and $\alpha_1(t) = \left(1-\mathrm{e}^{-2t/\tau}\right)^{1/2}$. Equation (2.20) used by LEGGRAUP follows immediately from this solution.

The point where our analysis departs from that of Legg and Raupach (1982) is in the derivation of the position update. Under the approximation of linear σ_w the position equation of (2.2) is

$$\mathrm{d}Z_t = \Omega_t\,\left(\sigma_0 + \sigma'_0\,Z_t\right)\mathrm{d}t, \tag{2.23}$$

which, applying Itô's lemma, can be written as

$$\mathrm{d}\left(\log\left(\sigma_0 + \sigma_0' \, Z_t\right)\right) = \sigma_0' \, \Omega_t \, \mathrm{d}t \tag{2.24}$$

and integrated to obtain

$$\frac{1}{\sigma_0'}\left(\log\left(\sigma_0 + \sigma_0' \, Z_t\right) - \log\left(\sigma_0 + \sigma_0' \, Z_0\right)\right) = \int_0^t \Omega_s \, \mathrm{d}s. \tag{2.25}$$

The update equation used in LEGGRAUP, i.e. from Table 2.2,

$$Z_{n+1} = Z_n + \sigma_n \Omega_n \, \mathrm{d}t \tag{2.26}$$

would be correct (only in the limit $\sigma_0' \to 0$) in the event that Ω_s were a deterministic variable in the interval $0 \leq s \leq t$. However, Ω_s is a stochastic variable, hence it is a very crude approximation (error $O(t)$) to replace the integral on the right-hand side of (2.25) by $\Omega_0 t$ (which leads to the update eq. (2.26)). Instead, the integral needs to be considered carefully, as follows.

To evaluate the *stochastic* integral on the right-hand side of eq. (2.25) integral we can insert the solution (2.21) for Ω_s to obtain

$$\int_0^t \Omega_s \, \mathrm{d}s = \Omega_0 \, \tau \left(1 - \mathrm{e}^{-t/\tau}\right) + \sigma_0' \, \tau^2 \left(\frac{t}{\tau} - 1 + \mathrm{e}^{-t/\tau}\right) + \left(\frac{2}{\tau}\right)^{1/2} \int_0^t \int_0^s \mathrm{e}^{(q-s)/\tau} \, \mathrm{d}B_q \, \mathrm{d}s, \tag{2.27}$$

The final term can be evaluated following a switch in the order of integration

$$\int_0^t \int_0^s \mathrm{e}^{(q-s)/\tau} \, \mathrm{d}B_q \, \mathrm{d}s = \int_0^t \int_q^t \mathrm{e}^{(q-s)/\tau} \, \mathrm{d}s \, \mathrm{d}B_q = \tau \int_0^t \left(1 - \mathrm{e}^{(q-t)/\tau}\right) \, \mathrm{d}B_q = \tau^{3/2} \, \alpha_2(t) \, \hat{\Delta}_2. \tag{2.28}$$

where $\hat{\Delta}_2 \sim \mathcal{N}(0,1)$ and

$$\alpha_2(t) = \left(\frac{t}{\tau} - 2\left(1 - \mathrm{e}^{-t/\tau}\right) + \frac{1}{2}\left(1 - \mathrm{e}^{-2t/\tau}\right)\right)^{1/2}.$$

The issue for implementation is that the Gaussian random variables Δ_1 and $\hat{\Delta}_2$ are not independent. In fact, they have covariance given by

$$\mathbb{E}(\Delta_1\hat{\Delta}_2) \equiv \beta(t) = \frac{\sqrt{2}}{\tau^2\,\alpha_1(t)\,\alpha_2(t)}\int_0^t \mathrm{e}^{(s-t)/\tau}\left(1-\mathrm{e}^{(s-t)/\tau}\right)\,\mathrm{d}s = \frac{\left(1-\mathrm{e}^{-t/\tau}\right)^2}{\sqrt{2}\,\alpha_1(t)\,\alpha_2(t)}.$$

Independent random variables can be introduced by writing

$$\hat{\Delta}_2 = \beta(t)\,\Delta_1 + \left(1-\beta(t)^2\right)^{1/2}\Delta_2, \tag{2.29}$$

where Δ_1 and Δ_2 are independent with $\Delta_1, \Delta_2 \sim \mathcal{N}(0,1)$.

The explicit solution of (2.25) can therefore be written

$$Z_t = Z_0\exp\left(\sigma_0' S_0\right) + \frac{\sigma_0}{\sigma_0'}\left(\exp\left(\sigma_0' S_0\right)-1\right), \quad \text{where} \tag{2.30}$$

$$S_0 = \Omega_0\tau\left(1-\mathrm{e}^{-t/\tau}\right) + \sigma_0'\tau^2\left(\frac{t}{\tau}-1+\mathrm{e}^{-t/\tau}\right) + 2^{1/2}\alpha_2(t)\left(\beta(t)\,\Delta_1 + (1-\beta(t))^{1/2}\,\Delta_2\right)$$

The scheme LONGSTEP, given explicitly in Table 2.2, consists of the LEGGRAUP velocity update (2.20), and a position update obtained from the solution (2.30) by linearizing σ_w about the current position Z_n. Similar to E-M, LONGSTEP converges with weak error $\sim \Delta t$, however it is designed to perform better at long time-steps as is tested in §2.4.2.

2.4.1.2 RFM numerical boundary conditions

In the numerical implementation of RFM eq. (2.2), the reflection condition $\Omega_t \to -\Omega_t$ is applied at the bottom and top of the ABL, where $Z_t = 0$ and $Z_t = 1$ respectively. This means that perfect reflection at the boundaries is also assumed for the Z_t computation.

(i) At the end of every time step of the numerical scheme $t_j = j\,\Delta t$ ($j = 1, 2, 3, \ldots$), any 'illegal' particle $(\Omega^*_{t_j}, Z^*_{t_j})$ that crosses the boundaries, i.e. below $Z = 0$ or

Scheme	Algorithm	Reference and Notes
E-M	$\Omega_{n+1} = \Omega_n + F_n\,\Delta t + (2/\tau_n)^{1/2}\,\Delta B_n$ $Z_{n+1} = Z_n + \Omega_n \sigma_n\,\Delta t$	Maruyama (1955)
EXPLICIT 2.0	$\Omega_{n+1} = \Omega_n + \frac{1}{2}\,(F_n + F_\mu)\,\Delta t + \frac{1}{2}\left((2/\tau_n)^{1/2} + (2/\tau_\mu)^{1/2}\right)\,\Delta B_n$ $Z_{n+1} = Z_n + \frac{1}{2}\,(\Omega_n \sigma_n + \Omega_\mu \sigma_\mu)\,\Delta t$ $\Omega_\mu = \Omega_n + F_n\,\Delta t + (2/\tau_n)^{1/2}\,\Delta B_n,$ $Z_\mu = Z_n + \Omega_n \sigma_n\,\Delta t$	Sec. 15.1 of Kloeden and Platen (1992)
HON-SRKII	$\Omega_{n+1} = \Omega_n + \frac{1}{2}\,(F_n + F_\mu)\,\Delta t + (2/\tau_n)^{1/2}\,\Delta B_n$ $Z_{n+1} = Z_n + \frac{1}{2}\,(\Omega_n \sigma_n + \Omega_\mu \sigma_\mu)\,\Delta t$ $\Omega_\mu = \Omega_n + F_n\,\Delta t + (2/\tau_n)^{1/2}\,\Delta B_n,$ $Z_\mu = Z_n + \Omega_n \sigma_n\,\Delta t$	Honeycutt (1992)
LEGGRAUP	$\Omega_{n+1} = R_n\,\Omega_n + \sigma'_n\,\tau_n(1 - R_n) + \left(1 - R_n^2\right)^{1/2}\,\Delta_n$ $Z_{n+1} = Z_n + \sigma_n\,\Omega_n\,\Delta_n$ $R_n = \mathrm{e}^{-\Delta t/\tau_n}$	Legg and Raupach (1982)
LONGSTEP	$\Omega_{n+1} = R_n\,\Omega_n + \sigma'_n\,\tau_n(1 - R_n) + \left(1 - R_n^2\right)^{1/2}\,\Delta_n$ $Z_{n+1} = Z_n + \frac{\sigma_n}{\sigma'_n}\left(\exp\left(\sigma'_n\,S_n\right) - 1\right)$ $R_n = \mathrm{e}^{-\Delta t/\tau_n}$ $S_n = \Omega_n \tau_n\left(1 - \mathrm{e}^{-\Delta t/\tau_n}\right) + \sigma'_n \tau_n^2\left(\frac{\Delta t}{\tau_n} - 1 + \mathrm{e}^{-\Delta t/\tau_n}\right)$ $+ 2^{1/2}\alpha_{2n}(t)\left(\beta_n\,\Delta_{1n} + (1 - \beta_n)^{1/2}\,\Delta_{2n}\right)$ $\beta_n = \frac{(1-R_n)^2}{2^{1/2}\,\alpha_{1n}\alpha_{2n}}, \qquad \alpha_{1n} = (1 - R_n)^{1/2}$ $\alpha_{2n} = \left(\frac{\Delta t}{\tau_n} - 2\,(1 - R_n) + \frac{1}{2}\left(1 - R_n^2\right)\right)^{1/2}$	See §2.4.1.1

Table 2.2: The RFM numerical schemes investigated in §2.4. Here Δt is the time-step, $\Delta B_n \sim \mathcal{N}(0, \Delta t)$, $\Delta_n \sim \mathcal{N}(0, 1)$ and $\sigma_i = \sigma_w(Z_i)$, $\tau_n = \tau_w(Z_n)$. The drift function is denoted by $F_i = -\Omega_i/\tau_w(Z_i) + \sigma'_w(Z_i)$ where $i = n, \mu$.

Scheme	Algorithm	Reference and Notes
EXPLICIT 3.0	$\Omega_{n+1} = \Omega_n + F_n\,\Delta t + (2/\tau_n)^{1/2}\Delta B_n$ $+ \frac{1}{2}\left(F_\zeta^+ + F_\zeta^- - \frac{3}{2}F_n - \frac{1}{4}\left(\tilde{F}_\zeta^+ + \tilde{F}_\zeta^-\right)\right)\Delta t$ $+ \left(\frac{1}{\sqrt{2}}\left(F_\zeta^+ - F_\zeta^-\right) - \frac{1}{4}\left(\tilde{F}_\zeta^+ - \tilde{F}_\zeta^-\right)\right)\zeta\,\Delta C_n\,(2/\Delta t)^{1/2}$ $+ \frac{1}{6}\left(F_n + F_u - F_\zeta^+ - F_\rho^+\right)\left((\zeta+\rho)\,\Delta B_n\,(\Delta t)^{1/2} + \Delta t + \zeta\,\rho\left((\Delta B_n)^2 - \Delta t\right)\right)$ $Z_{n+1} = Z_n + \Omega_n\sigma_n\,\Delta t$ $+ \frac{1}{2}\left(\sigma_\zeta\left(\Omega_\zeta^+ + \Omega_\zeta^-\right) - \frac{3}{2}\Omega_n\sigma_n - \frac{1}{4}\tilde{\sigma}_\zeta\left(\tilde{\Omega}_\zeta^+ + \tilde{\Omega}_\zeta^-\right)\right)\Delta t$ $+ \left(\frac{\sigma_\zeta}{\sqrt{2}}\left(\Omega_\zeta^+ + \Omega_\zeta^-\right) - \frac{\tilde{\sigma}_\zeta}{4}\left(\tilde{\Omega}_\zeta^+ - \tilde{\Omega}_\zeta^-\right)\right)\zeta\,\Delta C_n\,(2/\Delta t)^{1/2}$ $+ \frac{1}{6}\left(\Omega_n\sigma_n + \Omega_u\sigma_u - \sigma_\zeta\left(\Omega_\zeta^+ + \Omega_\rho^-\right)\right)\left((\zeta+\rho)\,\Delta B_n\,(\Delta t)^{1/2} + \Delta t + \zeta\,\rho\left((\Delta B_n)^2 - \Delta t\right)\right)$ $\Omega_\phi^\pm = \Omega_n + F_n\,\Delta t \pm (2/\tau_n)^{1/2}(\Delta t)^{1/2}\phi$ $Z_\phi = Z_n + \Omega_n\sigma_n\,\Delta t$ $\tilde{\Omega}_\phi^\pm = \Omega_n + 2\,F_n\,\Delta t \pm (2/\tau_n)^{1/2}\,(2\,\Delta t)^{1/2}\,\phi$ $\tilde{Z}_\phi = Z_n + 2\,\Omega_n\sigma_n\,\Delta t$ $\Omega_u = \Omega_n + \left(F_n + F_\zeta^+\right)\Delta t + (2/\tau_n)^{1/2}\,(\zeta+\rho)\,(\Delta t)^{1/2}$ $Z_u = Z_n + \left(\Omega_n\sigma_n + \Omega_\zeta^+\sigma_\zeta\right)\Delta t$ where $\phi = \zeta, \rho$ and $P(\zeta = \pm 1) = P(\rho = \pm 1) = \frac{1}{2}$	Sec. 15.2 of Kloeden and Platen (1992)

Table 2.3: EXPLICIT 3.0 scheme tested in §2.4, with $\tau_n = \tau_w(Z_n)$, and $\sigma_i = \sigma_w(Z_i)$, $\tilde{\sigma}_\phi = \sigma_w(\tilde{Z}_\phi)$, where $i = n, u, \phi$. The drift function is denoted by $F_i = -\Omega_i/\tau_w(Z_i) + \sigma_w'(Z_i)$ or $\tilde{F}_\phi = -\tilde{\Omega}_i/\tau_w(\tilde{Z}_\phi) + \sigma_w'(\tilde{Z}_\phi)$. Here Δt is the time step and we use two correlated Gaussian random variables $\Delta B_n \sim \mathcal{N}(0, \Delta t)$ and $\Delta C_n \sim \mathcal{N}(0, (\Delta t)^3/3)$, with $E(\Delta B_n \Delta C_n) = (\Delta t)^2/2$.

above $Z = 1$, will be reflected back into the domain and its velocity direction is reversed, i.e. $\Omega_{t_j} = -\Omega^*_{t_j}$.

(ii) Higher-order schemes involve intermediate time-steps. Our treatment of intermediate time-steps is as follows. First, the z-domain is extended to $z \in (-\infty, \infty)$, by repeated reflection of the $\sigma_w(z)$ and $\tau(z)$ profiles in the boundaries. In this extended domain, all intermediate time-steps are completed according to the algorithm in question. Then, at the end of the completed time-step reflection, as detailed above, takes the particle back into the $z \in [0, 1]$ domain where necessary. The domain extension device thus uniquely determines an unambiguous treatment of reflection of particles near the boundaries in the higher weak order schemes EXPLICIT 2.0, HON-SRKII, EXPLICIT 3.0 detailed in Tables 2.2 and 2.3.

2.4.1.3 Measured error

The method used to compare the results from a particular scheme, at fixed time-step Δt, to the particle concentration $c(z, t)$ obtained from the numerical solution of the FPE, is as follows. First, a large ensemble (typically $N = 10^6$) of trajectories is calculated using the scheme under investigation. Next, the density of particles $\widehat{c}$ is reconstructed from the resulting ensemble $\{Z_t^{(i)},\ i = 1, ..., N\}$ using kernel density estimation

$$\widehat{c}(z, t; h_b) = \frac{1}{N h_b} \sum_{i=1}^{N} K\left(\frac{z - Z_t^{(i)}}{h_b}\right) + \text{‘image terms’}. \tag{2.31}$$

Here $h_b > 0$ is a (small) smoothing parameter known as the bandwidth, and ‘image terms’ refer to contributions from the images of trajectories, introduced to satisfy the boundary conditions. The function $K(\cdot)$ is the kernel function, and is non-negative with zero mean and has unit integral. Here we use a Gaussian kernel. Details, including how the optimal bandwidth $h_b = h_*$ is chosen in practice, are given in Chapter 4.

The error associated with a given scheme, at time-step Δt, is measured by the L_2-norm

$$\|c - \widehat{c}\|_2 = \left(\int_0^1 \left(c(z,t) - \widehat{c}(z,t;h_*) \right)^2 \, \mathrm{d}z \right)^{1/2}. \tag{2.32}$$

In practice the error (2.32) is effectively bounded below by the so-called *statistical error*, which is defined to be the expected value of $\|c - \widehat{c}\|_2$ in the event that the ensemble $\{Z_t^{(i)},\ i = 1, ..., N\}$ were sampled from the exact distribution $c(z,t)$ itself. It is important to emphasise that it is not possible, using our method, to investigate schemes with errors below the statistical error. The statistical error can of course be reduced by using a larger ensemble N, but convergence is slow as the dependency is $N^{-1/5}$, as discussed in Chapter 4 of the thesis.

In the results below, in the interests of reproducibility, the error is presented as a function of the fixed time-step Δt for each scheme. However, the schemes have different computational costs per time-step, which will depend on both the method of implementation of each algorithm, and on the machine used for the simulations. To give a rough idea of representative computational costs, in Table 2.4 the relative cost, measured with reference to the E-M scheme is shown for our calculations. Following best practice in large operational calculations (see e.g. Stohl et al., 2005), the random numbers used to simulate the Wiener processes are pre-calculated so the costs of their generation are not included in the comparison.

Scheme	Relative computational time
E-M	1.0
EXPLICIT 2.0	2.0
EXPLICIT 3.0	5.8
HON-SRKII	1.9
LEGGRAUP	1.2
LONGSTEP	1.5

Table 2.4: Computational clock times, measured relative to the E-M scheme, for all of the schemes detailed in Tables 2.2–2.3. The calculations are for $N = 10^6$ trajectories, with time-step $\Delta t = 10^{-3} h/u_*$ and integration time h/u_*, The computational times are obtained by taking the average of times elapsed in seconds from several simulations, coded in MATLAB, on a MacBook Pro with no other programs running.

Another possible computational saving comes from the use of variable time-steps. To test whether or not a significant computational saving is easily attainable, we have made some calculations in which $\Delta t \propto \tau_w$ (the local Lagrangian decorrelation time). Error results of E-M and HON-SRKII schemes with variable time-steps are shown in Fig. 2.5. For each scheme tested, the use of variable time-steps was found to lead to a computational saving of a factor of around two to three compared to fixed time-steps, with the schemes otherwise performing as detailed below. More details and derivation of variable time-stepping schemes can be found in the literature (see for examples Szepessy et al., 2001; Burrage and Burrage, 2003; Burrage et al., 2004).

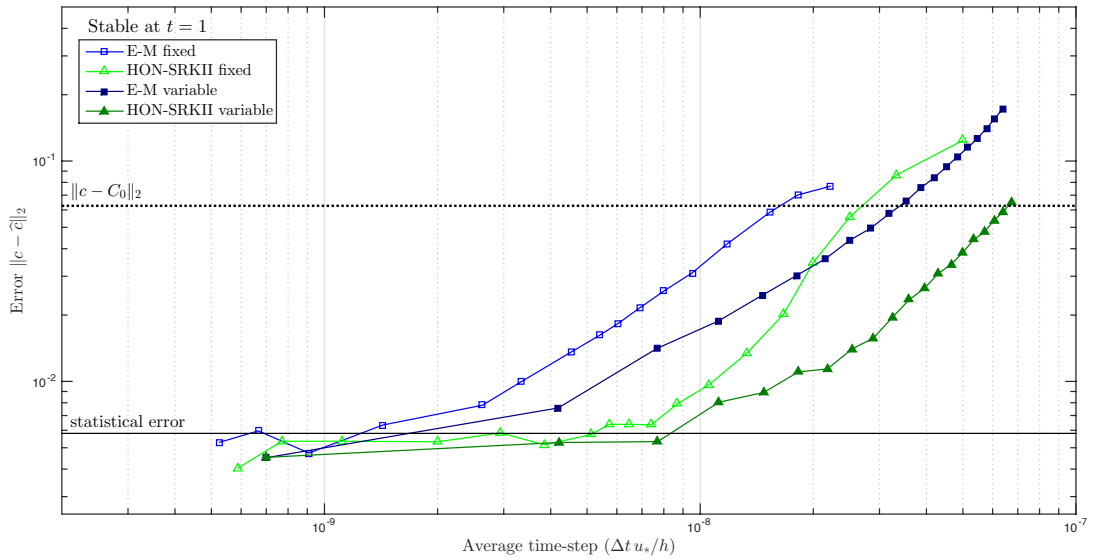

Figure 2.5: L_2-error against average time-steps $\Delta t\, u_*/h$ of the E-M and HON-SRKII schemes detailed in Table 2.2, using fixed time-steps Δt versus variable time-steps (i.e. $\Delta t \propto \tau_w(z)$). Results are calculated from $N = 10^6$ trajectories in the stable case with integration time h/u_*.

2.4.2 Results

The main results, showing the performance of the six schemes described in Tables 2.2 - 2.3 over a wide range of time-steps Δt, are shown in Figs. 2.6- 2.8. Figure 2.6- 2.8 detail the results for the constant τ_w test case, the stable ABL test case and the neutral ABL test case respectively (see Table 2.1). In each figure, the L_2-error (2.32) is plotted as a function of non-dimensional time-step $\Delta t\, u_*/h$. Logarithmic scales are used so that lines of constant slope corresponds to the observed order of the schemes. Blue lines with slopes 1, 2 and 3 are plotted for reference. The statistical error, which is the lowest possible error that can be measured for a given scheme, is plotted as a solid black line in each panel.

Also plotted on Figures 2.6 - 2.8, as a dotted black line, is the L_2-norm difference $\|c - C_0\|_2$ between the concentration field $c(z,t)$ obtained from the solution of the FPE (2.3) and $C_0(z,t)$ obtained from the diffusion equation (2.16). The dotted

black line marks an important boundary on each panel. If the time-step Δt is such that the error of a given scheme lies above this line, then it is preferable to solve the RDM (2.17) in place of (2.2), because (at fixed Δt) the numerical error for the former is more easily controlled.

Figure 2.6 shows results for the constant τ_w test-case at time $t = 1h/u_*$ (see Figure 2.4 and Table 2.1 for details). The lowest order schemes, LEGGRAUP (blue circles) and E-M (black squares) are seen to realise their formal weak order Δt. EXPLICIT 2.0 (red hexagons) and HON-SRKII (green solid triangles) have weak order Δt^2, whereas EXPLICIT 3.0 (blue triangles) has weak order Δt^3 as expected. The best performing scheme for this particular case is the new scheme LONGSTEP (purple diamonds) derived in §2.4.1.1. The rationale for LONGSTEP is that there is a conceptual error in the derivation of LEGGRAUP, which results in its performance at large Δt being no better than E-M. When this error is corrected in LONGSTEP, the performance is better than even EXPLICIT 3.0. LONGSTEP in effect uses exact solutions of the RFM equations for constant τ_w and linear σ_w, meaning that if the same calculations had been performed in an infinite domain, the numerical error would be zero. In the constant τ_w test case, errors in LONGSTEP arise only from the reflection boundary conditions at $z = 0, 1$. However, LONGSTEP does not fare well in the remaining two test-cases to be described next.

Figure 2.7 shows results for the stable ABL test case at intermediate time $t = h/u_*$ (upper panel) and at late time $t = 4\,h/u_*$ (lower panel), when the concentration is almost well-mixed across the ABL (see Figure 2.4). The results are similar to those of the constant τ_w case, except LONGSTEP (purple diamonds) now performs as poorly as E-M. Both E-M and LONGSTEP outperform LEGGRAUP. It was not found to be possible to obtain acceptable solutions for EXPLICIT 3.0 using time-steps longer than $\Delta t = 0.02\,h/u_*$ because of problems with reflective boundary conditions.

Figure 2.8 shows the results for the neutral ABL case at intermediate time

$t = 3\,h/u_*$ (upper panel) and at late time $t = 12\,h/u_*$ (lower panel). In this case the performance of LONGSTEP and LEGGRAUP are comparable, but with the E-M scheme performing better than both, except at very long time-steps where LEGGRAUP having slightly better accuracy at long time-steps. As for the previous test cases EXPLICIT 3.0 (blue triangles) scheme gives the lowest errors (weak order Δt^3), and EXPLICIT 2.0 (red hexagons) along with HON-SRKII (green solid triangles) perform consistently well with weak order Δt^2.

The typical time-step used by operational models such as FLEXPART (Stohl et al., 2005) is 900s in the 'long time-step' or 'global' mode. This is equivalent to $0.09 - 9\ h/u_*$ under our unit of time non-dimensionalisation, given that $h = 100 - 1000$ m is the ABL height and $u_* = 0.1 - 1$ ms^{-1} is surface friction velocity. According to our results in Figures 2.7 and 2.8, the time-step range $0.09 - 9\ h/u_*$ are too long and will show very small error difference between schemes, well above the L_2-norm difference $\|c - C_0\|_2$ error. At this point, the results are sufficiently inaccurate that it is better to use the RDM (2.17).

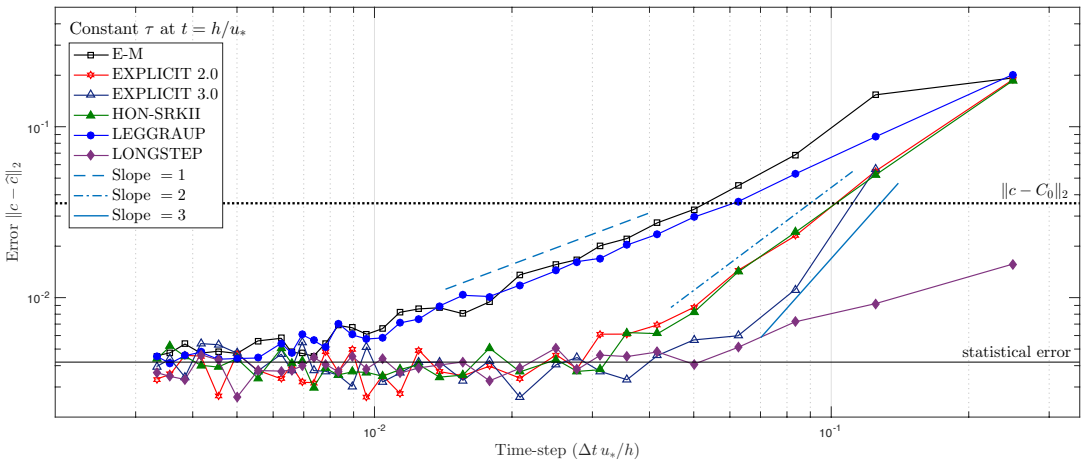

Figure 2.6: L_2-error (2.32) as a function of non-dimensional time-step $\Delta t\, u_*/h$ for the constant $\tau_w = 0.1$ test-case with $N = 10^6$ ensemble integrated at time $t = h/u_*$. The LONGSTEP scheme (purple diamonds) gives the best results in this case. Blue lines of slopes $1, 2$ and 3 are plotted for reference.

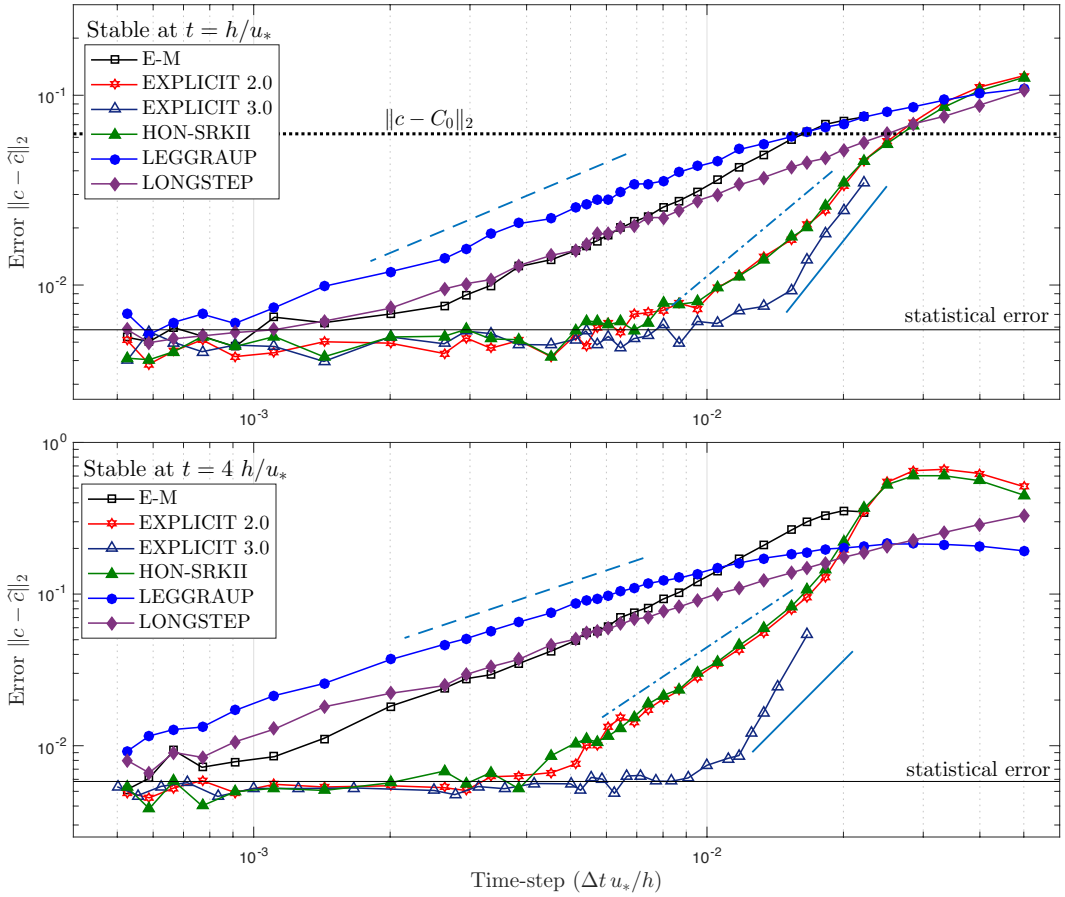

Figure 2.7: L_2-error (2.32) as a function of non-dimensional time-step $\Delta t\, u_*/h$ for the stable ABL test case integrated at intermediate time $t = h/u_*$ (upper panel) and at late time $t = 4\, h/u_*$ (lower panel). From left to right, blue lines of slopes $1, 2$ and 3 are plotted for reference.

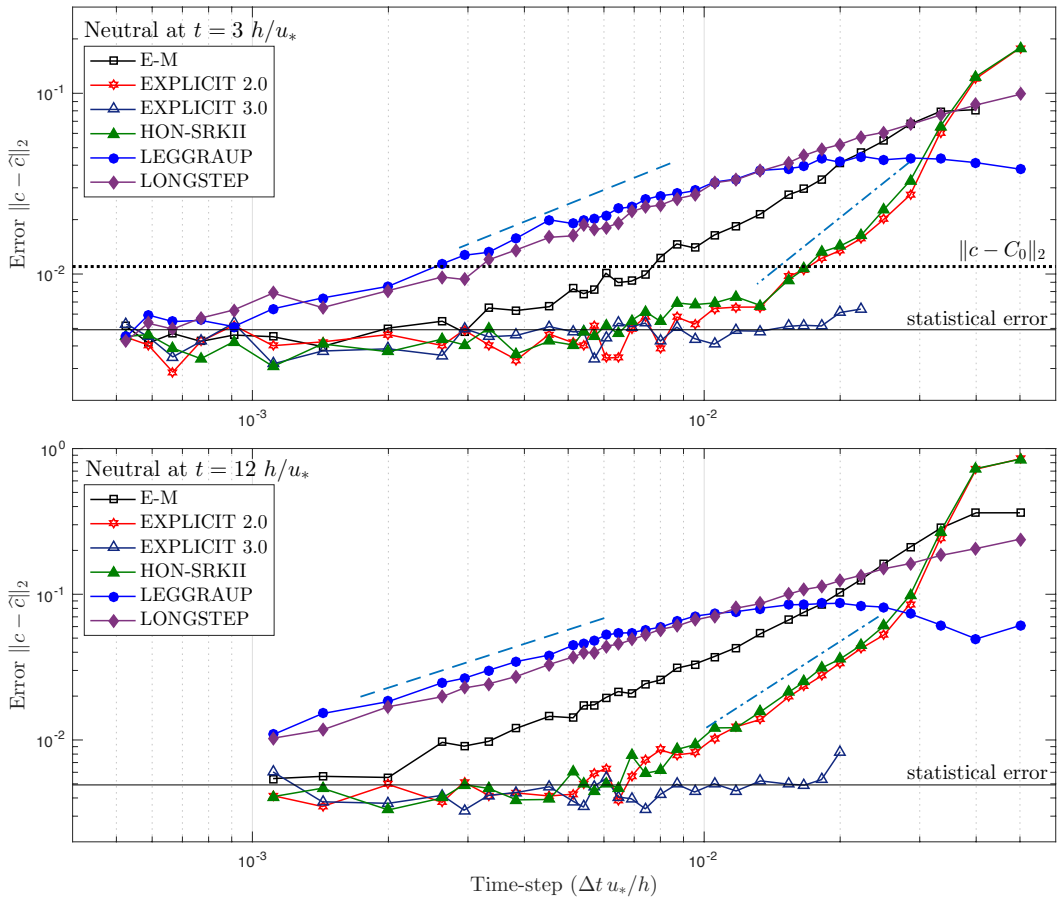

Figure 2.8: L_2-error (2.32) as a function of non-dimensional time-step $\Delta t\, u_*/h$ for the neutral ABL test case integrated at intermediate time $t = 3\, h/u_*$ (upper panel) and at late time $t = 12\, h/u_*$ (lower panel). From left to right, blue lines of slopes 1 and 2 are plotted for reference.

To give an impression of where the particle concentration errors are accumulating, Figure 2.9 shows snapshots of particle density $\widehat{c}(z,t)$ for the stable ABL case, at $t = h/u_*$. Results are shown for each scheme when a long time-step $\Delta t = 0.05\,h/u_*$ is used (left panel) and a moderate time-step $\Delta t = 0.007\,h/u_*$ (right panel). The errors in the long time-step case are large and are largely due to issues with the reflection of trajectories at the surface ($z = 0$). Numerical accuracy requires that $\Delta t \ll \tau_w$, which is evidently violated close to the boundary where $\tau_w(z)$ is small (see Fig. 2.1). Errors due to reflection are particularly acute for the higher order schemes (such as EXPLICIT 2.0 and HON-SRKII) that require the treatment of an intermediate step(s). See the discussion in §2.4.1.2 for how this step is implemented. The stable boundary layer case, where τ_w decays most rapidly near the $z = 0$ boundary, is the case which appears to be the most sensitive to the treatment of reflection there.

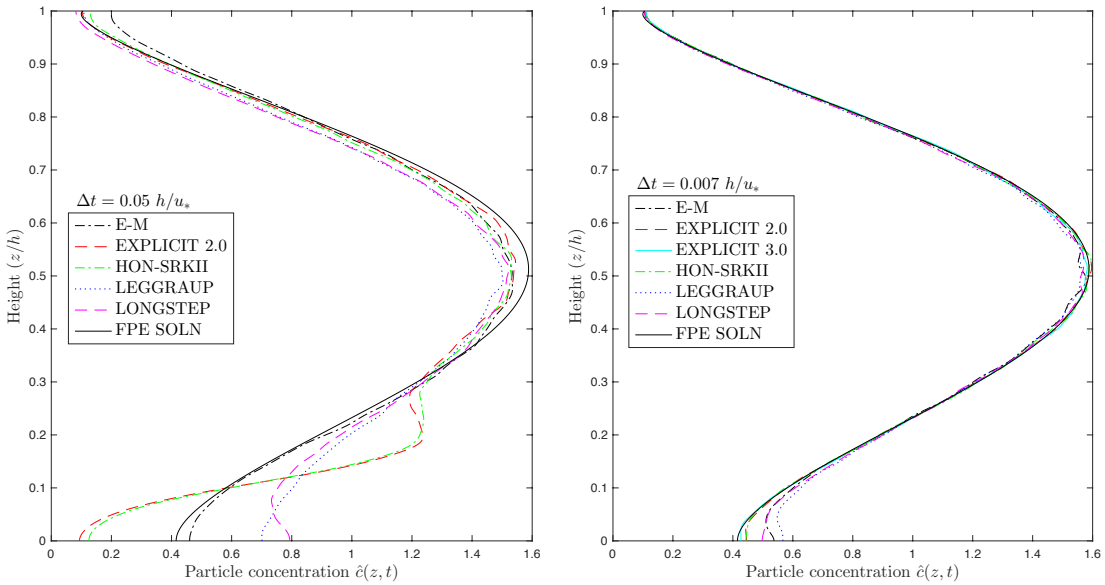

Figure 2.9: Snapshots of reconstructed particle density $\widehat{c}(z,t)$ for the stable ABL case at time $t = h/u_*$, shown at each scheme. Left: when long time-step $\Delta t = 0.05\,h/u_*$ is used and errors due to boundary conditions dominate. Right: when moderate time-step $\Delta t = 0.007\,h/u_*$ is used.

2.5 Conclusions

The main contribution of this chapter is to introduce a protocol for the quantitative assessment of SDE numerical schemes, applied to the problem of dispersion in an idealised atmospheric boundary layer, as modelled by RFMs. Accurate solutions of the Fokker-Planck equation (FPE (2.3)) are used to benchmark the distribution obtained from an ensemble of RFM solutions obtained using a particular scheme with a fixed time-step Δt. By using the FPE solution, our protocol avoids the possibility of the RFMs exhibiting spurious convergence to an incorrect distribution as $\Delta t \to 0$ (e.g. by a poor treatment of reflection boundary conditions), and the FPE provides independent verification of the correctness of a specific implementation.

The convergence results obtained in our model test problems are valuable because, due to the importance of reflection of particles from the surface and top of the boundary layer, it is not possible to rely on the formal convergence rates of different SDE schemes (as given by e.g. Kloeden and Platen, 1992). All of the schemes tested attain their formal convergence rates at early times in the model test problem, i.e. before reflection becomes important, and thereafter are limited to an extent by the details of how reflection is implemented (§2.4.1.2).

Our results allow the following recommendations to be made, for consideration by operational modellers:

1. For our test problems, the best results with respect to accuracy as a function of Δt were obtained with the weak order Δt^3 scheme EXPLICIT 3.0. However, this scheme is time-consuming to implement and more expensive per step compared to the weak order Δt^2 schemes investigated, so the gains associated with it are marginal. A good compromise between ease-of-implementation, flexibility and accuracy is the 'small-noise' scheme of Honeycutt (1992, here HON-SRKII). Formally, the weak order of HON-SRKII is just Δt, i.e. the same as Euler-Maruyama. However, the scheme designed so that at fixed Δt, in the

limit of small-noise the weak error scales with Δt^2 (e.g. Chap. 3 of Milstein and Tretyakov, 2004). Although the boundary layer dispersion problems examined here are not formally 'small-noise' problems, our results show clearly that they behave as such in a practical implementation. As a consequence HONSRKII scheme performs at least as well as the formally weak order Δt^2 scheme EXPLICIT 2.0 (which in fact has a very similar implementation for the specific RFM problem we have examined here).

2. The 'long-step' scheme due to Legg and Raupach (1982, here LEGGRAUP), which is used operationally for global integrations of trajectories in FLEXPART (for example), should be avoided. LEGGRAUP does not significantly outperform Euler-Maruyama at any time-step for any of the three profiles we have studied. The reason for this is a conceptual error in its derivation, which we have corrected here in the development of a new scheme LONGSTEP, see §2.4.1.1. LONGSTEP performs very well in the case of $\tau_w(z)$ =constant, but no better than LEGGRAUP for other $\tau_w(z)$ profiles, hence we do not recommend it for operational use either.

3. Global calculations often require the use of long time-steps for reasons of computational efficiency. For such calculations, we recommend switching to the random displacement model (2.17), rather than solving the RFM equations (2.2). The reason for this recommendation is apparent in Figures 2.6 - 2.8 where the numerical error for all of the schemes investigated is seen to exceed the difference between RDM and RFM solutions when the time-step $\Delta t \gtrsim 0.02\, h/u_*$. Given that the unit of time in our non-dimensionalisation is $T = h/u_*$, where $h = 100 - 1000$ m is boundary layer height and $u_* = 0.1 - 1$ ms^{-1} is surface friction velocity, for a typical $T \approx 1000$s errors will be minimized by using the RDM whenever a time-step $\Delta t \gtrsim 20$ s is required.

Naturally, the recommendations above are based only on the limited set of

schemes which we have studied. It is to be hoped that the protocol and test cases introduced here will be helpful to other researchers developing and testing novel methods for RFMs. A key challenge in such development will be the careful treatment of reflection boundary conditions, including their generalisation to more complex physical situations (e.g. Wilson and Flesch, 1993; Thomson et al., 1997; Wilson and Yee, 2007).

Chapter 3

Shear dispersion in the turbulent atmospheric boundary layer

3.1 Introduction

Shear dispersion, sometimes referred to as Taylor or Taylor-Aris dispersion, describes a fundamental process in fluid dynamics. It was first recognised by Taylor (1953) who investigated the dispersion of a passive tracer by laminar Poiseuille flow through a pipe, then later by Aris (1956) who treated the same problem but used a different analytical approach. The main feature of shear dispersion is that the rate dispersal of a tracer in the of along-flow (longitudinal) direction is influenced, not by the direct diffusion acting in the along-flow direction, but by the diffusion in the across-flow (lateral) direction acting simultaneously with the shear in the flow. More interestingly, the dominant term in the effective diffusivity in the along-flow direction is found to be *inversely* proportional to the across-flow diffusivity. This is because when the across-flow diffusivity is weak, individual fluid particles experience coherent differential advection by the shear flow for long periods, compared to when the across-flow diffusivity is strong. On the other hand, in the limit of

strong across-flow diffusivity the particles experience (non-dispersive) advection by the mean flow only.

Shear dispersion in the context of ABL flows has long been recognised. The classic paper of Saffman (1962) derived analytical solutions for two idealized problems of vertical diffusion in the atmosphere. The first problem is bounded to a fixed boundary layer height where a no-flux boundary condition is imposed and the second problem is unbounded. Subsequent researchers (e.g. Smith, 1965; Tyldesley and Wallington, 1965; Taylor, 1982; Smith, 2005) have mainly focussed on the paradigm presented by the second solution, which is relevant to the early stages of a tracer release problem in which a near-Gaussian tracer plume or puff spreads freely in the vertical, interacting only with the surface.

The present work[1], by contrast, is motivated in part by the desire to understand shear dispersion in state-of-the-art LPDMs such as FLEXPART (Stohl et al., 2005) and NAME (Jones et al., 2007). In these models a no-flux (or particle reflection) boundary condition is imposed at the top of ABL as in Saffman's (1962) first problem above. After a time period of the order of h/u_* where h is the boundary layer height and u_* the surface friction velocity, particle concentrations become homogenised in the vertical. Shear dispersion over the ABL depth then follows after this homogenisation period. Since h/u_* in the ABL is typically of the order of tens of minutes, the practical relevance of Saffman's (1962) first problem to the horizontal spread of tracers released in the ABL is evident over a period of a few hours. Figure 3.1 shows a diagram of turbulent tracer dispersal in a LPDM with spatially non-uniform turbulence statistics (e.g. Lagrangian decorrelation time and velocity fluctuations) interacting with a shear flow in a bounded model of the ABL.

Figure 3.2 displays snapshots in time of an ensemble of trajectories in one of the RFM calculations. The first panel shows the ensemble scatterplot at $t = 0.2\ h/u_*$

[1]Based on this chapter, a paper co-written with J.G. Esler is to be submitted to the Quarterly Journal of the Royal Meteorological Society.

just before the particle distribution become vertically homogenised (or well-mixed) in the second panel after $t = 2\ h/u_*$. In this chapter, we will be interested in the horizontal spread of the tracer particles as measured by the variance $\langle (X_t - \langle X_t \rangle)^2 \rangle^{1/2}$ (where the angle brackets denote ensemble average) in the late time $t = 20\ h/u_*$ evolution, indicated in the third panel.

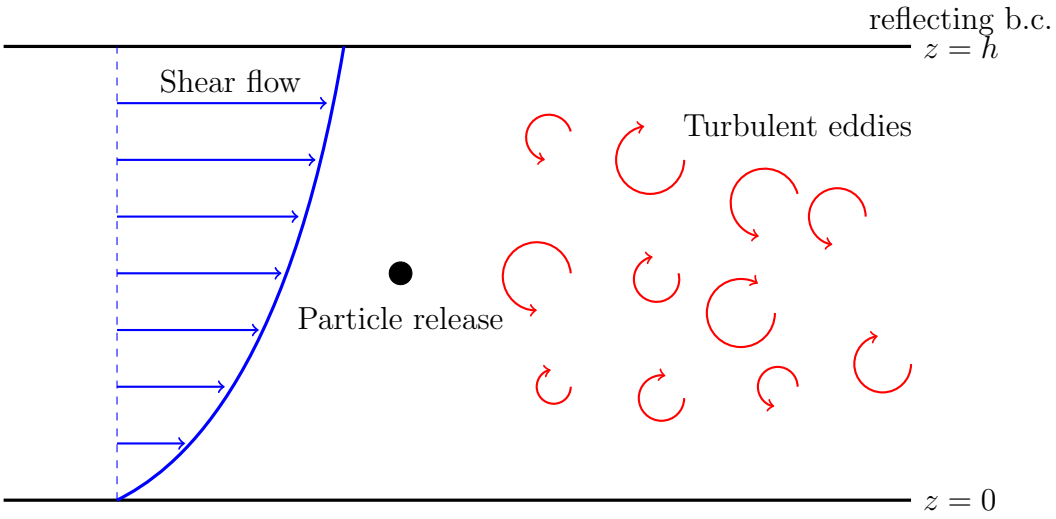

Figure 3.1: Schematic example of spatially varying ABL turbulent statistics in a shear dispersion flow. The particle diffusion is bounded at the top of the ABL ($z = h$) and at the bottom ground surface ($z = 0$).

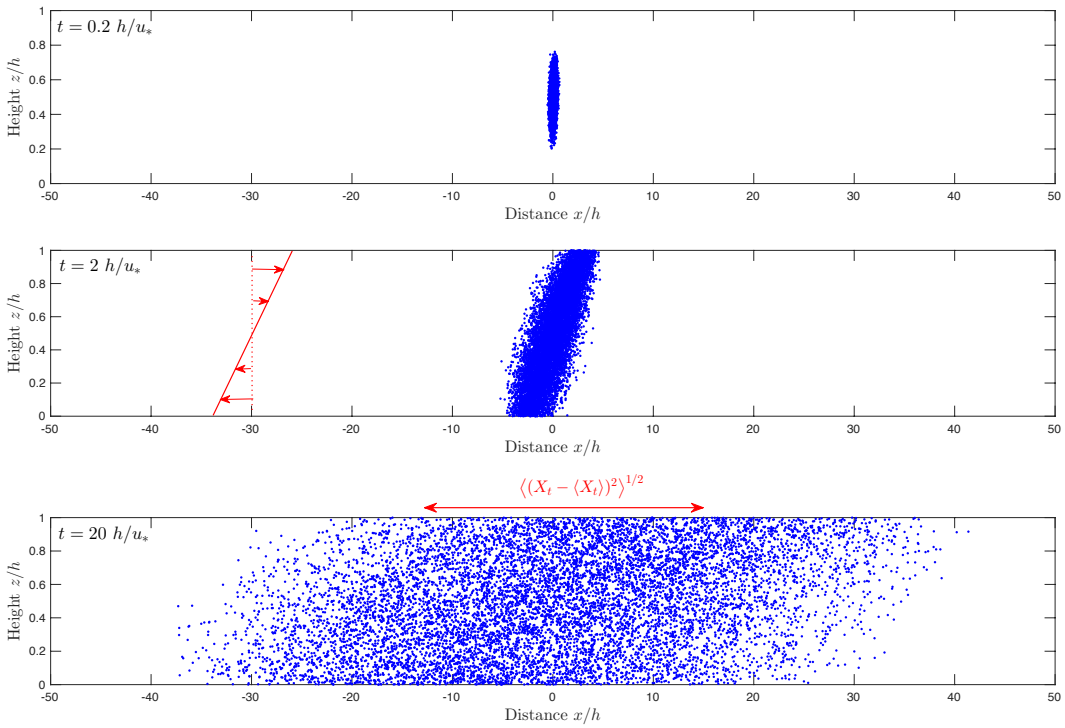

Figure 3.2: Scatterplots of an ensemble of trajectories in the stable ABL case. First panel: early time $t = 0.2\ h/u_*$ snapshot. Second panel: particles become wel-mixed at intermediate time $t = 2\ h/u_*$. Third panel: snapshot at late time $t = 20\ h/u_*$ when shear dispersion ensues. The measure of interest is the horizontal variance $\langle (X_t - \langle X_t \rangle)^2 \rangle^{1/2}$ which translates to the *central region* of the particle distribution.

Saffman's (1962) main result for the ABL one-dimensional problem with a height-dependent isotropic diffusivity $\kappa(z)$ and shear flow $u(z)$, after the homogenization period described above, is as follows. The vertical mean concentration

$$[c](x,t) = \int_0^h c(x,z,t)\ \mathrm{d}z,$$

evolves according to the one-dimensional advection-diffusion equation

$$\partial_t[c] + [u]\ \partial_x[c] = \kappa_{\mathrm{eff}}\ \partial^2_{xx}[c], \tag{3.1}$$

where $[\cdot]$ here denotes the average over the vertical depth of the ABL. Saffman's (1962) result for the effective diffusivity κ_{eff} is found to be

$$\kappa_{\mathrm{eff}} = \left[\frac{F^2}{\kappa} + \kappa\right], \quad \text{where} \quad F(z) = \int_0^z (u(\bar{z}) - [u])\ \mathrm{d}\bar{z}. \tag{3.2}$$

In practice κ_{eff} is dominated by the first term on the right-hand side which depends on the the inverse of the eddy diffusivity $\kappa(z)$, as expected by the discussion above. In the present work, we shall examine the application of Saffman's (1962) first solution to the shear dispersion process in the LPDMs designed for the ABL (e.g. FLEXPART and NAME). Specifically, we will address the following aspects:

1. The effect on κ_{eff} when RFMs are used instead of RDMs. Both FLEXPART and NAME are RFMs, which are stochastic models of the turbulent diffusion that include a finite Lagrangian decorrelation time for the turbulent velocity field. However the results of Saffman (1962) apply directly only to RDMs, which correspond to both the limit of zero decorrelation time of the RFM (e.g. Rodean, 1996), and the standard advection-diffusion model.

2. The difference between the large-deviation behaviour of the RFM and that of the RDM. Large deviation theory studies the evolution of the low concentra-

tions seen in the tails of a spreading cloud of parcels (Haynes and Vanneste, 2014), and can be important in estimating the time-scale on which a threshold concentration is met at a given location downstream.

The two questions above will be answered by comparing analytical, semi-analytical and numerical results. In §3.2, the RFM and RDM models are introduced, and the large-deviation analysis of the RDM (Haynes and Vanneste, 2014) is briefly described. In §3.3, we extend the large-deviation approach to the RFM, and analytical and numerical methods to obtain the effective horizontal diffusivity are discussed. In §3.4, a numerical approach using the Hermite function expansion to solve the eigenvalue problem which arises in the large-deviation theory is presented and numerical results for the large-deviation rate function. In §3.5, the predictions of §3.3 are compared with numerical calculations of large ensembles of tracer particles in both the RFM and RDM. The differences between the two models are investigated in both stable and neutral ABL conditions. To further validate our results, a GWTW splitting method is implemented using our large-deviation predictions in rare-event simulations in §3.6. Finally in §3.7, conclusions are drawn.

3.2 Model and background

In the LPDMs to be investigated, we consider two-dimensional turbulent ABL of uniform density, and a given air parcel is moving along the (x, z)-axes with a parallel shear flow $\boldsymbol{u} = (u(z), 0)$. For the purposes of this work, the LPDMs are non-dimensional, with length, velocity and time scales of boundary layer height h, surface friction velocity u_* and h/u_* respectively. Under this scaling, the spatial domain for the LPDMs is $0 \leq z \leq 1$. The vertical mean of the horizontal velocity flow $[u(z)]$ is assumed to be zero,

$$[u] = \int_0^1 u(z)\,\mathrm{d}z = 0, \tag{3.3}$$

which allows us to work in a frame following the mean of the ensemble of particle trajectories.

For most of the numerical results below, we have chosen a horizontal velocity flow to be linear in the vertical direction, i.e. $u(z) = U_0(z - 0.5)$ which is displayed in Figure 3.3 below. Note that this picture is the Galilean transformation of the shear flow in accord with the ensemble mean frame of reference mentioned above. The mean velocity profile $u(z)$ will typically have a large magnitude (measured in units of u_*), i.e. the parameter $U_0 = U_{\max} - U_{\min}$, where $U_{\max}$ and $U_{\min}$ are the maximum and minimum physical velocities respectively, is usually $O(10)$ or greater.

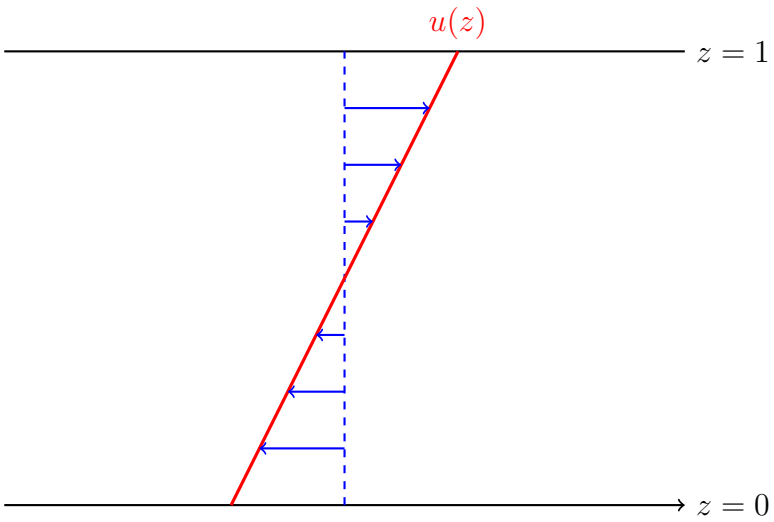

Figure 3.3: The zero mean of the horizontal velocity profile for $u(z) = U_0(z - 0.5)$.

3.2.1 The random flight model

Consider the RFM which is defined by the following set of SDEs describing the time evolution of the position (X, Z) and eddy velocity (U, W) of a single fluid parcel in a turbulent boundary layer with Gaussian velocity statistics. Note for simplicity in this chapter, we drop the subscripts t from (X_t, Z_t, U_t, W_t) to denote

the stochastic variables at time t (unless specified otherwise).

$$\begin{aligned}
\mathrm{d}U &= \frac{-U}{\tau_u}\,\mathrm{d}t + \left(\frac{2\sigma_u^2}{\tau_u}\right)^{1/2}\mathrm{d}B_u, \\
\mathrm{d}W &= -\frac{W}{\tau_w}\,\mathrm{d}t + \frac{1}{2}\left(1+\left(\frac{W}{\sigma_w}\right)^2\right)\frac{\mathrm{d}(\sigma_w^2)}{\mathrm{d}z}\,\mathrm{d}t + \left(\frac{2\sigma_w^2}{\tau_w}\right)^{1/2}\mathrm{d}B_w, \qquad (3.4)\\
\mathrm{d}X &= (u(z)+U)\,\mathrm{d}t, \\
\mathrm{d}Z &= W\,\mathrm{d}t,
\end{aligned}$$

where (B_u, B_w) are the two-dimentional Brownian (or Wiener) processes, with subscripts u and w referring to the horizontal and vertical directions respectively. The turbulent statistics are specified by the turbulent velocity scales $(\sigma_u(z), \sigma_w(z))$, and Lagrangian decorrelation times $(\tau_u(z), \tau_w(z))$. The mean horizontal velocity flow is $u(z) = U_0(z - 0.5)$ discussed above.

The physical interpretation and discussion of the different terms in (3.4) is given in §1.3.2. Equation (3.4) is essentially that used in FLEXPART (Stohl et al., 2005) and NAME (Jones et al., 2007) to model dispersion in the ABL. Following these models, reflection boundary conditions are used at the model boundaries at $z = 0, 1$. Physically, reflection at the boundary layer top ($z = 1$) is (at least partially) justified when the ABL has locally developed a sharp gradient in buoyancy, forming an interface across which there is a large decrease in the intensity of turbulence. See Wilson et al. (1993) and Thomson et al. (1997) for discussion, including the possibility of more sophisticated boundary conditions.

Following Rodean (1996) and also discussed in §2.2, it is easier to work with scaled velocities $(\Lambda, \Omega) = (U/\sigma_u(Z), W/\sigma_w(Z))$ which following application of Itô's

lemma, satisfy

$$\begin{aligned}
\mathrm{d}\Lambda &= -\frac{\Lambda}{\tau_u}\mathrm{d}t + \left(\frac{2}{\tau_u}\right)^{1/2} \mathrm{d}B_u, \\
\mathrm{d}\Omega &= \left(-\frac{\Omega}{\tau_w} + \frac{\mathrm{d}\sigma_w}{\mathrm{d}z}\right)\mathrm{d}t + \left(\frac{2}{\tau_w}\right)^{1/2} \mathrm{d}B_w, \\
\mathrm{d}X &= (u + \Lambda\,\sigma_u)\ \mathrm{d}t, \\
\mathrm{d}Z &= \Omega\,\sigma_w\,\mathrm{d}t.
\end{aligned} \tag{3.5}$$

For ease of comparison with the FPE, the initial positions, are sampled from the Gaussian distribution of mean (x_0, z_0) and standard deviation (σ_x, σ_z), and the initial scaled velocities are sampled from the standard normal distribution,

$$X_0 \sim \mathcal{N}(x_0, \sigma_x^2), \quad Z_0 \sim \mathcal{N}(z_0, \sigma_z^2), \quad \Lambda_0 \sim \mathcal{N}(0,1), \quad \Omega_0 \sim \mathcal{N}(0,1). \tag{3.6}$$

The complimentary approach to the system of SDEs such as (3.5) is to consider the corresponding FPE (see §1.2.2 for the standard procedure) that describes the evolution of the joint probability density $p(x, z, \lambda, \omega, t)$ of stochastic variables (X, Z, Λ, Ω), which is found to be

$$p_t + ((\lambda\,\sigma_u + u)\,p)_x + (\omega\sigma_w p)_z + (\sigma_w' p)_\omega = \tau_u^{-1}\left(\partial_\lambda + \lambda p\right)_\lambda + \tau_w^{-1}\left(\partial_\omega + \omega\,p\right)_\omega . \tag{3.7}$$

Here the subscripts denote partial derivatives, $\sigma_w' \equiv \mathrm{d}\sigma_w/\mathrm{d}z$ and explicitly, $\lambda = u/\sigma_u$ and $\omega = z/\sigma_w$. It should be emphasised that

$$p_e = \text{constant} \times \exp\left(-\frac{1}{2}\left(\lambda^2 + \omega^2\right)\right), \tag{3.8}$$

is the steady solution of (3.7). The solution p_e, or in the language of probability theory the invariant measure of (3.4), is interpreted physically as the distribution of particles in the background atmosphere in position-velocity space. As already

discussed in §1.3.1, the WMC of Thomson (1987) corresponds to ensuring that the invariant measure of the system of SDEs being solved corresponds to a notional, pre-specified distribution p_e, which is determined by the statistics of the background atmosphere.

The initial conditions consistent with those specified in (3.6) are therefore given by

$$p(\lambda,\omega,x,z,0)=\frac{1}{4\pi^2\sigma_x\sigma_z}\exp\left(-\frac{\lambda^2+\omega^2}{2}-\frac{(x-x_0)^2}{2\sigma_x^2}-\frac{(z-z_0)^2}{2\sigma_z^2}\right). \tag{3.9}$$

Moreover, the boundary conditions for FPE (3.7) at $z=0,1$ must also be exactly consistent with the WMC, as discussed in the introductory §1.3.6. Hence the perfect reflection boundary conditions can be written in the form

$$p(\lambda,\omega,x,0,t)=p(\lambda,-\omega,x,0,t),\quad p(\lambda,\omega,x,1,t)=p(\lambda,-\omega,x,1,t). \tag{3.10}$$

3.2.2 RFM non-uniqueness

In his seminal paper introducing the WMC, Thomson (1987) showed that, while the WMC leads to a unique RFM in one-dimension, in two or more dimensions the RFM is not unique. This means that two distinct RFMs could satisfy the WMC for the same flow but exhibit significantly different dispersion behaviours. Specific solutions illustrating this non-uniqueness for Gaussian inhomogeneous turbulence were first given by Sawford and Guest (1988).

Borgas et al. (1997) explored the non-uniqueness problem in a 3-D model appropriate to homogeneous axisymmetric Gaussian turbulence without reflectional symmetry, which was found to lead to significant reduction of dispersion and spiralling of particle trajectories about the axis of symmetry. Subsequent researchers introduced more general and tractable measures to quantify the rotation of trajectories, for e.g. Wilson and Flesch (1997) considered the mean rate of rotation of

velocity fluctuation vector in two dimensions and Sawford (1999) presented the cross product of particle velocity and acceleration which is related to the area swept out by the velocity vector. For example, the model (3.5) can be replaced by

$$\begin{aligned}
\mathrm{d}\Lambda &= \left(-\frac{\Lambda}{\tau_u} + \frac{\Omega}{\tau_r}\right)\mathrm{d}t + \left(\frac{2}{\tau_u}\right)^{1/2}\mathrm{d}B_u, \\
\mathrm{d}\Omega &= \left(-\frac{\Omega}{\tau_w} + \frac{\Lambda}{\tau_r} + \frac{\mathrm{d}\sigma_w}{\mathrm{d}z}\right)\mathrm{d}t + \left(\frac{2}{\tau_w}\right)^{1/2}\mathrm{d}B_w, \\
\mathrm{d}X &= (u + \Lambda\,\sigma_u)\;\mathrm{d}t, \\
\mathrm{d}Z &= \Omega\,\sigma_w\,\mathrm{d}t.
\end{aligned} \tag{3.11}$$

Here the rotation time-scale τ_r controls the 'spin rate' of particles with respect to an axis in the y-direction (i.e. perpendicular to the (x, z) plane). Note that both positive and negative values of τ_r are permissible.

The RFM (3.11) which is discussed more in detail in the paper to be submitted based on this chapter, also has the invariant measure (3.8) and therefore cannot be objectively distinguished from (3.5). We have chosen to investigate the RFM (3.5) in this thesis as it arguably the simplest 2-D model that is consistent with the turbulent ABL dispersion problem.

3.2.3 The random displacement model and its large-deviation behaviour

As reviewed earlier in the thesis (§1.3.3), the simpler RDM is well-known as the diffusion limit or an approximation of the RFM, in the distinguished limit of short decorrelation time $\tau_i \to 0$, and large velocity fluctuations $\sigma_i \to \infty$, in which $\kappa_i = \sigma_i^2\tau_i$ (here $i = u, w$) is finite and non-zero. The SDE system (3.5) can be

transformed into

$$\begin{aligned} \mathrm{d}X &= u\,\mathrm{d}t + (2\kappa_u)^{1/2}\,\mathrm{d}B_u \\ \mathrm{d}Z &= \kappa_w'\,\mathrm{d}t + (2\kappa_w)^{1/2}\,\mathrm{d}B_w, \end{aligned} \tag{3.12}$$

where $\kappa_w' \equiv \mathrm{d}\kappa_w/\mathrm{d}z$. The corresponding FPE of RDM equation (3.12) is simply the advection-diffusion PDE

$$c_t + u\,c_x = \kappa_u c_{xx} + \left(\kappa_w\,c_z\right)_z, \tag{3.13}$$

where we have identified the joint pdf of (X, Z) in (3.12) with the particle concentration $c(x, z, t)$. The effective diffusivity result (3.1) can be obtained from (3.13) by finding the equations for moments of c (Aris, 1956; Saffman, 1962), or by applying the method of homogenisation (Majda and Kramer, 1999; Pavliotis and Stuart, 2008).

The effective diffusivity does not, of course, give the full picture of the long-time dispersion of tracer particles according to (3.12). In certain problems, for example the point release of a highly toxic substance, the quantity of interest can be the time taken for the tracer concentration to first reach a given (low) threshold at a particular location. The evolution of the relatively low concentrations in the tails of the spreading cloud of particles are described mathematically by large deviation theory. Recently, Haynes and Vanneste (2014) considered the large deviation statistics for (3.13), focussing on classic Taylor-Aris dispersion problems (Couette flow, plane Poiseuille flow and pipe Poiseuille flow). The main point is that, while in the central region (where $x^2/t \sim O(1)$) the evolution of $[c]$ is well-described by the effective diffusivity model (3.1), in the tails of the distribution (where $x/t \sim O(1)$) the concentration $c(x, z, t)$ can be shown, using for example a WKBJ expansion

(Haynes and Vanneste, 2014), to satisfy

$$c(x,z,t) \sim t^{-1/2}\phi(z,\xi)\,\mathrm{e}^{-tg(\xi)}, \quad \text{where} \quad \xi = x/t. \tag{3.14}$$

Equation (3.14) has the characteristic large-deviation decay rate, which is controlled primarily by the so-called rate function $g(\xi)$. If the effective diffusivity model were valid everywhere, we would have $g_0(\xi) = \xi^2/4\kappa_{\mathrm{eff}}$. However, Haynes and Vanneste (2014) showed that in a range of simple shear flows, at larger values of ξ, $g(\xi)$ is in fact larger than its quadratic approximation $g_0(\xi)$, indicating that the tracer decays significantly more in the tail regions than predicted by the effective diffusivity model. In particular, when ξ takes values outside of the range of velocities of the shear flow $(U_{\min}, U_{\max})$, $g(\xi)$ increases sharply and tracer concentrations fall away rapidly outside the interval $U_{\min}t < x < U_{\max}t$.

The function ϕ in (3.14) determines the vertical structure of the local concentration profile, as experienced by an observer travelling at constant speed $\xi = x/t$. $\phi(z,\xi)$ can be obtained by solving the eigenvalue problem

$$\left(u\,q + \kappa_u\,q^2\right)\phi + \kappa_w'\,\phi_z + \kappa_w\,\phi_{zz} = f(q)\,\phi. \tag{3.15}$$

Notice that at small values of q, which correspond to the central region, the eigenvalue $f(q)$ is small and $\phi \approx$ const., consistent with the standard Taylor dispersion analysis.

3.3 Large deviation behaviour in the RFM

The above discussion raises the question of whether the above picture changes when the turbulent dispersion model (3.5) is used in place of the advection-diffusion model (3.12). To answer this question, we have used a WKBJ approach to calculate the rate function for (3.7) numerically, and compare with the corresponding results

of Haynes and Vanneste (2014) for (3.13).

To find the leading-order WKBJ solution, we apply and extend the methods presented in the paper of Haynes and Vanneste (2014) to the FPE (3.7) by seeking the ansatz

$$p(x, z, \lambda, \omega, t) \sim t^{-1/2} \phi(z, \lambda, \omega, \xi)\, \mathrm{e}^{-tg(\xi)}, \tag{3.16}$$

where $g(\xi)$ is the rate function (Touchette, 2009) and $\xi = x/t$ as above. Conservation of the total mass – the spatial integral of (3.16) – imposes a positive and convex $g(\xi)$ having a single minimum at zero, i.e.

$$g(0) = 0, \quad g'(0) = 0. \tag{3.17}$$

Substituting (3.16) into the FPE (3.7), and retaining only the leading order terms gives

$$((u + \lambda\sigma_u)\, q)\, \phi - (\omega\sigma_w\phi)_z - (\sigma_w'\phi)_\omega + \tau_u^{-1}\, (\phi_\lambda + \lambda\phi)_\lambda + \tau_w^{-1}\, (\phi_\omega + \omega\phi)_\omega = f(q)\, \phi, \tag{3.18}$$

where $\sigma_w' \equiv \mathrm{d}\sigma_w/\mathrm{d}z$, and

$$q = \partial g/\partial\xi, \qquad f(q) = q\,\xi - g, \tag{3.19}$$

and the function $\phi(z, \lambda, \omega, \xi)$ satisfies boundary conditions with perfect reflection,

$$\begin{aligned} \phi(0, \lambda, \omega, \xi) &= \phi(0, \lambda, -\omega, \xi), \\ \phi(1, \lambda, \omega, \xi) &= \phi(1, \lambda, -\omega, \xi). \end{aligned} \tag{3.20}$$

As in the diffusion equation problem studied by Haynes and Vanneste (2014), equations (3.18)-(3.20) constitute a family of eigenvalue problems for $\phi(z, \lambda, \omega, t)$ parameterised by q with eigenvalue $f(q)$. Using the numerical scheme described in §3.4 below, $f(q)$ is solved (numerically) as the principal eigenvalue, that is, the eigenvalue

with the largest real part. The rate function $g(\xi)$ is then recovered by the Legendre transform relation between convex functions $g(\xi)$ and $f(q)$ from (3.19),

$$f(q) = \sup_{\xi} \left(q\,\xi - g(\xi)\right) \quad \text{and} \quad g(\xi) = \sup_{q} \left(\xi\, q - f(q)\right). \tag{3.21}$$

Notice that the second relation in (3.21) implies a one-to-one map between parameter q and the physical variable $\xi = x/t$ of the form

$$\xi = \mathrm{d}f/\mathrm{d}q.$$

The eigenfunction ϕ of (3.18) associated with $f(q)$ can therefore be equivalently thought of as a function of ξ, as in (3.16), or of q, as in (3.18).

3.3.1 Effective diffusivity in the RFM

The main purpose of this subsection is to investigate the effective horizontal diffusivity for particles released in the RFM in the large-time limit. First of all, the probability density $p(x, z, \lambda, \omega, t)$ in the ansatz (3.16) can be written as a Taylor expansion of the rate function $g(\xi)$ about $\xi = 0$,

$$p(x, z, \lambda, \omega, t) \approx t^{-1/2}\phi(z, \lambda, \omega, \xi) \exp\left(-t\left(g(0) + \xi\, g'(0) + \frac{\xi^2}{2} g''(0)\right)\right). \tag{3.22}$$

Noting that $g(0) = g'(0) = 0$ as justified in (3.17), and that $\xi = x/t$, the large-deviation form above has a simple relationship with the effective diffusivity given by

$$p(x, z, \lambda, \omega, t) \approx t^{-1/2} \exp\left(-\frac{x^2}{2t} g''(0)\right) \approx t^{-1/2} \exp\left(-\frac{x^2}{4\kappa_{\mathrm{eff}}\, t}\right), \tag{3.23}$$

where the second equation is obtained from the quadratic approximation $g_0(\xi)$. As a result we can identify that

$$\kappa_{\mathrm{eff}} = \frac{1}{2\, g''(0)}. \tag{3.24}$$

However in practice, it is more convenient to infer κ_{eff} directly from $f(q)$, without the need to carry out the Legendre transform explicitly to find $g(\xi)$. Due to the Legendre transform definition in (3.21), $f(q)$ at small q is determined by $g(\xi)$ at small ξ, and vice versa. Hence it can be deduced that $f(q)$ also has a single minimum property at zero, i.e. $f(0) = f'(0) = 0$, so we expect that $f(q)$ also be quadratic near $q = 0$. From the first relation of (3.21), $f(q)$ can be approximated by a Taylor expansion in $g(\xi)$ about $q = 0$,

$$f(q) \approx \sup_{\xi} \left(q\,\xi - \frac{\xi^2}{2} g''(0) \right) = \frac{q^2}{2\,g''(0)} + O(q^3), \tag{3.25}$$

which results in the inverse relation $f''(0) = 1/g''(0)$, a standard result for Legendre transform (Touchette, 2009), and therefore we obtain

$$\kappa_{\text{eff}} = \frac{f''(0)}{2}. \tag{3.26}$$

Alternatively, the effective horizontal diffusivity can be calculated directly from an ensemble of solutions X_t of (3.5). In the long time limit $t \gg 1$, if X_t obeys the diffusion law the particle concentration from an initial point source can be described as a fundamental solution or heat kernel,

$$c(x, z, t) \approx \frac{1}{\sqrt{4\pi\kappa_{\text{eff}} t}}\ \exp\left(-\frac{x^2}{4\kappa_{\text{eff}} t} \right),$$

which is essentially a Gaussian distribution. Based from the above, we can identify the variance of the horizontal distribution is $\sigma_x^2 = 2\kappa_{\text{eff}} t$ and the effective diffusivity can be obtained using

$$\kappa_{\text{eff}} = \lim_{t\to\infty} \frac{1}{2t} \left\langle (X_t - \langle X_t \rangle)^2 \right\rangle, \tag{3.27}$$

where $\langle \cdot \rangle$ is the ensemble average.

3.3.2 Analytical solution

In order to calculate κ_{eff} analytically in the RFM, we use the method of homogenisation (Majda and Kramer, 1999; Pavliotis and Stuart, 2008) in which we introduce two parameters. First, $\varepsilon = h/L$ is the ratio of the ABL depth to the horizontal length scale of the cloud particles. Second, $\delta = h\tau/u_*$ is the ratio of a typical Lagrangian decorrelation time τ to the reference timescale h/u_*, introduced earlier as the typical timescale on which vertical homogenisation occurs in the turbulent ABL. Based on the above, we seek solutions of (3.7) of the form $p = p(\bar{x}, z, \lambda, \omega, \bar{t})$ where $\bar{x}$ and $\bar{t}$ are long time and space scales satisfying

$$\bar{x} = \varepsilon x, \quad \bar{t} = \varepsilon^2 t. \tag{3.28}$$

Further, the turbulent statistics σ_i and τ_i are rescaled as follows

$$\sigma_i = \delta^{-1}\Sigma_i, \quad \tau_i = \delta^2 T_i. \tag{3.29}$$

Notice that this scaling preserves the relationship with the diffusivity, since $\sigma_i^2\tau_i = \Sigma_i^2 T_i = \kappa_i$. As explained in the introduction, diffusive behaviour applies to the late-time, large-scale stage of a point release experiment, hence $\varepsilon \ll \delta \ll 1$ appears to be the most interesting tractable regime. The primary expansion to be inserted into (3.7) is therefore

$$p = \sum_{j=0}^{\infty} \varepsilon^j p_j(\bar{x}, z, \lambda, \omega, \bar{t}). \tag{3.30}$$

The perturbative calculation is detailed in Appendix B. There, it is shown that

$$p_0 = P(\bar{x}, \bar{t}) \exp\left(-\tfrac{1}{2}(\lambda^2 + \omega^2)\right),$$

where $P(\bar{x}, \bar{t})$ is the undetermined function of the 'long' space and time variables

$(\bar{x}, \bar{t})$, and

$$p_1 = \sum_{k=0}^{\infty} \mathrm{He}_k(\omega)\Big(C_k(z) + \lambda D_k(z)\Big) P_{\bar{x}}(\bar{x}, \bar{t}) \exp\left(-\tfrac{1}{2}(\lambda^2 + \omega^2)\right).$$

At order ε^2, the following solvability condition is found,

$$\int_{\mathcal{D}} \left(p_{0\bar{t}} + u p_{1\bar{x}} + \delta^{-1}\lambda \Sigma_u p_{1\bar{x}}\right)\, \mathrm{d}z\, \mathrm{d}\lambda\, \mathrm{d}\omega = 0,$$

where the integral is over the domain $\{\mathcal{D} : (\lambda, \omega) \in \mathbb{R}^2, z \in [0, 1]\}$. Evaluating this integral, one obtains the one-dimensional diffusion equation

$$P_{\bar{t}} = \kappa_{\mathrm{eff}} P_{\bar{x}\bar{x}}, \tag{3.31}$$

and the main analytical result for the effective diffusivity is given by

$$\kappa_{\mathrm{eff}} = \left[\frac{F^2}{\kappa_w} + \kappa_w \left(\frac{F}{\sigma_w}\right)'^2 - \frac{\kappa_w}{2}\left(\frac{\kappa_w}{\sigma_w}\left(\frac{F}{\sigma_w}\right)'\right)'^2\right] + \left[\kappa_u + \frac{\kappa_w \tau_u}{\tau_u + \tau_w}\left(\frac{\kappa_u}{\sigma_u}\right)'^2\right], \tag{3.32}$$

where as before, $[\cdot]$ denotes the the vertical average over the boundary layer, and $F(z)$ is the integral of the mean wind profile as in (3.2).

The first average part of (3.32) can be interpreted as an expansion in δ^2, including three terms of $O(1)$, $O(\delta^2)$ and $O(\delta^4)$ respectively, and with terms of $O(\delta^6)$ neglected. The leading term is identical to the first term in Saffman's result (3.2), with the remaining terms giving the corrections due to the finite decorrelation times in the RFM (3.4). It is notable that the dominant correction, given by the second term in (3.32), is always positive. Consequently, at least for small δ, the effective horizontal diffusivity will always be greater in the RFM compared to its RDM limit. The leading correction term in the second part of (3.32) is also positive definite, showing that shear dispersion is always increased in the RFM compared with the RDM.

3.4 Numerical method for the eigenvalue problem

In this section, an efficient algorithm for the solution of the non-dimensonalszed eigenvalue problem (3.18) is presented. Our approach is to seek a Hermite polynomial expansion for $\phi(z,\lambda,\omega)$ (we have suppressed the ξ-dependency in this expression as ξ (through q) has the role of a parameter in the eigenvalue problem),

$$\phi(z,\lambda,\omega) = \frac{1}{2\pi}\sum_{k=0}^{\infty}\sum_{l=0}^{\infty} C_{k,l}(z,\xi)\,\mathrm{He}_k(\omega)\,\mathrm{He}_l(\lambda)\,\mathrm{e}^{-(\lambda^2+\omega^2)/2}. \tag{3.33}$$

where $\mathrm{He}_k(\omega)$ and $\mathrm{He}_l(\lambda)$ are the Hermite polynomials defined by eq. (A.1) in Appendix A. Before inserting the expansion (3.33) into the eigenvalue problem (3.18) it is helpful to rewrite the eigenvalue problem in the form

$$\tau_u^{-1}\,\mathcal{L}_\lambda\phi + \tau_w^{-1}\,\mathcal{L}_\omega\phi - (\omega\sigma_w\phi)_z - (\sigma_w'\phi)_\omega + ((u+\lambda\sigma_u)\,q)\,\phi = f(q)\,\phi, \tag{3.34}$$

where e.g. the linear operators

$$\mathcal{L}_\omega = \partial_\omega^2 + \omega\partial_\omega + 1, \quad \text{and} \quad \mathcal{L}_\lambda = \partial_\lambda^2 + \lambda\partial_\lambda + 1.$$

Using the Hermite polynomial identities given in Appendix A, the resulting expression can be rearranged into a single summation of the form (3.33). Using the orthogonality, the system can then be reduced to a doubly-infinite set of coupled ordinary differential equations for the $\{C_{k,l}\}$,

$$\begin{aligned} u\,q\,C_{k,l} + \sigma_u\,q\,(C_{k,l-1} + (l+1)\,C_{k,l+1}) - \sigma_w\,\partial_z C_{k-1,l} \\ - (k+1)\,\partial_z\,(\sigma_w\,C_{k+1,l}) - \left(k\,\tau_w^{-1} + l\,\tau_u^{-1}\right) C_{k,l} = f(q)\,C_{k,l}, \end{aligned} \tag{3.35}$$

where $k, l \geq 0$, and the convention $C_{k,-1} \equiv 0$ and $C_{-1,l} \equiv 0$ is used. The system (3.35) can be truncated at a finite $(k, l) = (K, L)$, and discretised using N_z points in z, resulting in a matrix eigenvalue problem of dimension $N_z KL \times N_z KL$, whose numerical implementations are detailed below.

3.4.1 Boundary conditions and implementation

The boundary conditions can be obtained using the the symmetry $\mathrm{He}_k(\omega) = (-1)^k \mathrm{He}_k(-\omega)$. Substituting the expansion (3.33) into the boundary conditions (3.20), at $z = 0, 1$, can be shown to be

$$C_{k,l}(0, \xi) = C_{k,l}(1, \xi) = 0, \quad \text{for } \ k \text{ odd.} \tag{3.36}$$

This means that the k-even equations have no boundary conditions and k-odd take two boundary conditions, which will add up to the correct number of boundary conditions provided that the series is truncated at $k = K$ odd.

The solution to system (3.35) involves solving the eigenvalue problem type

$$\mathbf{A}\,\boldsymbol{c} = f(q)\,\boldsymbol{c}, \tag{3.37}$$

where $\mathbf{A}$ is a square matrix of dimension $N_z KL \times N_z KL$. A standard finite-difference discretisation is used, with N_z equally spaced grid-points with $\Delta z = 1/N_z$, on a staggered cell-centred grid (i.e. $z_i = (1-1/2)\Delta z$, for $i = 1, \ldots, N_z$) in order to apply the boundary conditions (3.36) at $z = 0, 1$ systematically. In this discretisation, $\boldsymbol{c}$ are eigenvectors of length $N_z KL$ with entries corresponding to $C_{k,l}(z_i)$.

There are two MATLAB built-in eigenvalue/vector solvers available namely `'eig'` (Anderson et al., 1999) and `'eigs'` (Lehoucq et al., 1998). Both routines are based on the QR-algorithm, a numerical eigenvalue algorithm that performs the QR-decomposition of a matrix into an orthogonal matrix and an upper triangular

matrix. The first routine `'eig'` is suited to generalised problems with matrices of realistic sizes that fit well into memory, but not to large non-symmetric sparse matrices. On the other hand, the `'eigs'` routine uses specialised methods that are more appropriate for large problems where only a limited subset of the eigenvalues/vectors are required. Therefore the principal eigenvalue $f(q)$ for a given value of q and eigenvectors $\boldsymbol{c}$ solutions of eigenvalue problem (3.37) are suitably calculated using the MATLAB command:

```
[c,f] = eigs(A,1,'lr').
```

However it can become computationally expensive to calculate sensible values of $f(q)$ of large matrices of $N_zKL \times N_zKL$ elements. Accurate computations of $f(q)$ are expected to rely on a large selection of numerical parameters such as a sufficiently large number of grid-points N_z, truncations K and L, and a suitable tolerance for eigenvalue convergence at certain values of q. There are several ways to optimise the MATLAB routine. One method that has been used successfully is a multi-grid method, in which low resolution (in N_z) solutions are interpolated to provide initial guesses for higher resolution calculations.

Table 3.1 shows the convergence of eigenvalue solutions $f(q)$ of (3.35) as the N_z resolution increases, for all the test-cases detailed in Table 3.2. Based on the calculations, the $f(q)$ values start to converge to 2 significant figures with $N_z \geq 64$. Not shown in the table, we also found that increasing the truncation values above $K \geq 3$ and $L \geq 2$ do not make any difference in the calculated $f(q)$. The following Figure 3.4 shows the resulting $\phi(z)$ plots in each case at resolutions $N_z = 64,\ 128$ where the eigenvalue solutions are correctly converged.

Another technique that has been exploited is the method of continuation, where the solution from the previous q calculation is used as an initial guess of the next q calculation, provided that parameter interval Δq is sufficiently small.

	N_z	$q = 0.2$	$q = 2$
Constant	8	0.0919	3.455
	16	0.0898	3.406
	32	0.0893	3.395
	64	0.0892	3.392
	128	0.0892	3.391
Stable ABL	8	0.208	4.126
	16	0.200	4.106
	32	0.198	4.054
	64	0.197	4.034
	128	0.197	4.030
Neutral ABL	8	0.345	4.294
	16	0.333	4.397
	32	0.331	4.353
	64	0.330	4.342
	128	0.330	4.340

Table 3.1: Table of numerical eigenvalue results $f(q)$ using (3.35) for $q = 0.2$ near the central region and $q = 2$ farther out. Results are listed for (i) constant, (ii) stable ABL, and (iii) neutral ABL cases detailed in Table 3.2.

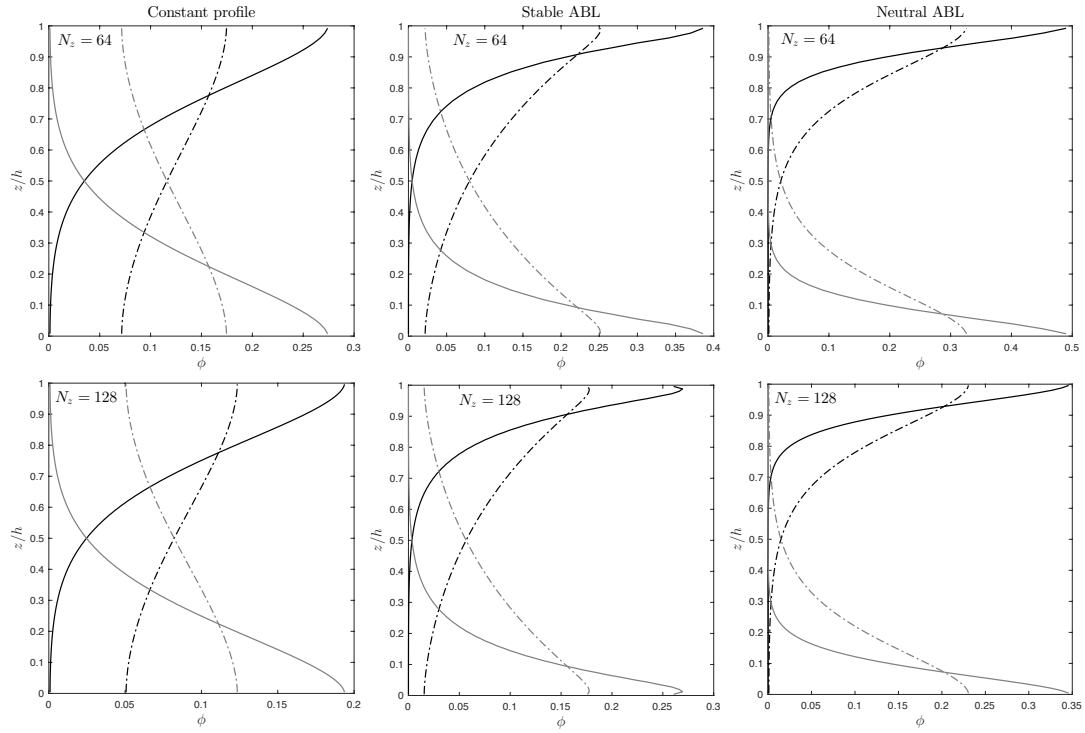

Figure 3.4: Eigenfunctions ϕ as a function of ABL height z/h for $q = 0.2,\ 2$ (dashed and solid black lines) and for $q = -0.2,\ -2$ (dashed and solid grey lines), using resolutions $N_z = 64, 128$ and truncated at $K = 5, L = 4$.

3.4.2 Turbulent statistics

In the results to follow, we apply our ideas to three test-case problems; namely the constant case, the stable ABL and the neutral ABL, as detailed in Table 3.2 below. The first case has idealized constant profiles for $\sigma(z)$ and $\tau(z)$, and used to demonstrate the numerical solutions of the eigenvalue problem introduced above. The last two ABL profiles are empirical fits to observed statistics (Hanna, 1982; Stohl et al., 2005) for the stable and neutral conditions in the ABL, respectively (see §1.1.1 for details). As practiced earlier in Chapter 2, for the purpose of numerical stability, we modify slightly the profiles of Hanna (1982) to $\sigma_i(Z_m(z))$ and $\tau_i(Z_m(z))$, where $Z_m(z) = z_b + z(1 - 2z_b)$ and $z_b = 0.05$ are chosen. The non-dimensional parameter $\epsilon = u_*/fh$ in the neutral ABL profile is a boundary layer Rossby number.

Condition	Hanna (1982) profile	Modified profile
Constant	$\sigma_u = \sigma_w = 1$ $\tau_u = \tau_w = 0.1$	–
Stable	$\sigma_u = 2.0\,(1 - z)$ $\sigma_w = 1.3\,(1 - z)$ $\tau_u = 0.15\,z^{1/2}/\sigma_u$ $\tau_w = 0.1\,z^{4/5}/\sigma_w$	$\bar{\sigma}(z) = \sigma(Z_m(z))$ $\bar{\tau}(z) = \tau(Z_m(z))$
Neutral	$\sigma_u = 2.0\exp(-2z/\epsilon)$ $\sigma_w = 1.3\exp(-2z/\epsilon)$ $\tau_u = \tau_w$ $\tau_w = \dfrac{z}{2\sigma_w(1 + 15z/\epsilon)}$	$\bar{\sigma}(z) = \sigma(Z_m(z))$ $\bar{\tau}(z) = \tau(Z_m(z))$

Table 3.2: The non-dimensional profiles of the velocity standard deviation $\sigma(z)$ and Lagrangian decorrelation time-scale $\tau(z)$ suitable for (i) a constant profile, (ii) a stable ABL, and (iii) a neutral ABL (e.g. Hanna, 1982).

3.5 Numerical results

In this section, the large deviation results (3.18) for the RFM are discussed. Our main numerical results include effective horizontal diffusivity $\kappa_{\text{eff}}(\delta)$ and the rate function $g(\xi)$. To understand more completely how the RFM and RDM differ, we reintroduce parameter δ from (3.29) as an 'interpolation' parameter for the input turbulence profiles as follows:

$$\sigma_i = \delta^{-1}\,\Sigma_i \quad \text{and} \quad \tau_i = \delta^2\,T_i, \quad (i = u, w), \tag{3.38}$$

where Σ_i and T_i are the turbulent velocity fluctuations and decorrelation time profiles, respectively from the test-cases detailed in Table 3.2. The new profiles σ_i and τ_i in (3.38) generate a family of interpolated models, with δ as a free parameter.

Here the limit $\delta \to 0$ corresponds to the RDM (3.12), and $\delta = 1$ gives the RFM (3.5) with velocity decorrelation times appropriate to the ABL. Models with δ in the range $0 < \delta < 1$ are more 'diffusive' and than the ABL, and those with $\delta > 1$ are more 'ballistic' in the sense discussed in §1.3.2.1.

3.5.1 RFM-RDM hybrid model

The aim of this subsection is to validate our numerical approach of using the Hermite polynomial expansion method to solve the eigenvalue problem and subsequently aid in the development of numerical strategies required to calculate the large eigenvalue problem in (3.18). In this process, we found it helpful to first consider a simpler model with only three stochastic variables, which will involve less expensive computations of the associated eigenvalue problem.

Motivated by the physical intuition that suggests that finite decorrelation times are likely to be more important in the vertical than in the horizontal, we consider

the 'RFM-RDM hybrid model',

$$\begin{aligned} \mathrm{d}\Omega &= \left(-\frac{\Omega}{\tau_w} + \frac{\mathrm{d}\sigma_w}{\mathrm{d}z}\right)\mathrm{d}t + \left(\frac{2}{\tau_w}\right)^{1/2}\mathrm{d}B_w, \\ \mathrm{d}X &= u\,\mathrm{d}t + (2\,\kappa_u)^{1/2}\,\mathrm{d}B_u, \\ \mathrm{d}Z &= \Omega_t\,\sigma_w\,\mathrm{d}t, \end{aligned} \tag{3.39}$$

which is obtained by taking the diffusive limit in the x-direction only (i.e. $\tau_u \to 0,\ \sigma_u \to \infty,\ \sigma_u^2\tau_u = \kappa_u$), where $\kappa_u(z)$ is the horizontal diffusivity term. The large-deviation results will therefore be based on the corresponding FPE for joint probability density $p(\omega, x, z, t)$,

$$p_t + (u\,p)_x - (\kappa_u\,p)_{xx} = \tau_w^{-1}\,(p_\omega + \omega p)_\omega - (\sigma_w'\,p)_\omega - (\omega\,\sigma_w\,p)_z\,, \tag{3.40}$$

with boundary conditions at $z = 0, 1$,

$$p(\omega, x, 0, t) = p(-\omega, x, 0, t) \ \text{ and } \ p(\omega, x, 1, t) = p(-\omega, x, 1, t).$$

Based on our analysis for large deviation approximation above, the eigenvalue problem for $\phi(\omega, z, \xi)$ from (3.40) can be reduced to a relatively simpler system of eigenvalue problems,

$$\left(u\,q + \kappa_u\,q^2 - \frac{k}{\tau_w}\right)C_k - \sigma_w\partial_z C_{k-1} - (k+1)\partial_z\,(\sigma_w C_{k+1}) = f(q)\,C_k, \tag{3.41}$$

for $k \geq 0$, with boundary conditions $C_k(0, \xi) = C_k(1, \xi) = 0$, for k odd. If the system (3.41) is truncated at $k = K$ (odd), the linear operator on the left-hand side can be discretised into a matrix of dimensions $N_z(K+1) \times N_z(K+1)$ including the $k = 0$ equation of (3.41). Based on our tests in Table 3.1, correct convergence of $f(q)$ solutions using (3.41) can be obtained using lower resolutions (specifically $N_z = 30$ and $K = 3$) than those obtained using (3.35), hence accurate results are

computed directly without the use of optimisation strategies such as the multi-grid method or continuation method described above.

In the large deviation results below, the RFM-RDM hybrid model (3.39) for the constant and (modified) stable cases are examined. The main results are shown in the top row panels of Figure 3.5 where the effective horizontal diffusivity κ_{eff} are plotted as a function of the interpolation parameter δ (recall that $\delta \to 0$ corresponds to the RDM, $\delta = 1$ gives the RFM with the ABL profiles detailed in Table 3.2, and other values of δ interpolate between the two models). The blue curve indicates κ_{eff} obtained from the calculated $f(q)$ in the eigenvalue problem (3.41) using the formula (3.26), which is explicitly written as

$$\kappa_{\text{eff}} = \lim_{\Delta q \to 0} \frac{f(\Delta q)}{(\Delta q)^2}. \tag{3.42}$$

Numerical κ_{eff} statistics from SDE ensemble solutions of the hybrid model (3.39) (black diamond symbols) and the RDM (3.12) (solid green squares) are also plotted. The ensemble of LPDM solutions are obtained using the numerical scheme EXPLICIT 2.0 (see Table 2.2 for details) at sufficiently small time-steps Δt as recommended in Chapter 2 of this thesis. Here κ_{eff} is measured by the time derivative of the horizontal displacement variance (3.27) of SDE ensemble size $N = 10^6$ solutions. Late integration times at $t = 15,\ 50$ for the constant and stable ABL profiles, respectively are obtained to ensure that the particle distribution is passed the well-mixed state or homogenisation period. The κ_{eff} results show good agreement between the eigenvalue problem and the SDE ensemble, and hence confirms the validity of our numerical approach for solving the eigenvalue problem detailed in §3.4, at least in the simpler hybrid RFM-RDM model.

To complete this short subsection, we include the large deviation results obtained from the eigenvalue problem (3.41) such as the rate function $g(\xi)$ as a function of the large deviation velocity $\xi = x/t$, shown in the middle row. The rate functions

in blue are numerically obtained by taking the Legendre transform (3.21) of the solution $f(q)$ from eq. (3.41), using the corresponding input parameters at $\delta = 1$. This is compared with $g(\xi)$ solutions calculated similarly for the RDM (3.15) in red dashed curves and the quadratic approximation $g_0(\xi) = \xi^2/4\kappa_{\text{eff}}$ in black dashed curves. The minimum and maximum flow speeds, $U_{\min}$ and $U_{\max}$ are also plotted for reference. The bottom row of Figure 3.5 shows the relationship between ξ and q, of ($\delta = 1$) hybrid model and ($\delta = 0$) RDM, determined from their numerical Legendre transforms.

The result is that for all cases, both the hybrid model and RDM have $g(\xi)$ larger than its quadratic approximation $g_0(\xi)$, as discussed above and shown in the paper of Haynes and Vanneste (2014). The near identical $g(\xi)$ curves obtained suggest that the large-deviation behaviour is extremely similar between the RDM and the hybrid model, at least near the central region. In the subsection below we will discuss the result in more detail and also determine if the same result holds for the full RFM model.

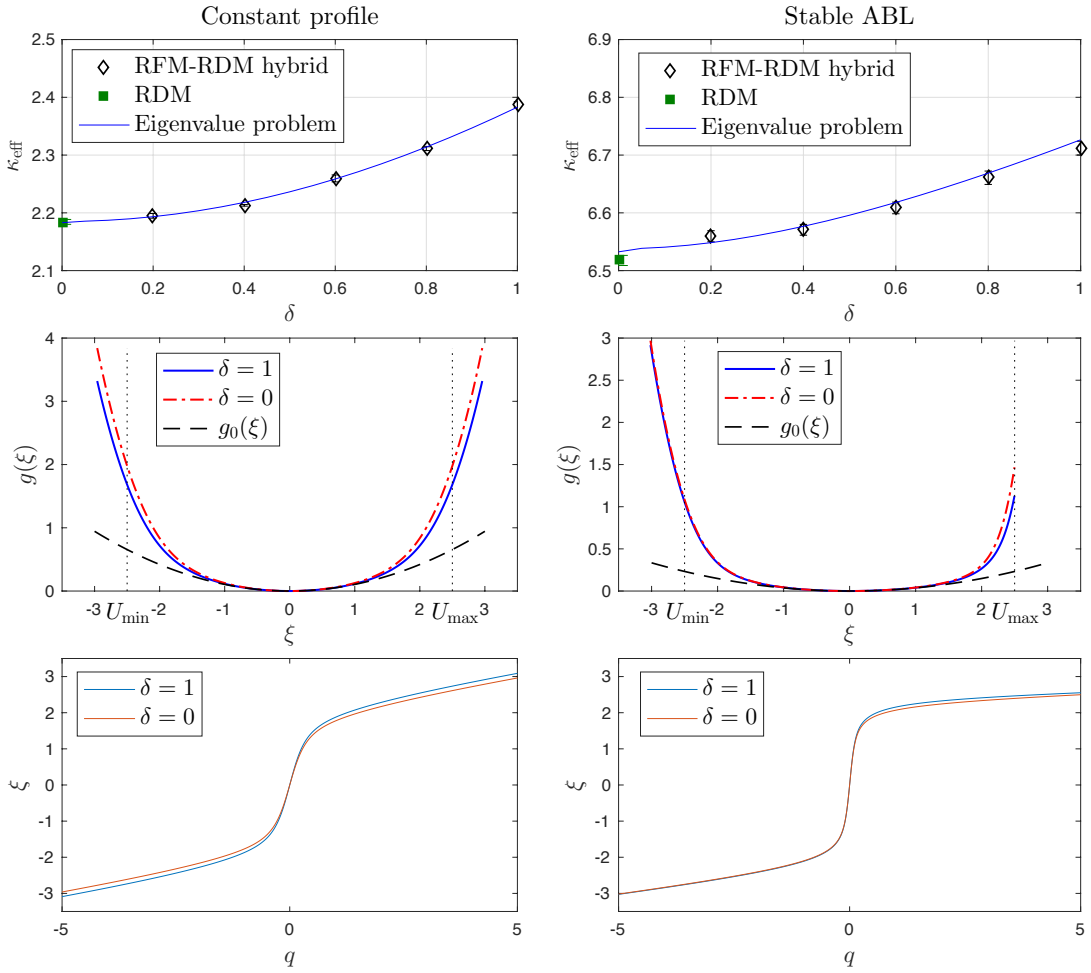

Figure 3.5: Large-deviation results for the RFM-RDM hybrid model (3.39), for test-cases of constant profile (left column) and modified stable ABL profile (right column) from Table 3.2. First row: the effective diffusivity κ_{eff} plotted as a function of the model interpolation parameter δ. Second row: the rate function $g(\xi)$ obtained from the Legendre transform of the numerical eigenvalue $f(q)$. Third row: a map between large-deviation parameter q and velocity $\xi = x/t$ derived from the numerical eigenvalue $f(q)$ solution of (3.41).

3.5.2 Large deviation RFM results

In this subsection, we proceed with the main large deviation results of the RFM (3.5) by extending the numerical scheme used in the calculations for the hybrid RFM-RDM model. The following numerical adaptations to the solver are required:

1. The left-hand side of (3.18) is discretised into a matrix of dimensions $N_z(K+1)(L+1) \times N_z(K+1)(L+1)$, including the $k=0$ and $l=0$ equations. Here we have chosen the parameters $N_z = 100, K = 7$ and $L = 5$.

2. Effective diffusivity κ_{eff} is calculated from (3.42) using a finite value of Δq in practice. This value must be chosen carefully, because truncation errors from the eigenvalue solver give inaccurate numerical results at very low Δq. We found that $\Delta q = 10^{-2},\ 10^{-3},\ 10^{-4}$ are adequate for the constant, stable ABL and neutral ABL cases, respectively.

3. To compute the eigenvalue problem efficiently, low resolution solutions of $N_z = 20$ or 40 are used to interpolate initial eigenvector $\{C_{k,l}\}$ guesses for the higher resolution ($N_z = 100$) calculations.

For the SDE ensemble solution calculated from the LPDMs, the final integration times to capture the large deviation behaviour vary in each test-case, and explicitly we have used $t = 15,\ 50,\ 200$, for the constant (idealised), stable ABL and neutral ABL cases, respectively (see Table 3.2).

First of all, we show the numerical results obtained from the eigenvalue problem (3.18) in Figure 3.6 for the three test cases examined. The results include the eigenvalue function $f(q)$ in the top row and the rate function $g(\xi)$ calculation in the middle row. For the constant profile in the leftmost column, the RDM result ($\delta = 0$, red dashed curves) is seen to underestimate the horizontal diffusion rate of the RFM ($\delta = 1$, solid blue curves), leading to an underestimate of $f(q)$ and an overestimate of $g(\xi)$, near the outers regions (i.e. $\xi \to U_{\min}, U_{\max}$). The concentration distributions

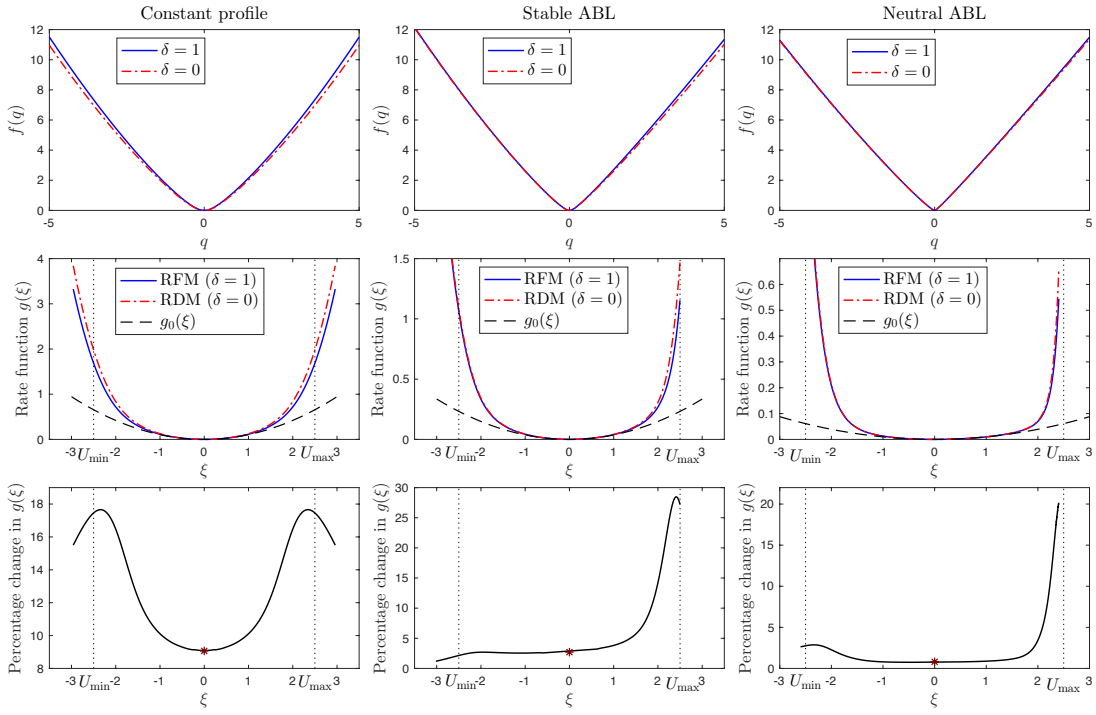

Figure 3.6: Large-deviation results for the constant profile, (modified) stable ABL and (modified) neutral ABL cases (see Table 3.2 for details) in the RFM. First row: the eigenvalue $f(q)$ obtained by numerical solution of the eigenvalue problem (3.18) (solid blue line) is compared with the RDM eigenvalue problem (3.15) (red dashed line). Second row: the rate function $g(\xi)$ obtained by Legendre transform of the eigenvalue problem (3.18) solution $f(q)$ (solid blue curves) is compared with those of the RDM (3.15) (red dashed curves). Their corresponding quadratic approximations $g_0(\xi)$ are also plotted (black dashed curves). Third row: percentage difference between $g(\xi)$ in the RFM compared to the RDM (calculated as 100(RDM-RFM)/RFM).

for neutral ABL case (rightmost column) are slightly skewed, with $g(\xi)$ increasing faster for $\xi < 0$ compared to $\xi > 0$. This corresponds to smaller concentrations predicted near the ground where the velocity ξ is large and negative, compared to the upper domain towards the ABL top where ξ is large and positive.

The $f(q)$ results for the RDM ($\delta = 0$) are seen to be remarkably identical for all q in the stable and neutral ABL cases. However, close inspection shows in fact that there is a range of values of $\xi > 0$, for which the diffusive behaviour overestimates the $g(\xi)$ in the stable and neutral ABL cases. This can be observed clearly in the bottom row of Figure 3.6, which displays the plotted $g(\xi)$ percentage difference between the RFM ($\delta = 1$) and RDM ($\delta = 0$) for all profiles and also shows that the small differences found in κ_{eff} (dark red star symbols) are not typical of the differences in $g(\xi)$ everywhere. In fact, both the stable and neutral ABL profiles have $g(\xi)$ significantly larger ($\geq 20\%$) for the RDM, towards $\xi = U_{\max}$. This highlights the fact that the outcome of using realistic Lagrangian decorrelation times in the RFM is to enhance transport into the tail regions, with the largest effect being in the downstream tail.

Finally in Figure 3.7, the effective horizontal diffusivity κ_{eff} of the interpolated models (3.38) is plotted as a function of interpolation parameter δ. The $\kappa_{\text{eff}}(\delta)$ provides a quantitative interpolation between the RDM ($\delta = 0$) and the RFM with the ABL profiles detailed in Table 3.2 ($\delta = 1$) in the large deviation regime. Here the numerical κ_{eff} obtained from the eigenvalue solutions $f(q)$ from the eigenvalue problem (3.35) using the formula (3.26) (blue solid lines) is compared with the SDE ensemble solution statistics (red diamond symbols) using the formula (3.27). The asymptotic solutions of κ_{eff} (3.32) (black dotted lines) are also plotted here, which shows excellent agreement with the eigenvalue calculations and the SDE ensemble statistics, at least in the interpolation between the RDM and RFM ($0 < \delta < 1$). The difference in κ_{eff} between the physical RFMs ($\delta = 1$) and their RDM limit ($\delta = 0$) is rather small, in fact just 9.08%, 2.74% and 0.76% for the constant, stable

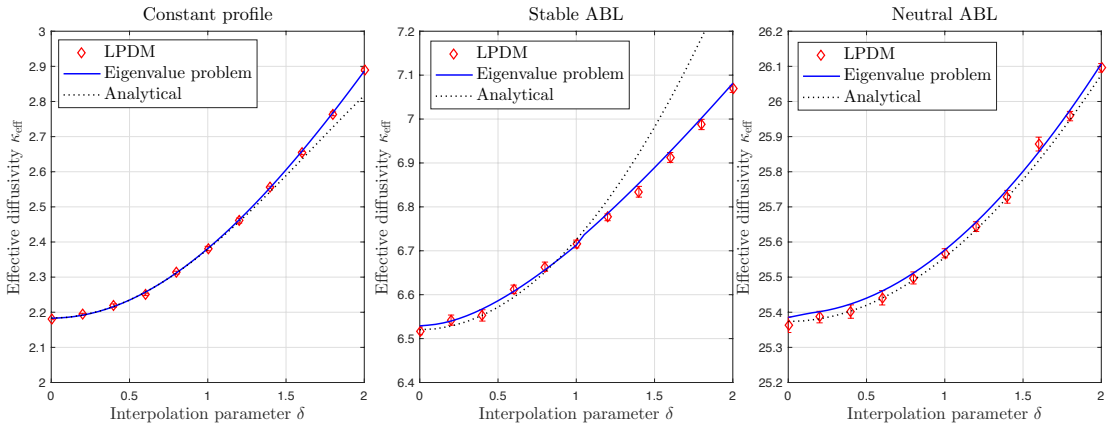

Figure 3.7: The effective horizontal diffusivity κ_{eff} as a function of interpolation parameter δ obtained from the numerical solutions of the eigenvalue problems (3.15) and (3.18) (solid blue curve), compared with the SDE ensemble statistics of (3.5) and (3.12) (red diamond symbols). Analytical results (3.32) are also shown (black dotted line).

and neutral profiles. The κ_{eff} values for the range $1 < \delta < 2$ are also plotted to show the interpolation between the RFM and the more 'ballistic' models in the sense discussed in §1.3.2.1.

3.6 Rare-event simulation

In order see if the large-deviation results obtained above are accurate, we shall consider a scenario where we want to make a measurement of particle concentration in a specific region at a late time after the particle release. If the region in question is outside of the central region illustrated in Figure 3.2, the problem is one of rare-event simulation introduced in §1.4. Here the direct Monte-Carlo (DMC) sampling using the RFM does not provide a reliable estimate of the concentration quantity as the concentrations are controlled by rare realisations which are not sampled satisfactorily.

To remedy this, a splitting technique can be used to improve the computational

efficiency of the calculations. For the purposes of this work, we have implemented a version of Grassberger's (2002) go-with-the-winners (GWTW) branching process introduced in §1.4.2. The challenge in any implementation of GWTW is to find an appropriate method of assigning scores S_t to trajectories, so that the 'winners' correspond to trajectories likely to end up in the region of interest, and 'losers' are those that will not. As discussed in §1.4.2, Esler (2015) showed that the ideal scoring system is based on the (unknown) adjoint problem solution. Based on this insight, we can use the predictions of large-deviation theory for the shear dispersion problem to approximate the adjoint solution, and use the approximation to drive the GWTW algorithm here. In doing so, we improve significantly on GWTW calculations reported in Haynes and Vanneste (2014, Appendix B.1).

Suppose we are interested in the particle concentration reaching the infinite region $R = \{X \geq X_0, Z \in [0,1]\}$ at a late time $t = T$, the corresponding value of the velocity 'ray' is $\xi_0 = X_0/T$. The following expansion of the particle concentration $c(x, z, \lambda, \omega, t)$ can be obtained by Taylor expanding the large deviation form (3.16) about $|\xi - \xi_0| \ll 1$,

$$c(x, z, \lambda, \omega, t) \approx t^{-1/2} \left(\phi(z, \lambda, \omega, \xi_0) + \ldots\right) \, \mathrm{e}^{-t(g(\xi_0) + g'(\xi_0)\xi + \ldots)} \propto \mathrm{e}^{-q\,x}, \tag{3.43}$$

where $q = g'(\xi_0)$ is the corresponding large deviation parameter for ξ_0. The adjoint of (3.7) (sometimes known as the 'retro-transport' equation, see for e.g. Hourdin and Talagrand (2006)), $c^*(x, z, \lambda, \omega, t)$ can be physically interpreted as a measure of the proportion of a fluid parcel at (x, z) with scaled velocity (λ, ω) that will subsequently arrive in the (suitably-weighted) receptor region R (in the stochastic representation this can be interpreted as a probability). In the current problem, it can be shown that the adjoint PDE is simply the forward PDE (3.7) with the velocity field reversed (see Flesch et al., 1995, for example). Hence by symmetry,

the adjoint problem will have

$$c^*(x, z, \lambda, \omega, t) \propto \mathrm{e}^{q(x-X_0)},$$

which adapting the scoring algorithm from Esler (2015), suggests the GWTW scoring:

$$S_t = \Theta_t \; c^*(x, z, \lambda, \omega, t) = \Theta_t \; \exp(q \, X_t). \tag{3.44}$$

In the following results, we have compared the DMC (3.5) with the GWTW importance sampling technique using the scoring strategy (3.44). The calculations are all for the stable ABL (see Table 3.2 for details), with parameters given in Figure 3.6 at time $T = 20$. Several GWTW calculations are performed with the scoring parameter q in (3.44) being varied ($q = 0.5,\ 1.0,\ 1.5$). We know from the discussion above that each value of q is related to a particular 'speed' $\xi = x/t$ through the Legendre transform relationship. Consequently we expect the trajectories in each GWTW calculation to be centred on location moving with speed $\xi_0 = 1.94,\ 2.15,\ 2.25$, respectively. Figure 3.8 shows that this is in fact the case.

Table 3.3 lists the statistical mean estimates of the particles reaching the region $R = \{X \geq \xi_0 T,\ Z \in [0, 1]\}$, $\{\boldsymbol{X}_i\}$ sampled by the DMC and $\{\tilde{\boldsymbol{X}}_i\}$ by GWTW branching process at time $T = 20$. The computational saving due to using GWTW is given in column 3, and is calculated as the ratio of the variance of the two methods:

$$\mathrm{Var}(I_R(X \geq \xi_0 T))/\mathrm{Var}(\Theta_T \, I_R(\tilde{X} \geq \xi_0 T)),$$

where I_R is the indicator function defined as

$$I_R(\boldsymbol{X}_t) = \begin{cases} 1 & \boldsymbol{X}_t^{(i)} \in R, \\ 0 & \text{otherwise.} \end{cases}$$

The saving factor is seen to improve as q increases, provided that some DMC tra-

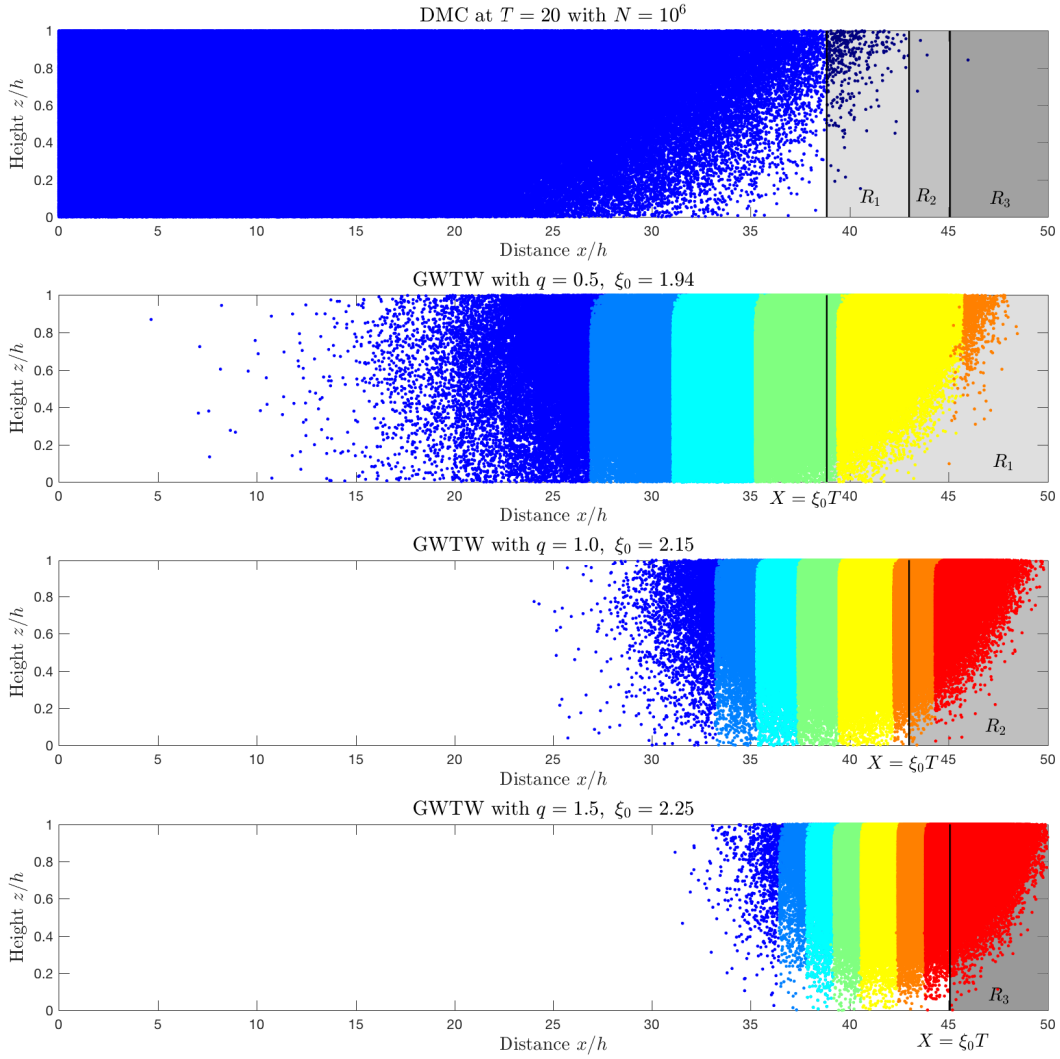

Figure 3.8: Particle positions at $T = 20$, using the DMC (3.5) (first panel), compared with those of GWTW branching process for $q = 0.5$ (second panel), $q = 1.0$ (third panel), and $q = 1.5$ (fourth panel). The blue particles indicate trajectories having $\Theta_T \geq 1$, yellow $10^{-3} > \Theta_T > 10^{-4}$, orange $10^{-4} > \Theta_T > 10^{-5}$ and red $\Theta_T < 10^{-5}$.

jectories still reach the receptor region R.

q	DMC	GWTW	Saving factor
0.1	$(7.603 \pm 0.0254) \times 10^{-2}$	$(7.601 \pm 0.098) \times 10^{-2}$	7
0.2	$(1.257 \pm 0.0129) \times 10^{-2}$	$(1.251 \pm 0.019) \times 10^{-2}$	46
0.3	$(3.156 \pm 0.079) \times 10^{-3}$	$(3.106 \pm 0.002) \times 10^{-3}$	999
0.4	$(9.780 \pm 0.276) \times 10^{-4}$	$(9.934 \pm 0.020) \times 10^{-4}$	185
0.5	$(3.560 \pm 0.225) \times 10^{-4}$	$(3.613 \pm 0.009) \times 10^{-4}$	664
0.6	$(1.410 \pm 0.216) \times 10^{-4}$	$(1.470 \pm 0.002) \times 10^{-4}$	7789
0.7	$(6.500 \pm 1.107) \times 10^{-5}$	$(6.229 \pm 0.010) \times 10^{-5}$	12545
0.8	$(2.900 \pm 0.430) \times 10^{-5}$	$(2.806 \pm 0.006) \times 10^{-5}$	5900
0.9	$(1.200 \pm 0.339) \times 10^{-5}$	$(1.313 \pm 0.004) \times 10^{-5}$	6190
1.0	$(4.000 \pm 1.871) \times 10^{-6}$	$(6.396 \pm 0.007) \times 10^{-6}$	68838

Table 3.3: Table of results of mean estimate for DMC (3.5) $\langle I_R(X \geq \xi_0 T)\rangle$ (here I_R is the indicator function), against the estimate $\langle \Theta_T\, I_R(\tilde{X} \geq \xi_0 T)\rangle$ of the GWTW trajectories, using the q-parameter scoring (3.44). The ensemble solutions are calculated in the stable ABL case is used here at time $T = 20$ with $N = 10^6$.

3.7 Conclusions

In this chapter, the long-time dispersion behaviour of LPDMs are discussed in the context of two-dimensional shear dispersion in the ABL. The key results obtained from our analysis are summarised in the following.

1. The effective diffusivity κ_{eff} governing the horizontal spread of particles in the ABL, is found to differ by only a few percent between the use of RFM

(3.5) and its RDM approximation (3.12). The RFM effective diffusivity is invariably slightly larger, as illustrated by our analytical, semi-analytical and numerical results in Figure 3.7, for all the test cases examined. From the analytical expression for the κ_{eff} in the RFM found in (3.32), the dominant term is dominated by the integral of F^2/κ_w just as predicted in Saffman's (1962) analysis for the RDM.

2. The second key result is the large deviation rate function ($g(\xi)$ above) which controls the evolution of the tracer concentration in the tail regions of the cloud of particles. In the test-cases that are relevant in the stable and neutral ABL conditions, the large deviation rate functions between the RFM and RDM are found to be quite identical except in the positive tail regions where the RFM exhibits increased transport (reduced rate function $g(\xi)$) compared to the RDM (see Figure 3.6). This means that the large deviation rate function becomes more sensitive to the use of RDM approximation in the positive tail region.

Overall, our results show that the RDM (3.12) shows an excellent job of modelling late-time shear dispersion in the turbulent boundary layer, because the effective diffusivity and large-deviation statistics of the RDM are so close to those of the more realistic RFM (3.5), at least under typical stable and neutral ABL conditions. The analytical κ_{eff} equation (3.32) could even be used as the basis for correcting the diffusivities in the RDM to agree with the RFM more closely. The results found in this chapter lend further support to the results found in Chapter 2, which suggests that the cheaper and more easily implemented RDM can be used without significant loss of accuracy in one-dimensional problems.

Chapter 4

Kernel density methods

4.1 Introduction

In this chapter we are interested in the problem of obtaining tracer concentration fields $c(\boldsymbol{x}, t)$ from an ensemble of trajectory positions $\{\boldsymbol{X}_t^{(i)},\ i = 1, \ldots, N\}$. This problem has been widely considered in the atmosphere-ocean science (for examples Rotach et al., 1996; de Haan, 1999; Spivakovskaya et al., 2007) and it is also an important component of operational LPDMs such as FLEXPART (for e.g. see §8 of Stohl et al., 2005).

Essentially the problem to be addressed is very similar to that of density estimation in statistics (e.g. Rosenblatt, 1956; Parzen, 1962; Scott, 2015), which uses methods of nonparametric statistics to reconstruct a sample of observed data into a probability density function (pdf). There are several methods of density estimation used in statistics that may be adapted to the atmospheric LPDMs. Traditionally, the concentration field was determined by crude box counting methods which entail counting the number of particles in a uniform rectangular volume (see Luhar and Britter, 1989; Borgas and Sawford, 1994; Rotach et al., 1996, for examples). Using any density estimation method for the concentration field can be shown to

cause either over-smoothed predictions (having a large bias) or too noisy (large variance). These effects can be minimised by increasing the number of particles N (e.g. de Haan, 1999), but with the consequential growth of computation time.

Efficiency of the density estimation problem can be significantly improved by using a more sophisticated method than the crude density estimation method above, namely the kernel density estimation (KDE, hereafter) (Silverman, 1986; Wand and Jones, 1994). Its application in atmosphere-ocean problems is not new; for examples, in idealised oceanic transport problems (Spivakovskaya et al., 2007) and in stochastic models for atmospheric meteorology (Boughton et al., 1987; Yamada and Bunker, 1988; Uliasz, 1994). The kernel density estimator works by weighting each particle by a smooth kernel function so that the probability represented by each particle becomes continuously spread out in space. The recognised multivariate kernel density estimator for a tracer concentration is given in the form of

$$\widehat{c}(\boldsymbol{x}, t; \boldsymbol{H}) = \frac{1}{N|\boldsymbol{H}|^{1/2}} \sum_{i=1}^{N} \mathcal{K}\left(\boldsymbol{H}^{-1/2}\left(\boldsymbol{x} - \boldsymbol{X}_t^{(i)}\right)\right), \tag{4.1}$$

where $\boldsymbol{H}$ is the bandwidth $(d \times d)$ matrix which is symmetric and positive definite, and d denotes the dimension. The kernel function $\mathcal{K}(\cdot) \geq 0$ satisfies

$$\int_{\mathbb{R}^d} \mathcal{K}(\boldsymbol{s})\, \mathrm{d}\boldsymbol{s} = 1.$$

Note that in general, the tracer concentration and the marginal probability density can differ by a normalisation constant. The resulting concentration estimations are only moderately sensitive to the shape of the kernel but they are critically dependent on the bandwidths. Bandwidth selection will therefore be a major theme of this chapter as the bandwidth $\boldsymbol{H}$ can be chosen to jointly minimise the bias and variance of the KDE.

The aim of the present chapter is to develop numerical strategies for an accurate

estimations of $c(\boldsymbol{x}, t)$ from the ensemble of SDE solutions of the LPDM. Specifically, more information can be obtained in a SDE problem than just a static density. We can go beyond standard KDE methods by exploiting the fact that we are solving a dynamic problem. Hence we can introduce a new class of methods, which we will call the dynamic KDE (DKDE). The starting point of DKDE is the Green's function representation of the solution to the Fokker-Planck (in this chapter, this will be the advection-diffusion equation). The Green's function for a short-time interval is then approximated by considering the leading order WKBJ series solution of the advection-diffusion equation, under the assumption that the diffusivity parameter is small (see Ottino, 1990; Balkovsky and Fouxon, 1999, for examples).

To demonstrate these methods, we will consider a model problem describing a two-dimensional advection-diffusion flow which is equivalent to a random displacement model (RDM). The model problem to be investigated is selected to highlight some keys features of observed flows in practical atmosphere-ocean fluid transport systems. An important feature is the 'chaotic advection' or Batchelor regime, i.e. the exponential divergence of nearby trajectories of the underlying deterministic flow. In this model problem, the Pèclet number Pe is relatively high and the advection-diffusion equation is solved in a periodic horizontal channel bounded by sidewalls. The flow prescribed is a uniform current superimposed a linear combination of two waves propagating with different frequencies, which has been used to explore chaotic advection in geophysical flows dominated by Rossby waves (Pierrehumbert, 1991; Haynes et al., 2007; Esler, 2015). This specific flow is also found to exhibit transport barriers that separate regions of strong mixing (see Haynes et al., 2007, for details), typically observed in geophysical flows such as stratospheric night jet, edge of polar vortices, extratropical tropopause and in oceanic current systems. Here we will consider practical quantities that correspond to weak transport across the barriers or when there is no existing formal barrier, as was recently investigated by Esler (2015) using methods of importance sampling in the stochastic model problem. Further-

more, the chosen model problem is particularly suitable for investigating methods of KDE because very high accuracy numerical solutions of the advection-diffusion equation (or the PDE solutions) are available using a relatively easy-to-implement spectral method. In more general problems, global PDE solutions are expensive to obtain and (typically) less accurate, while the Lagrangian approach will offer more benefits (see the list given in §1.1.3 for example). However in this model problem, the easily accessible PDE solutions will act to benchmark the distributions of the Lagrangian solutions, and more fundamentally to guide in the development of new KDE strategies.

The outline of this chapter is as follows. In §4.2 the model problem is described and the numerical methods for calculating the benchmark PDE solutions. The stochastic representation of the advection-diffusion is introduced as a RDM, followed by a chosen non-autonomous numerical scheme (Tocino and Ardanuy, 2002) to solve the RDM. Both PDE and RDM solutions are then presented. In §4.3 the two dimensional kernel density method by Silverman (1986) is applied to the model problem and is then reviewed by analysing the L_2-norm error results. In §4.4 a new strategy of constructing the KDE using the Green's function approximation is developed and assessed using the benchmark PDE solutions. Finally, conclusions are drawn in §4.6.

4.2 The model problem

Consider a model problem in which the evolution of the concentration of a passive tracer $c(\boldsymbol{x}, t)$ where $\boldsymbol{x} = (x, y)$ is the position vector in the two-dimensional coordinates, is described by the advection-diffusion equation,

$$\frac{\partial c}{\partial t} + (\boldsymbol{u} \cdot \nabla)\, c = \nabla \cdot (\boldsymbol{\kappa} \cdot \nabla c)\,, \tag{4.2}$$

with initial condition

$$c(\boldsymbol{x}, 0) = \exp\left(-|\boldsymbol{x} - \boldsymbol{x}_0|/W_s\right)^2, \tag{4.3}$$

where $\boldsymbol{x}_0$ is the release position and W_s is the width parameter of the initial blob. Here $\boldsymbol{u}(\boldsymbol{x}, t)$ is a given smooth incompressible velocity field and $\boldsymbol{\kappa}(\boldsymbol{x}, t)$ is a symmetric diffusivity tensor.

The domain $\mathcal{D}$ taken to be periodic in the x direction and is bounded by the sidewalls in the y direction, with dimensions $2\pi \times \pi$. No-flux boundary conditions are applied on the boundaries $\partial\mathcal{D}$ (i.e. on the sidewalls $y = 0,\ \pi$)

$$\boldsymbol{n} \cdot \boldsymbol{\kappa} \cdot \nabla c = 0, \quad \text{on} \ \ \partial\mathcal{D}. \tag{4.4}$$

The velocity field given by $\boldsymbol{u} = -\nabla \times \psi\, \mathbf{k}$ is specified by the streamfunction

$$\psi(\boldsymbol{x}, t) = -0.5y + \sin x \sin y + \epsilon \sin(x - ct) \sin 2y, \tag{4.5}$$

with the amplitude and phase speed of the second wave taken to be $\epsilon = 0.6$ and $c = 0.3$, respectively. The diffusivity tensor is given by $\boldsymbol{\kappa} = \kappa(y)\ \mathbf{I}$, where $\mathbf{I}$ is the identity matrix and

$$\kappa(y) = \kappa\,(1 + \alpha \cos 2y). \tag{4.6}$$

The specific initial condition is centred on $\boldsymbol{x}_0 = (\pi, \pi/4)^\dagger$ and with horizontal scale $W_s = 0.05$. We are interested in the behaviour at very low diffusivity $\kappa = 2 \times 10^{-4}$, which can be identified with the inverse of the flow Pèclet number $Pe = UL/K$, where U, L and K are the dimensional magnitudes for flow speed, length and diffusivity scales respectively. Hence, the Pèclet number here is large i.e. $Pe = 5000$. The relevance of this flow for large-scale transport in the atmosphere is the regime known as the chaotic advection or 'Batchelor turbulence', where the particles paths that are initially nearby each other separate exponentially in time. This phenomenon particularly applies to regions where the flow is dominated by stratification and

rotation, i.e. the large-scale flow in the troposphere and stratosphere away from the ABL and regions of active convection (Haynes, 2011).

4.2.1 Numerical discretisation

The numerical method in solving (4.2) is a standard spectral method using Fourier transform, adapted from Esler (2015) but extended here to a more general diffusion $\boldsymbol{\kappa}$. The spectral method is based on a simple spectral representation

$$c(x,y,t) = \mathrm{Re}\left(\sum_{k=-M}^{M}\sum_{l=0}^{N} A_{kl}(t)e^{ikx}\cos(ly)\right), \tag{4.7}$$

where the complex coefficients are constrained so that $\{A_{kl}\} = \{A_{kl}^*\}$, because $c(x,y,t)$ is real. Expanding the advection and diffusion terms into PDE (4.2), produces the set of linear ODEs:

$$\begin{aligned}\frac{\mathrm{d}A_{kl}}{\mathrm{d}t} &= -\frac{ik}{2}A_{kl} + \frac{k-l}{4}\left(A_{k-1,l-1} - A_{k+1,l+1}\right) + \frac{k+l}{4}\left(A_{k-1,l+1} - A_{k+1,l-1}\right)\\ &+ \frac{\epsilon(2k-l)}{4}\left(e^{-i\omega t}A_{k-1,l-2} - e^{i\omega t}A_{k+1,l+2}\right) + \frac{\epsilon(2k+l)}{4}\left(e^{-i\omega t}A_{k+1,l-2} - e^{i\omega t}A_{k+1,l-2}\right)\\ &- \kappa(k^2+l^2)A_{kl} - \frac{\kappa\alpha}{2}(k^2+l^2-2l)A_{k,l+2} - \frac{\kappa\alpha}{2}(k^2+l^2+2l)A_{k,l-2}\end{aligned} \tag{4.8}$$

for which it is understood that $A_{k,-1} = A_{k,-2} = 0$. The numerical concentration $c(x,y,t)$ can then be obtained by time-stepping the set of ODEs (4.8) using a standard fourth-order Runge-Kutta scheme. For the Pèclet number $Pe = 5000$, Esler (2015) has shown that high accuracy is possible with resolution threshold of 512×256 wavenumbers. The solution converges rapidly because the power spectrum of c decays exponentially at scales below $L_d = K/U$, hence the numerical solution is spectrally accurate provided that L_d is resolved.

The Lagrangian stochastic methods described below will be verified against the numerical concentration solution of (4.2). Very accurate solutions are not usually

available for most other problems and thus making this model an ideal test bed for the KDE methods for estimating the probability density from the Lagrangian sample solutions.

4.2.2 Stochastic representation

The Lagrangian stochastic model corresponding to (4.2) is essentially in the form of random walk model or RDM (see chapter 1.3.3 for introduction). The SDE representing this RDM is chosen in order that the probability density $p(\boldsymbol{x}, t)$ of the random variable $\boldsymbol{X}_t$ evolves in time according to the FPE that is identical to (4.2). The standard method of deriving an SDE from a given FPE (or vice versa) is outlined in §1.2.2. The SDE in the case of (4.2) is found to be

$$\mathrm{d}\boldsymbol{X}_t = (\boldsymbol{u}(\boldsymbol{X}_t, t) + \nabla \cdot \boldsymbol{\kappa}(\boldsymbol{X}_t, t))\ \mathrm{d}t + (2\boldsymbol{\kappa}(\boldsymbol{X}_t, t))^{1/2} \cdot \mathrm{d}\boldsymbol{B}_t, \quad \boldsymbol{X}_0 \sim \mathcal{N}(\boldsymbol{x_0}, W_S^2/2), \tag{4.9}$$

where $\boldsymbol{X}_t = (X_t, Y_t)$ are the stochastic vector variable explicitly, $\mathrm{d}\boldsymbol{B}_t$ are the increments of a two-dimensional Brownian (Wiener) process, and the square root of a symmetric positive-definite tensor $\boldsymbol{\kappa}$ follows the standard definition. Note that in practice, the probability density of the specified initial particle position $\boldsymbol{X}_0$ in (4.9) must be multiplied by the normalising constant πW_s^2, as $p(\boldsymbol{x}, 0) = c(\boldsymbol{x}, 0)/\pi W_s^2$. Consequently, at subsequent times the respective distributions must also be in direct proportion, i.e. $p(\boldsymbol{x}, t) = c(\boldsymbol{x}, t)/\pi W_s^2$.

The flow in (4.9) is time-dependent, and the corresponding SDE (4.9) is therefore described as non-autonomous. As a result, a more sophisticated time-stepping scheme, compared to those used in Chapter 2 is required. A suitable second-order Runge-Kutta time-stepping scheme for non-autonomous SDE (4.9) is that of Tocino and Ardanuy (2002, §6). Note that the Tocino-Ardanuy scheme (TA-RK2, hereafter) is 'weak' in the sense that it converges only in probability as time-step is

reduced, as opposed to being 'strong' in the sense of converging pathwise. The weak convergence is nevertheless appropriate for our investigation of the kernel density methods for this problem, because we are interested in convergence of the concentration field which is proportional to the pdf $p(\boldsymbol{x}, t)$. The simplified version for the implementation of their scheme in this case is detailed as follows. Denoting the drift and diffusion terms of the SDE (4.9) as $\boldsymbol{a}$ and $\boldsymbol{b}$ respectively, i.e.

$$\begin{aligned} \boldsymbol{a}(\boldsymbol{X}_n, t_n) &= \boldsymbol{u}(\boldsymbol{X}_n, t_n) + \nabla \cdot \boldsymbol{\kappa}(\boldsymbol{X}_n, t_n), \\ \boldsymbol{b}(\boldsymbol{X}_n, t_n) &= \left(2\,\boldsymbol{\kappa}(\boldsymbol{X}_n, t_n)\right)^{1/2}, \end{aligned} \tag{4.10}$$

where $\boldsymbol{X}_n \equiv \boldsymbol{X}_{t_n}$ is the stochastic variable at time $t_n = n\,\Delta t$, Δt is the time-step, the TA-RK2 is found to be

$$\begin{aligned} \boldsymbol{X}_{n+1} = \boldsymbol{X}_n &+ \frac{\Delta t}{2}\left(\boldsymbol{a}(\boldsymbol{X}_n, t_n) + \boldsymbol{a}(\boldsymbol{X}_{\mu_1}, t_n + \Delta t)\right) + \boldsymbol{R}(\boldsymbol{X}_n, t_n) \\ &+ \frac{\Delta \boldsymbol{B}_n}{2}\left(\boldsymbol{b}(\boldsymbol{X}_n, t_n) + \frac{1}{4}\,\boldsymbol{b}(\boldsymbol{X}_{\mu_1}, t_n + \Delta t) + \frac{3}{4}\,\boldsymbol{b}(\boldsymbol{X}_{\mu_2}, t_n + \Delta t)\right), \end{aligned} \tag{4.11}$$

with supporting values as intermediate steps

$$\boldsymbol{X}_{\mu_1} = \boldsymbol{X}_n + \boldsymbol{a}\,\Delta t + \boldsymbol{b}\,\Delta \boldsymbol{B}_n, \tag{4.12}$$

$$\boldsymbol{X}_{\mu_2} = \boldsymbol{X}_n + \boldsymbol{a}\,\Delta t - \tfrac{1}{3}\boldsymbol{b}\,\Delta \boldsymbol{B}_n, \tag{4.13}$$

Here N_t is the number of time-steps and $\boldsymbol{X}_n$ $(n = 1, \ldots, N_t)$ is the numerical approximation of the stochastic variable $\boldsymbol{X}(t_n)$ at $t_n = n\,\Delta t$, where $\Delta t = t/N_t$ is the time-step. $\boldsymbol{R}(\boldsymbol{X}_n, t_n) = (R_1, R_2)^\dagger$ is the remainder vector

$$\begin{pmatrix} R_1 \\ R_2 \end{pmatrix} = \begin{pmatrix} \frac{1}{2}\sqrt{2\kappa}\,\left(\sqrt{2\kappa}\right)'\left(\Delta B_n^y \Delta B_n^x - V_{12}\right) + \frac{1}{6}2\kappa\,\left(\sqrt{2\kappa}\right)''\Delta t\,\Delta B_n^x \\ \frac{1}{2}\sqrt{2\kappa}\,\left(\sqrt{2\kappa}\right)'\left(\Delta B_n^y \Delta B_n^y + V_{22}\right) \end{pmatrix}, \tag{4.14}$$

where superscript primes denote derivatives with respect to y, ΔB_n^x and ΔB_n^y are

discrete increments of the Brownian (Wiener) process in the x and y coordinate respectively. The two-point distributed random variables V_{ij} where $i, j = 1, 2$ are sampled from

$$P(V_{ij} = \Delta t) = \frac{1}{2} = P(V_{ij} = -\Delta t), \quad \text{if} \quad j > i,$$
$$\text{where} \quad V_{ii} = -\Delta t, \quad \text{and} \quad V_{ij} = -V_{ji}, \quad \text{if} \quad j > i.$$

The same boundary conditions as in (4.2) are implemented in the TA-RK2 scheme, i.e. imposing periodicity in the X_n trajectories between $X = 0$ and $X = 2\pi$, as well as perfect reflection of the Y trajectories at the side walls $Y = 0, \pi$. In comparison tests with the PDE solution (4.8), using the kernel density method described below, a time-step of $\Delta t = 10^{-3}$ was found to be adequate to ensure that the numerical error was significantly less than the statistical error when using $N = 10^5$ particles. It is immediately evident in Figure 4.1 that the scatter plot distribution of $\boldsymbol{X}_t$ follows that of $c(\boldsymbol{x}, t)$ as expected. The diffusivity parameter used in this simulation is $\alpha = 0.8$ in (4.6).

The RDM simulation only provides discrete trajectory information $\{\boldsymbol{X}_t^{(i)}\}$ (where $i = 1, \ldots, N$) which can be reconstructed to obtain their continuous probability density function using density estimation methods. The traditional density estimation method used by atmospheric modellers is the box counting method, which has normalised concentration at a specific location and time $(\boldsymbol{x}, t)$ given by

$$C(\boldsymbol{x}, t) = \frac{\pi W_s^2 N_x}{N \Delta x^2}, \tag{4.15}$$

where N_x is the number of particles in a square grid box around $\boldsymbol{x}$, N the total number of particles and Δx length of each square box. Figure 4.2 shows comparisons with the PDE solutions with the box counting reconstructions of the RDM ensemble solutions obtained from Figure 4.1. As expected, the concentrations are too noisy

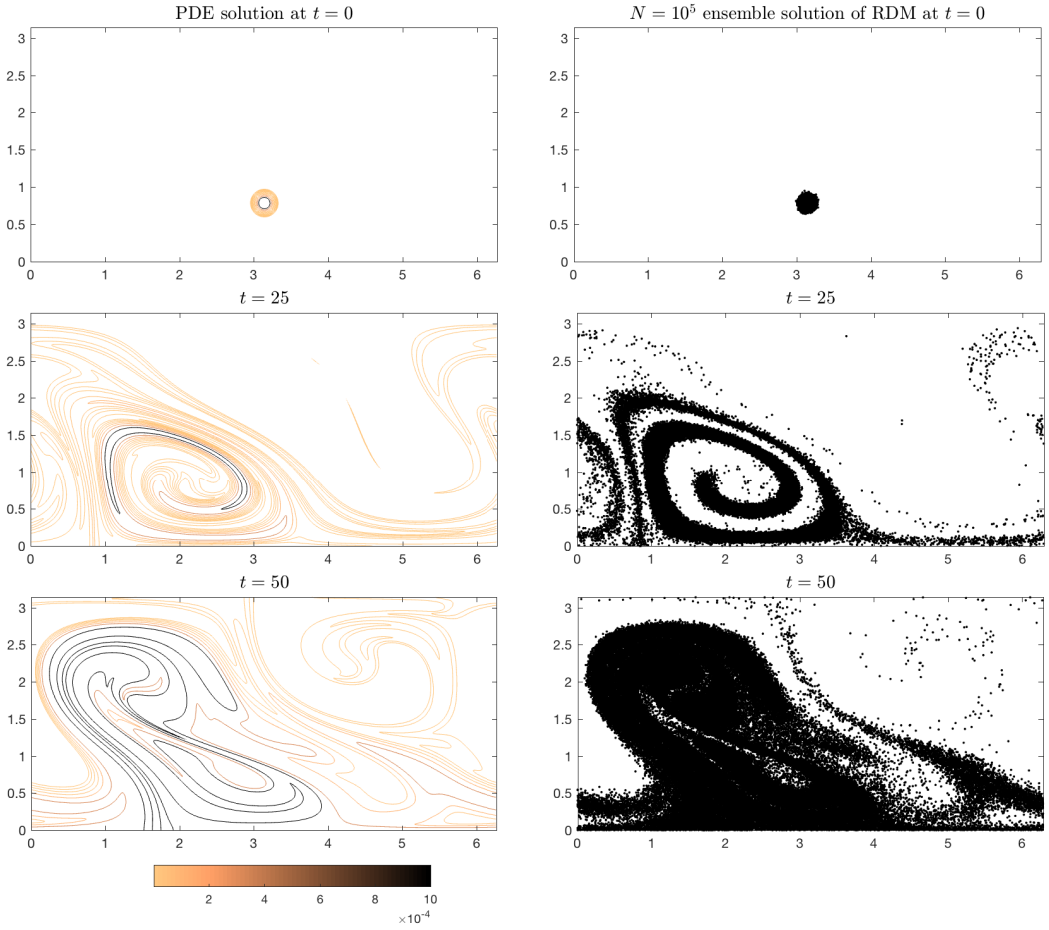

Figure 4.1: Snapshots from the PDE spectral method solution of (4.2) (left column) versus the scatterplot of $N = 10^5$ ensemble of solutions $\boldsymbol{X}_t$ of the RDM (4.9), for times $t = 0,\ 25,\ 50$. The quantity contoured for the PDE solution is $c(\boldsymbol{x}, t)$ with contour interval $10^{-0.5}$ (see colour map). The initial conditions for both solutions are sampled from the same Gaussian distribution and plotted in the top row.

and important trajectories in the centre of cloud get over-smoothed especially at $t = 50$ (bottom right panel).

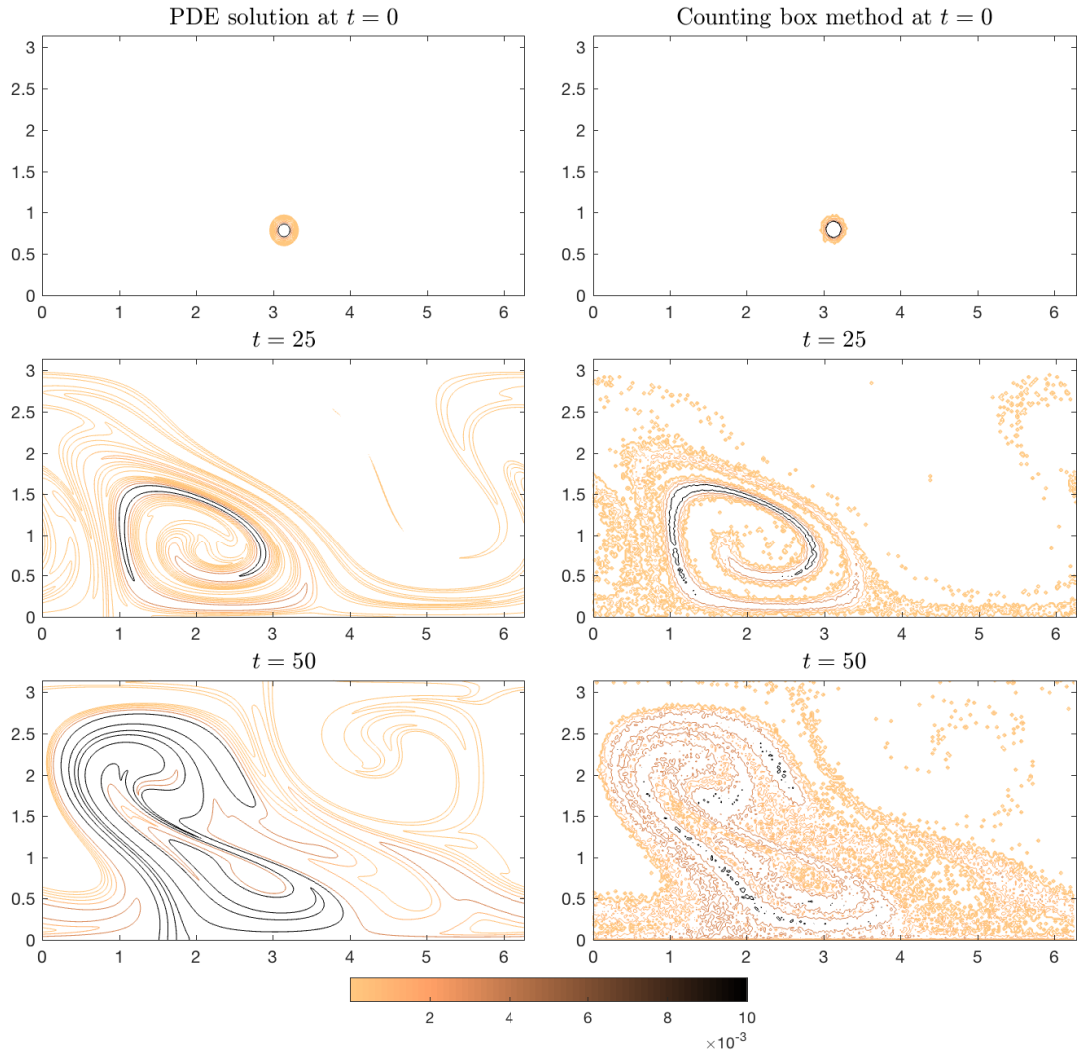

Figure 4.2: Snapshots from the PDE spectral method solution of (4.2) (left column) versus the box counting estimations (4.15) of the RDM (4.9), for times $t = 0,\ 25,\ 50$.

4.3 Kernel density estimation

As highlighted above, the density estimation method can be greatly improved by using the KDE (Silverman, 1986; Wand and Jones, 1994). The KDE spreads out

the mass of each particle across a small interval surrounding its position, thus the concentration at a given time $\widehat{c}(\boldsymbol{x}, t)$ is estimated as the sum of contributions from all the particles. As a starting point to our KDE methods for the advection-diffusion problem above, we will use circular symmetric kernels in (4.1), corresponding to the restriction

$$\boldsymbol{H} = \begin{bmatrix} h_b^2 & 0 \\ 0 & h_b^2 \end{bmatrix},$$

(see e.g. Silverman, 1986, Eq. (4.1)). The result is the single bandwidth KDE estimator

$$\widehat{c}(\boldsymbol{x}, t; h_b) = \frac{\pi W_s^2}{N h_b^2} \sum_{i=1}^{N} \mathcal{K}\left(\frac{\boldsymbol{x} - \boldsymbol{X}_t^{(i)}}{h_b}\right) + \text{ “image terms”}, \tag{4.16}$$

where “image terms” denote the reflection or images of trajectories from the boundaries and we recall that $c(\boldsymbol{x}, t) = (\pi W_s^2) \times p(\boldsymbol{x}, t)$. The (small) bandwidth $h_b > 0$ here determines the size of the kernel. Various functional forms can be chosen for the kernel $\mathcal{K}(\cdot)$, usually the kernel function is chosen to be a density function that has zero mean. A practical choice of kernel which is used throughout in this thesis is the Gaussian kernel

$$\mathcal{K}_G(\boldsymbol{x}) = (2\pi)^{-d/2} \exp\left(-\frac{1}{2}\boldsymbol{x}^T\boldsymbol{x}\right), \tag{4.17}$$

with $d = 2$ in the current application. The Gaussian kernel has the advantage of being simple to work with, but the disadvantage of not having compact support and other choices are used in applications.

4.3.1 Bandwidth selection and MISE

The main challenge in KDE is to choose the optimal bandwidth $h_b = h_*$ that will result in the most accurate reconstruction of the pdf. In order to evaluate

the accuracy of a given KDE reconstruction, it is necessary to choose a measure of error between the true value of $c(\boldsymbol{x}, t)$ and the estimator $\widehat{c}(\boldsymbol{x}, t)$. The most common measured criterion is the expectation value of $||c - \widehat{c}||_2^2$, i.e. the square of the L_2-error norm, which was first discussed in §2.4.1.3 in this thesis. In the literature of statistics (Silverman, 1986; Wand and Jones, 1994), this is often referred to as the mean integrated square error (abbreviated MISE):

$$\begin{aligned} \text{MISE}(t) &= \mathbb{E}\left(\int_{\mathcal{D}} (\widehat{c} - c)^2 \, \mathrm{d}\boldsymbol{x}\right), \\ &= \int_{\mathcal{D}} \left(\mathbb{E}\left(\widehat{c}\right) - c\right)^2 \, \mathrm{d}\boldsymbol{x} + \int_{\mathcal{D}} \text{Var}\left(\widehat{c}\right) \, \mathrm{d}\boldsymbol{x}, \end{aligned} \tag{4.18}$$

where $\mathbb{E}(\cdot)$ denotes the expectation value. In the second line, the MISE is decomposed into integrated square bias and the integrated variance following §2.3 of Wand and Jones (1994). It will be shown later that there is a trade-off: between the first and second terms of (4.18), which are known as the bias and variance respectively. The bias can be reduced at the expense of increasing the variance, and vice versa.

Numerically, we can use the definition of MISE (4.18) to determine the optimal bandwidth h_* by selecting the bandwidth that minimises the numerical MISE (or L_2-error norm, $||c - \widehat{c}||_2^2$). This is shown in Figure 4.3 in which the MISE results of the KDE reconstruction of $N = 10^6$ sized ensemble solutions from (4.9), are plotted as a function of bandwidth h_b.

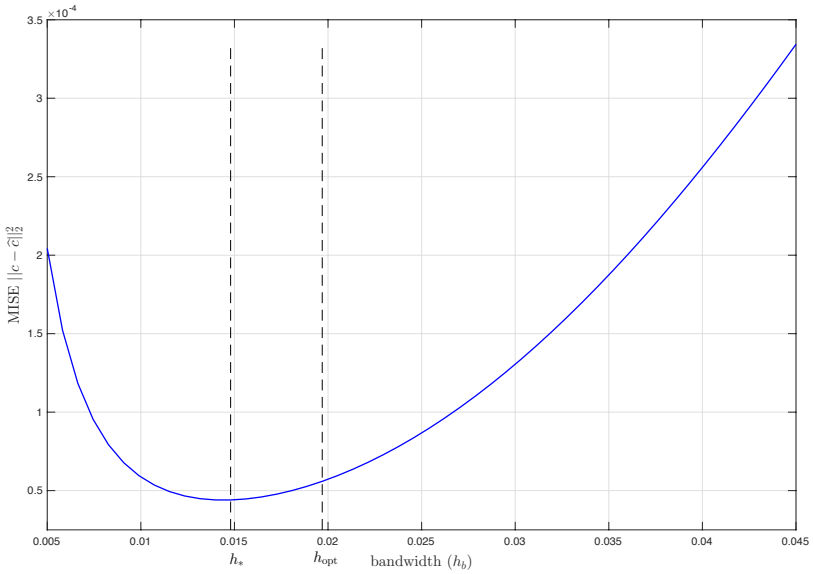

Figure 4.3: Numerical MISE (4.18) as a function of bandwidth h_b, using Silverman KDE (4.16) from a sample of $N = 10^6$ trajectory solutions of (4.9) at time $t = 50$. The black dash lines indicate the optimal bandwidth and optimal asymptotic bandwidth, h_* and h_{opt} respectively.

A lot of the literature on density estimation deal with asymptotic properties of the various methods, which can provide some intuition about the way that the methods behave and may also be of significant practical use. An asymptotic formula for the MISE, referred to as the asymptotic mean integrated square error (AMISE) and valid in the limit of small h_b, can be found as follows (e.g. Silverman, 1986, §4.3.1). The formula for AMISE in d dimensions is

$$\text{AMISE}(t) = \frac{1}{4}\, h_b^4\, \alpha_{\mathcal{K}}^2\, I + \frac{\beta_{\mathcal{K}}}{N h_b^d}, \tag{4.19}$$

$$\text{where} \quad \beta_{\mathcal{K}} = \int_{\mathcal{D}} \mathcal{K}(\boldsymbol{x})^2 \,\mathrm{d}\boldsymbol{x}, \quad \alpha_{\mathcal{K}} = \int_{\mathcal{D}} |\boldsymbol{x}|^2 \mathcal{K}(\boldsymbol{x}) \,\mathrm{d}\boldsymbol{x}.$$

Here constants $\beta_{\mathcal{K}}$ and $\alpha_{\mathcal{K}}$ are properties of the symmetric kernel function, and $I = \int_{\mathcal{D}} \left(\nabla^2 c\right)^2 \,\mathrm{d}\boldsymbol{x}$ is a functional that depends on the curvature of the true function $c(\boldsymbol{x}, t)$.

A very interesting property of (4.19) is that the integrated square bias (first

term on the right-hand side) does not depend on the sample size N directly, but does depend on the bandwidth h_b. In practice, the aim is to choose h_b as a function of N, and then the bias will depend indirectly on N via its dependence on h_b. In (4.19), the bias is asymptotically proportional to h_b^4, but taking h_b small would lead to an increase to the leading term of the integrated variance (second term) since this term is proportional to h_b^{-d}. Hence to minimise the AMISE, as $N \to \infty$ the bandwidth should vary in such a way that each component of the MISE are reduced. As pointed out above, this is known as the variance-bias trade-off.

Therefore the ideal estimate can be obtained by taking the value of h_b that minimises the AMISE expression (4.19). We refer this minimum as the asymptotically optimal bandwidth h_{opt}, which can be easily calculated by differentiating (4.19) and setting the derivative equal to zero,

$$h_{\text{opt}}^{d+4} = \frac{d\,\beta_{\mathcal{K}}}{\alpha_{\mathcal{K}}^2 N I}. \tag{4.20}$$

By inserting (4.20) into (4.19), the smallest possible AMISE for our estimation of c using a kernel function $\mathcal{K}$ is found to be

$$\begin{aligned} \min_{h_b} \text{AMISE}(t) &= c_{\mathcal{K}}\, I^{d/(d+4)} N^{-4/(d+4)}, \\ \text{where} \quad c_{\mathcal{K}} &= \left(\frac{1}{4} d^{4/(d+4)} + d^{-d/(d+4)}\right) \beta^{4/(d+4)} \alpha^{2d/(d+4)}. \end{aligned} \tag{4.21}$$

Returning to our two-dimensional advection-diffusion problem (4.2) (i.e. $d = 2$), and using the Gaussian kernel function (4.17) results in the following parameter values

$$\beta_{\mathcal{K}_G} = \frac{1}{4\pi} \quad \text{and} \quad \alpha_{\mathcal{K}_G} = 2.$$

Therefore from equations (4.20) and (4.21), the asymptotic bandwidth h_{opt} and AMISE for the estimation of the particle concentration $c(\boldsymbol{x}, t)$ in (4.2) using the

KDE (4.16) are given as follows

$$h_{\text{opt}} = (8\pi)^{-1/6} I^{-1/6}\, N^{-1/6}, \qquad \text{AMISE}(t) = \frac{3}{4}\pi^{-2/3}\, I^{1/3}\, N^{-2/3}, \tag{4.22}$$

where $I = \int_{\mathcal{D}} \left(\nabla^2 c(\boldsymbol{x}, t)\right)^2 \mathrm{d}\boldsymbol{x}$ is the measure of curvature or roughness of the function $c(\boldsymbol{x}, t)$ from (4.2). The expressions (4.22) provide the rate of convergence of the optimal bandwidth and the minimum AMISE, respectively, to zero as the sample size gets large $N \to \infty$. Under these stated assumptions, the best obtainable rate of convergence of the MISE of the KDE estimator (4.16) in $d = 2$ dimension is of order $N^{-2/3}$.

In Figure 4.3, the numerical MISE is plotted as a function of bandwidth h_b using the Silverman KDE (4.16) from the RDM ensemble solution of $N = 10^6$ at time $t = 50$. The values of optimal bandwidth $h_* = 0.0148$ obtained by minimising the numerical MISE (4.18) and the asymptotic bandwidth $h_{\text{opt}} = 0.0196$ from (4.22) are also indicated with black dashed lines. The close gap between the two optimal bandwidth values suggests that the h_{opt} formula in (4.22) can be used as a reliable guide to determine the optimal bandwidth, without repeating the KDE calculations over a range of h_b to find the minimum numerical MISE. Note that this method of selecting optimal bandwidth could be implemented for any type of model and has been used successfully in the preceding chapters, provided that a reasonable estimate of the integral I, which measures the roughness of the true function $c(\boldsymbol{x}, t)$, is available. In the current application the h_{opt} and AMISE dependence on I is rather slow, i.e. $-1/6$ and $1/3$, respectively.

Figure 4.4 shows comparisons with the PDE spectral solutions with KDE reconstructions, $\widehat{c}(\boldsymbol{x}, t, h_{\text{opt}})$ of the RDM ensemble solutions of size $N = 10^5$ generated from (4.9) at times $t = 0$ (top row), $t = 25$ (middle row) and $t = 50$ (bottom row). The contour plots show good agreement by eye, but the quality of the reconstructions may not be adequate for particular problems that require very accurate

estimates of the particle concentrations (for e.g. in importance sampling methods, Esler, 2015).

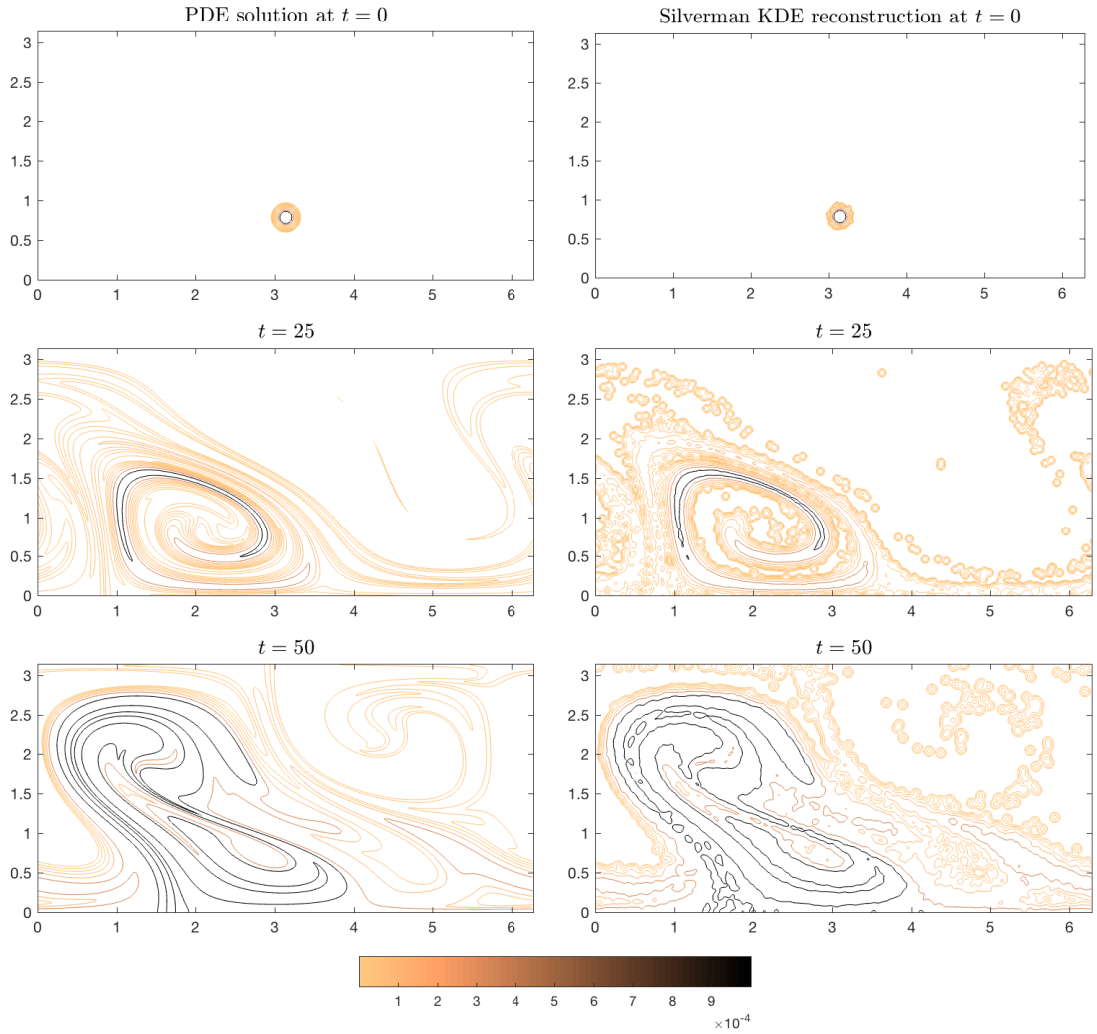

Figure 4.4: PDE solutions versus Silverman kernel density reconstructions $\widehat{c}(\boldsymbol{x}, t; h_{\text{opt}})$ from ensemble solutions of the RDM (4.9) with $N = 10^5$. The quantity contoured are $c(\boldsymbol{x}, t)$ (left column) and $\widehat{c}(\boldsymbol{x}, t; h_{\text{opt}})$ (right column), for $t = 0,\ 25,\ 50$, with contour interval $10^{-0.5}$ (see colour map).

Because the Silverman KDE (4.16) applied here use equally sized kernels in all directions, the best obtainable results can still appear too noisy or undersmoothed, especially for cases where the spread of the trajectories is much greater in one of the direction than the others. An appropriate fix for this flaw is to use kernels of

varying sizes and orientation, such as the diagonal bandwidth matrix,

$$\boldsymbol{H} = \begin{bmatrix} h_1^2 & 0 \\ 0 & h_2^2 \end{bmatrix},$$

or the full bandwidth matrix,

$$\boldsymbol{H} = \begin{bmatrix} h_1^2 & h_{12} \\ h_{12} & h_2^2 \end{bmatrix}.$$

This brings us to a new method in constructing the KDE method to follow; where the shape and size of the kernel function are determined based on approximate fundamental solutions of the PDE (4.2).

4.4 Dynamic kernel density estimation

In this section, we proceed by introducing a variant on the KDE method that exploits the fact we are solving SDEs. As a starting point, consider the well-known Green's function representation of the solution of (4.2)

$$c(\boldsymbol{x}, t) = \int_{\mathcal{D}} c(\boldsymbol{x}', t - \Delta t_1)\, G(\boldsymbol{x}, t, \boldsymbol{x}', t - \Delta t_1)\, \mathrm{d}\boldsymbol{x}', \tag{4.23}$$

where Δt_1 is small and G is the exact Green's function solution of the PDE (4.2), also known as the 'propagator' in the language of probability. G is an unknown function in $4 + 2$ dimensions. Dynamic KDE (DKDE) depends upon taking the *unbiased* infinite variance solution at $t - \Delta t_1$,

$$c(\boldsymbol{x}, t - \Delta t_1) = \frac{\pi W_s^2}{N} \sum_{i=1}^{N} \delta(\boldsymbol{x} - \boldsymbol{X}_{t-\Delta t_1}^{(i)}), \tag{4.24}$$

and then propagating forwards using an approximation to the Green's function $G_0(\boldsymbol{x}, t, \boldsymbol{X}^{(i)}_{t-\Delta t_1}, t - \Delta t_1)$. Note that by definition,

$$\mathbb{E}\delta(\boldsymbol{x} - \boldsymbol{X}^{(i)}_{t-\Delta t_1}) = p(\boldsymbol{x}, t - \Delta t_1).$$

Therefore from (4.23), the proposed DKDE is in the form

$$\begin{aligned} \widehat{C}_r(\boldsymbol{x}, t) &= \frac{\pi W_s^2}{N} \int_{\mathcal{D}} \sum_{i=1}^{N} \delta(\boldsymbol{x} - \boldsymbol{X}^{(i)}_{t-\Delta t_1})\, G_0(\boldsymbol{x}, t, \boldsymbol{x}', t - \Delta t_1)\, \mathrm{d}\boldsymbol{x}', \\ &= \frac{\pi W_s^2}{N} \sum_{i=1}^{N} G_0(\boldsymbol{x}, t, \boldsymbol{X}^{(i)}_{t-\Delta t_1}, t - \Delta t_1). \end{aligned} \tag{4.25}$$

In contrast to (4.18), the bias in (4.25) is no longer a direct consequence of smoothing by the kernel function, but is instead due to the error associated with approximating G by G_0. Here G_0 takes the role of the kernel and the bias can be written as

$$\mathbb{E}\widehat{C}_r - c = \int_{\mathcal{D}} c(\boldsymbol{x}', t - \Delta t_1)\, (G_0(\boldsymbol{x}, t, \boldsymbol{x}', t - \Delta t_1) - G(\boldsymbol{x}, t, \boldsymbol{x}', t - \Delta t_1))\, \mathrm{d}\boldsymbol{x}'. \tag{4.26}$$

The main question now is, what approximate Green's function solution G_0 do we take? The answer depends on the governing equations of the model that is being examined. In the following section, we derive the approximate G_0 from the advection-diffusion problem (4.2) introduced in this chapter.

4.4.1 Approximate Green's function in advection-diffusion

Considering the PDE of the advection-diffusion problem (4.2) and focusing on the chaotic advection regime, it is more convenient to work with the non-dimensional

equation

$$(\partial_t + \boldsymbol{u} \cdot \nabla_{\boldsymbol{x}})\, C = \epsilon\, \nabla_{\boldsymbol{x}} \cdot (\boldsymbol{\kappa} \cdot \nabla_{\boldsymbol{x}} C)\,, \quad C(\boldsymbol{x}, 0) = \delta(\boldsymbol{x} - \boldsymbol{x}_0), \tag{4.27}$$

where the parameter $\epsilon = \mathrm{Pe}^{-1} \ll 1$ is the inverse of the large Pèclet number and C is a function of the scaled coordinates $(\boldsymbol{x}, t) \to (\boldsymbol{x}, t)/\epsilon$. The aim of this section is to derive the approximate Green's function solution of the eq. (4.27), while taking advantage of the fact that $\epsilon \ll 1$. First of all note that a unique central trajectory $\tilde{\boldsymbol{x}}$ can be defined as the solution to the characteristic equation including the drift term

$$\frac{\mathrm{d}\tilde{\boldsymbol{x}}(t)}{\mathrm{d}t} = \boldsymbol{u}(\tilde{\boldsymbol{x}}, t) + \nabla_x \cdot \boldsymbol{\kappa}(\tilde{\boldsymbol{x}}, t), \quad \tilde{\boldsymbol{x}}(0) = \boldsymbol{x}_0. \tag{4.28}$$

Under the assumption that $|\boldsymbol{x} - \tilde{\boldsymbol{x}}(t)| = O(\epsilon^{1/2})$ and $t = O(1)$, the solution to PDE (4.27) in the vicinity of the central trajectory $\tilde{\boldsymbol{x}}(t)$, can be sought as a WKBJ series solution in the form

$$C = C_0(\boldsymbol{X}, t) + \epsilon^{1/2} C_1(\boldsymbol{X}, t) + \ldots, \text{ where } \boldsymbol{X} = \epsilon^{-1/2}(\boldsymbol{x} - \tilde{\boldsymbol{x}}(t)). \tag{4.29}$$

Under the change of variables it follows that

$$\nabla_x \to \epsilon^{1/2} \nabla \text{ and } \partial_t \to \partial_t - \epsilon^{-1/2} \left(\boldsymbol{u}(\tilde{\boldsymbol{x}}(t), t) + \epsilon^{-1/2} \nabla \cdot \boldsymbol{\kappa}(\tilde{\boldsymbol{x}}, t)\right) \cdot \nabla.$$

For convenience ∇ here denotes the gradient operator with respect to $\boldsymbol{X}$, and consequently eq. (4.27) becomes

$$\left(\partial_t + \epsilon^{-1/2} \left(\boldsymbol{u}(\boldsymbol{x}, t) - \boldsymbol{u}(\tilde{\boldsymbol{x}}, t)\right) \cdot \nabla\right) C = \nabla \cdot \left(\left(\boldsymbol{\kappa}(\boldsymbol{x}, t) + \epsilon^{-1} \boldsymbol{\kappa}(\tilde{\boldsymbol{x}}, t)\right) \cdot \nabla C\right). \tag{4.30}$$

Using the fact that $\epsilon \ll 1$ and $\boldsymbol{x} = \tilde{\boldsymbol{x}} + \epsilon^{1/2}\boldsymbol{X}$, we Taylor expand the velocity field $\boldsymbol{u}(\boldsymbol{x}, t)$ and the diffusion tensor $\boldsymbol{\kappa}(\boldsymbol{x}, t)$ to give

$$\begin{aligned}\boldsymbol{u}(\boldsymbol{x}, t) &= \boldsymbol{u}(\tilde{\boldsymbol{x}}, t) + \epsilon^{1/2}\left(\boldsymbol{X}\cdot\nabla\boldsymbol{u}\right)(\tilde{\boldsymbol{x}}, t) + \frac{\epsilon}{2}\left(\boldsymbol{X}\boldsymbol{X} : \nabla\nabla\boldsymbol{u}\right)(\tilde{\boldsymbol{x}}, t) + \ldots \\ \boldsymbol{\kappa}(\boldsymbol{x}, t) &= \boldsymbol{\kappa}(\tilde{\boldsymbol{x}}, t) + \epsilon^{1/2}\left(\boldsymbol{X}\cdot\nabla\boldsymbol{\kappa}\right)(\tilde{\boldsymbol{x}}, t) + \ldots\end{aligned}$$

and then inserting the series into (4.30), we obtain the following PDE at leading order $O(\epsilon^0)$,

$$\partial_t C_0 + \left(\boldsymbol{X}\cdot\boldsymbol{\Gamma}\cdot\nabla\right)C_0 - \left(\tilde{\boldsymbol{\kappa}} : \nabla\nabla C_0\right) = 0. \tag{4.31}$$

Here $\boldsymbol{\Gamma}(t)$ and $\tilde{\boldsymbol{\kappa}}(t)$ are the velocity gradient and diffusion tensor evaluated at the location of the central trajectory $\tilde{\boldsymbol{x}}$, respectively i.e.

$$\boldsymbol{\Gamma}(t) = \nabla\boldsymbol{u}(\tilde{\boldsymbol{x}}(t), t) \quad \text{and} \quad \tilde{\boldsymbol{\kappa}}(t) = \boldsymbol{\kappa}(\tilde{\boldsymbol{x}}(t), t).$$

With the solution of a diffusion equation or heat kernel in mind, we proceed by seeking a Gaussian solution for C_0 of (4.31),

$$C_0(\boldsymbol{X}, t) = \frac{1}{2\pi}|\boldsymbol{\Sigma}|^{-1/2}\,\exp\left(-\frac{1}{2}\boldsymbol{X}\cdot\boldsymbol{\Sigma}^{-1}\cdot\boldsymbol{X}\right), \tag{4.32}$$

where $\boldsymbol{\Sigma}(t)$ is the covariance matrix of the Gaussian 'blob'. In preparation for the next step, we note that

$$\begin{aligned}\partial_t\, C_0 &= -\frac{1}{2}\left(\boldsymbol{\Sigma}^{-1} : \boldsymbol{\Sigma}_t\right)C_0 - \frac{1}{2}\left(\boldsymbol{X}\cdot\boldsymbol{\Sigma}_t^{-1}\cdot\boldsymbol{\Sigma}\right)C_0, \\ \left(\boldsymbol{X}\cdot\boldsymbol{\Gamma}\cdot\nabla\right)C_0 &= -\left(\boldsymbol{X}\cdot\boldsymbol{\Gamma}\cdot\boldsymbol{\Sigma}^{-1}\cdot\boldsymbol{X}\right)C_0, \\ \left(\tilde{\boldsymbol{\kappa}} : \nabla\nabla\right)C_0 &= \left(\boldsymbol{X}\cdot\boldsymbol{\Sigma}^{-1}\cdot\tilde{\boldsymbol{\kappa}}\cdot\boldsymbol{\Sigma}^{-1}\cdot\boldsymbol{X}\right)C_0 - \left(\boldsymbol{\Sigma}^{-1} : \tilde{\boldsymbol{\kappa}}\right)C_0,\end{aligned} \tag{4.33}$$

where $\boldsymbol{\Sigma}_t$ denotes the time derivative of $\boldsymbol{\Sigma}$. Subsequently, we substitute Gaussian

solution (4.32) into (4.31) and equate the quadratic terms only to give

$$-\boldsymbol{\Sigma}_t^{-1} - \left(\boldsymbol{\Gamma}\cdot\boldsymbol{\Sigma}^{-1} + \boldsymbol{\Sigma}^{-1}\cdot\boldsymbol{\Gamma}^{\dagger}\right) - 2\,\boldsymbol{\Sigma}^{-1}\cdot\tilde{\boldsymbol{\kappa}}\cdot\boldsymbol{\Sigma}^{-1} = 0,$$

noting that $\boldsymbol{X}\cdot\boldsymbol{A}\cdot\boldsymbol{X} = 0 \implies \boldsymbol{A} + \boldsymbol{A}^{\dagger} = 0$. Upon using $\boldsymbol{\Sigma}_t^{-1} = -\boldsymbol{\Sigma}^{-1}\cdot\boldsymbol{\Sigma}_t\cdot\boldsymbol{\Sigma}^{-1}$, and pre- and post-multiplying by $\boldsymbol{\Sigma}$ gives the result

$$\frac{\mathrm{d}\boldsymbol{\Sigma}}{\mathrm{d}t} = 2\,\tilde{\boldsymbol{\kappa}} + \boldsymbol{\Sigma}\cdot\boldsymbol{\Gamma} + \boldsymbol{\Gamma}^{\dagger}\cdot\boldsymbol{\Sigma}, \qquad \boldsymbol{\Sigma}(0) = 0, \tag{4.34}$$

which is a matrix-valued ordinary differential equation (ODE) that can be simultaneously integrated with the ODE (4.28), in order to obtain a *full* covariance matrix $\boldsymbol{\Sigma}(t)$ solution. This solution will induce the elliptic shape of the Gaussian blob $C_0(\boldsymbol{X}, t)$ in (4.32) oriented in the direction of the central trajectory or characteristics solution of (4.27). The circular approximation in (4.33) leads to a simpler ODE in the form

$$\frac{\mathrm{d}\boldsymbol{\Sigma}}{\mathrm{d}t} = 2\,\tilde{\boldsymbol{\kappa}}, \tag{4.35}$$

producing a *diagonal* covariance matrix solution which will shape a circular Gaussian blob in (4.32). Figure 4.5 below shows contour plot examples of the the Gaussian blob C_0 placed as a kernel weight around one particle. The left panel illustrates the circular shaped kernel density using equation (4.35) and the elliptic shaped kernel using equation (4.34) in the right panel.

Furthermore, at the next order term in the expansion of (4.30), the equation will have the form

$$\partial_t C_1 + (\boldsymbol{X}\cdot\boldsymbol{\Gamma}\cdot\nabla)\,C_1 - (\tilde{\boldsymbol{\kappa}} : \nabla\nabla)\,C_1 = -\partial_t C_0 - \frac{1}{2}\,\boldsymbol{X}\boldsymbol{X} : \boldsymbol{\Pi}\cdot\nabla C_0 + \nabla\cdot(\boldsymbol{X}\cdot\boldsymbol{\Lambda}\cdot\nabla C_0)\,, \tag{4.36}$$

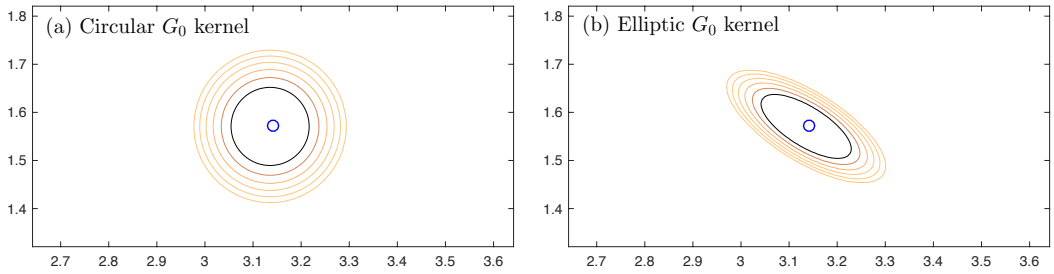

Figure 4.5: Shapes of the Green's function kernel G_0 spread on one particle. Panel (a) shows the circular kernel using (4.35) and (b) the elliptic kernel using (4.34).

where $\mathbf{\Pi}$ and $\mathbf{\Lambda}$ are the third order tensors

$$\mathbf{\Pi} = \nabla\nabla\boldsymbol{u}(\tilde{\boldsymbol{x}}, t), \quad \mathbf{\Lambda} = \nabla\boldsymbol{\kappa}(\tilde{\boldsymbol{x}}, t).$$

For the purpose of this work, we will not attempt to solve the higher order equation above but instead, we will deal with just derived key ODEs (4.28), (4.34) and (4.35) in the construction of the new DKDE (4.25), as described below.

4.4.2 DKDE algorithm

Returning to the newly proposed KDE in (4.25), we can make the approximation

$$G_0(\boldsymbol{x}, t, \boldsymbol{x}_0, t - \Delta t_1) = C_0(\boldsymbol{x} - \boldsymbol{x_0}, \Delta t_1),$$

where $\mathbf{\Sigma}(\Delta t_1)$ is the solution of (4.34) or (4.35), and $\tilde{\boldsymbol{x}}(\Delta t_1)$ the solution of (4.28). For particle concentration estimation from an ensemble solution of size N and final time $t = T$, we follow the algorithm below:

Step 1 Integrate the RDM equations (4.35) using the preferred numerical scheme for e.g. TA-RK2 (4.11) up to integration time $t = T - \Delta t_1$, and generate an

ensemble of solutions $\{\overline{\boldsymbol{X}}^{(i)}_{T-\Delta t_1}, i = 1, \ldots, N\}$.

Step 2 Integrate the following system of ODEs, using any standard integration method (e.g. fourth-order Runge-Kutta) to obtain the trajectory solution $\tilde{\boldsymbol{x}}(\Delta t_1)$ and covariance matrix $\boldsymbol{\Sigma}(\Delta t_1)$ in the short time interval $t = \Delta t_1$,

$$\frac{\mathrm{d}\tilde{\boldsymbol{x}}}{\mathrm{d}t} = \boldsymbol{u}(\tilde{\boldsymbol{x}}, t) + \nabla \cdot \boldsymbol{\kappa}(\tilde{\boldsymbol{x}}, t), \quad \tilde{\boldsymbol{x}}(0) = \overline{\boldsymbol{X}}^{(i)}_{T-\Delta t_1}, \tag{4.37a}$$

$$\begin{aligned} \frac{\mathrm{d}\boldsymbol{\Sigma}}{\mathrm{d}t} &= 2\,\boldsymbol{\kappa}(\tilde{\boldsymbol{x}}, t) + \boldsymbol{\Sigma} \cdot \boldsymbol{\Gamma} + \boldsymbol{\Gamma}^{\dagger} \cdot \boldsymbol{\Sigma}, \quad \text{(Elliptic)} \\ \text{or} \quad \frac{\mathrm{d}\boldsymbol{\Sigma}}{\mathrm{d}t} &= 2\,\boldsymbol{\kappa}(\tilde{\boldsymbol{x}}, t), \quad \text{(Circular)} \\ \text{where} \quad & \boldsymbol{\Sigma}(0) = 0. \end{aligned} \tag{4.37b}$$

Step 3 Apply the following DKDE to reconstruct the trajectory ensemble $\tilde{\boldsymbol{x}}(\Delta t_1)$ into a smooth particle concentration estimation $\widehat{C}_r$, using C_0 in (4.32) as the kernel function:

$$\begin{aligned} \widehat{C}_r(\boldsymbol{x}, T; \boldsymbol{\Sigma}) = \frac{\pi W_s^2}{2\pi N} & \left|\boldsymbol{\Sigma}(\Delta t_1)\right|^{-1/2} \\ & \times \exp\left(-\frac{1}{2}\left(\boldsymbol{x} - \tilde{\boldsymbol{x}}(\Delta t_1)\right) \cdot \boldsymbol{\Sigma}^{-1}(\Delta t_1) \cdot \left(\boldsymbol{x} - \tilde{\boldsymbol{x}}(\Delta t_1)\right)\right). \end{aligned} \tag{4.38}$$

In the algorithm steps $1 - 3$ above, the DKDE (4.38) works by spreading smooth Gaussian blobs C_0 around the particles $\tilde{\boldsymbol{x}}(\Delta t_1)$ which follow the shape and direction of trajectory information obtained from $\boldsymbol{\Sigma}$ in (4.37), to form the continuous particle concentration estimate $\widehat{C}_r(\boldsymbol{x}, T; \boldsymbol{\Sigma})$ at time T. By switching off the diffusion term in the short end time interval $[T - \Delta t_1, T]$ in step 2, the DKDE (4.38) is allowed to deterministically solve the diffusion equation in the stated time interval. More importantly, by approximating the Green's function G_0 in (4.25) with the leading order WKBJ series solution of the PDE (4.27), the bandwidth matrix $\boldsymbol{\Sigma}$ is appropriately orientated according to local trajectory of the particles. Consequently, the associated integrated bias (4.26) is expected to reduce without increasing the integrated

variance in the MISE.

4.5 Numerical results

An effective operation of the DKDE algorithm requires the selection of a large number of numerical parameters such as a sufficiently large ensemble size N, a short integration time-step Δt in the numerical scheme to attain the required level of accuracy (below the statistical error), as well as an appropriate switch time $T-\Delta t_1$ in the stochastic simulation. In the numerical result to follow, we have used numerical parameters $N = 10^6$, and $\Delta t = 10^{-3}$, at time $t = 50$. Note that the choice of Δt_1 determining the switch time in the DKDE reconstruction depends on the ensemble size N. The reason for this is that Δt_1 directly controls the size of the Gaussian kernel or bandwidth, and the optimal bandwidth depends on the number of particles N. For the purpose of presenting the new method numerically, we obtain the optimal Δt_1 for each ensemble of solutions with size N by selecting the value that minimises the numerical MISE. In future work a more detailed treatment will present a method for selecting Δt_1 in order to minimise AMISE, by analogy with methods for the optimal selection of bandwidths in KDE, discussed in §4.3.1.

The contour plots of kernel density reconstructions using the KDE, $\widehat{c}(\boldsymbol{x}, t; h_{\text{opt}})$ (4.16) and DKDE, $\widehat{C}_r(\boldsymbol{x}, t; \boldsymbol{\Sigma})$ (4.38) are compared with the PDE solution in Figure 4.6. Due to kernel weights in the DKDE reconstructions (panels (c) and (d)) having different sizes and shapes for each particle, it can be seen that the DKDE yield more continuous estimations than that of the KDE in panel (b). Moreover, the elliptic DKDE ((d)) is visually the least noisy and also appears to provide the closest estimate to the PDE solution (panel (a)) as contour lines are appropriately smoothed without masking the important trajectories.

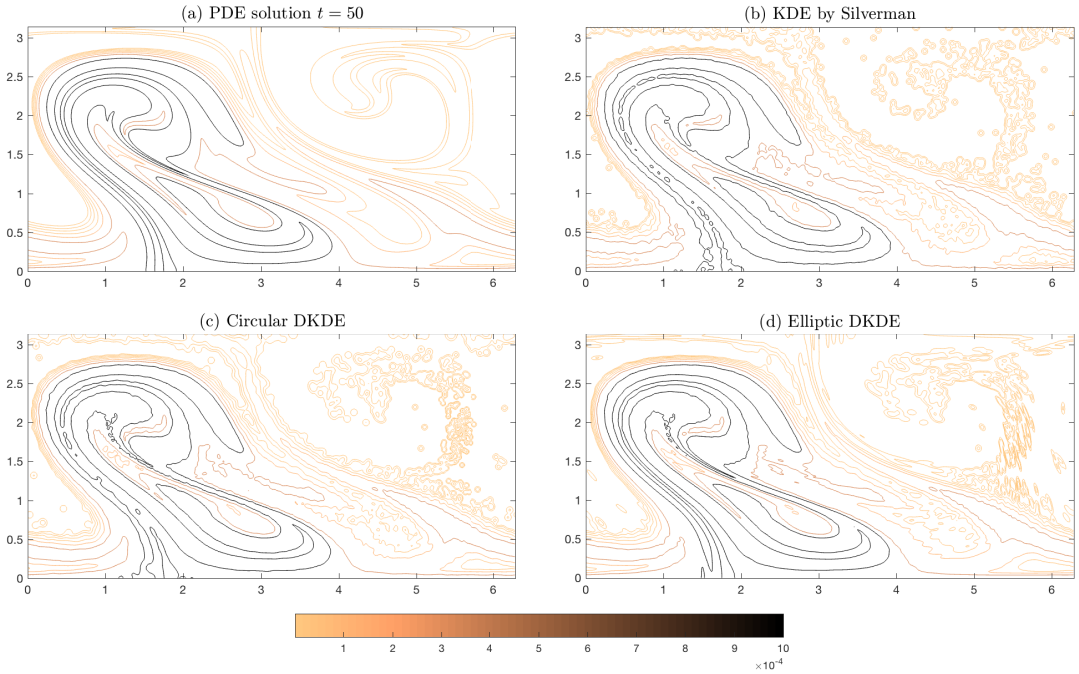

Figure 4.6: Contour plots of the benchmark PDE solution at $t = 50$ versus the kernel density reconstructions from ensembles of solutions of (4.9) with $N = 5 \times 10^5$. (a) PDE solution using the spectral method (4.8). (b) KDE using the asymptotic optimal bandwidth $\widehat{c}(\boldsymbol{x}, t; h_{\text{opt}})$ described in §4.3. (c) DKDE $\widehat{C}_r(\boldsymbol{x}, t; \boldsymbol{\Sigma})$ described in 4.4.2 using the circular kernel. (d) DKDE $\widehat{C}_r(\boldsymbol{x}, t; \boldsymbol{\Sigma})$ using the elliptic kernel.

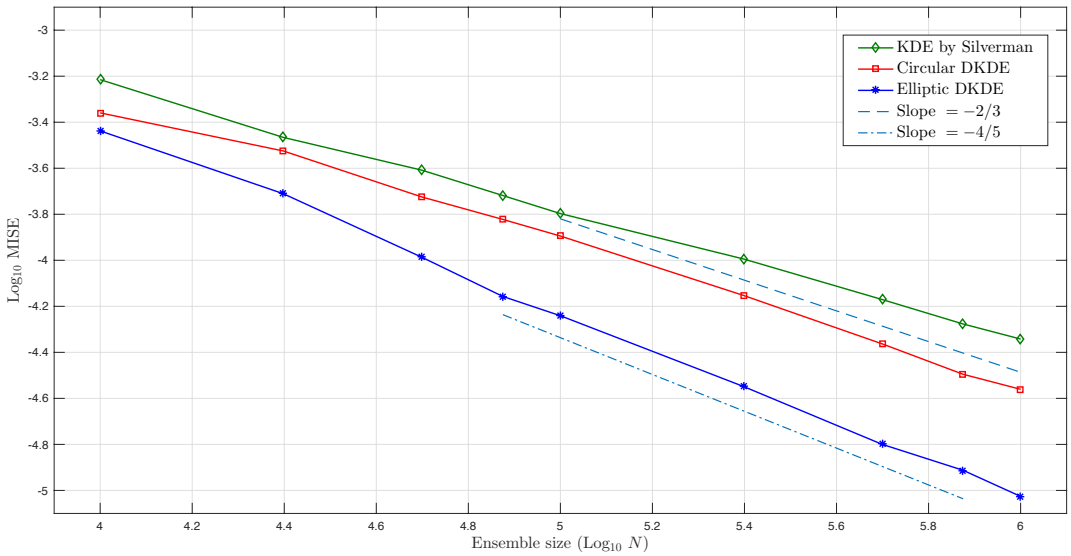

Figure 4.7: Numerical MISE (4.18) as a function of ensemble size (N) of the KDE reconstruction methods from ensembles of solutions of the RDM (4.9) at time $t = 50$.

To quantify the quality of the new estimator $\widehat{C}_r(\boldsymbol{x}, t; \boldsymbol{\Sigma})$, Figure 4.7 displays the numerical MISE (or square L_2-norm error) (4.18) of the KDE methods, calculated directly from ensembles of solution from the RDM (4.9) at $t = 50$. The MISE results are plotted as a function N, and convergence slopes are also plotted as light blue lines for reference. The DKDE reconstructions (red squares and blue stars) have MISE results significantly lower than that of the KDE (solid green diamonds), as expected from the reduced bias. Furthermore it appears that the elliptic DKDE (blue stars) has the best convergence of $\sim N^{-4/5}$, than those of the circular DKDE (red squares) and the KDE (solid green diamonds). The circular DKDE is found to attain slightly lower MISE values than KDE, but does not outperform KDE. They both converge with $\sim N^{-2/3}$. The $N^{-2/3}$ convergence for the $d = 2$ KDE is expected and discussed in (4.22).

4.6 Discussion

The focus of this chapter has been to investigate the problem of estimation of the concentration field $c(\boldsymbol{x})$ from trajectory input. Specifically, we have introduced a new methodology, the dynamic kernel density estimation (DKDE), which builds on the kernel density methods developed in statistics. The model problem examined is a two-dimensional advection-diffusion problem that is particularly relevant to the large-scale quasi-isentropic transport, typical of atmospheric and oceanic flows. We first discussed the KDE method by Silverman (1986) that applies uniform width kernels i.e. constant bandwidth in all directions, to an ensemble of RDM solutions with size N. The most convenient and reliable bandwidth selection for the KDE is to use Silverman's (1986) asymptotic analysis which states that the optimal asymptotic MISE (or square L_2-norm) has the best obtainable rate of convergence of order $N^{-2/3}$ in the two-dimensional problem. This bandwidth selection method can be easily implemented for any type of model provided that the curvature information of the true concentration is known.

We then proceeded to the main discussion of this chapter by considering the Green's function approximation solution to the advection-diffusion PDE, to construct the DKDE algorithm. The Green's function approximation method is particularly suited to the advection-diffusion in the chaotic advection regime, in which WKBJ series solutions can be sought using the small inverse of the Pèclet number i.e. $\epsilon = Pe^{-1} \ll 1$. In Figure 4.7, at $N = 10^6$ the MISE is five times lower for elliptic DKDE compared to KDE. The elliptic DKDE is also shown to have MISE convergence order of approximately 0.2 higher than those of the circular DKDE and KDE, with the last two estimators showing the same order of convergence.

There is of course plenty of room to optimise the DKDE methods, the next feasible step is to carry out the asymptotic analysis of the integrated bias (4.26) to determine the asymptotic relation between (4.26) and the bandwidth matrix.

The approximate minimum possible MISE and optimal bandwidth, as in (4.19) can then be used to provide a more sophisticated way of selecting the optimal switch time interval Δt_1. One can begin the analysis by finding the approximate properties of between the circular DKDE and the elliptic DKDE, which explicitly means substituting the G_0 in the bias equation (4.26) with the circular kernel and the Green's function solution G with the elliptic kernel. Another optimisation is to obtain a more accurate estimate of the covariance matrix $\mathbf{\Sigma}$ by solving the higher order term equation (4.36). For the interest of other researchers, we suggest using a valid methodology that has been successfully applied in the previous chapter problems, which is to seek a solution for C_1 based on a Hermite polynomial (Gram-Charlier type A) expansion

$$C_1 = \sum_{k=0}^{\infty} \mathrm{He}_k(\boldsymbol{X}; \mathbf{\Sigma})\, A_k(\tilde{\boldsymbol{x}})\, \frac{1}{2\pi|\mathbf{\Sigma}|^{1/2}}\, \exp\left(-\frac{1}{2}\boldsymbol{X}\cdot\mathbf{\Sigma}^{-1}\cdot\boldsymbol{X}\right) \tag{4.39}$$

Here $\mathrm{He}_k(\mathbf{\Sigma})$ denotes the bivariate vector (probabilists') Hermite polynimal of order k (Holmquist, 1996), defined by

$$\mathrm{He}_k(\boldsymbol{X}; \mathbf{\Sigma}) = (\phi(\boldsymbol{X}; \mathbf{\Sigma}))^{-1}\, (-1)^k\, (\mathbf{\Sigma}\cdot\nabla\boldsymbol{X})^{(k)}\, \phi(\boldsymbol{X}; \mathbf{\Sigma}),$$

where superscripts $^{(k)}$ denote the k^{th} derivative and

$$\phi(\boldsymbol{X}; \mathbf{\Sigma}) = \frac{1}{2\pi|\mathbf{\Sigma}|^{1/2}}\, \exp\left(-\frac{1}{2}\boldsymbol{X}\cdot\mathbf{\Sigma}^{-1}\cdot\boldsymbol{X}\right),$$

where $\{A_k(\tilde{\boldsymbol{x}})\}$ are sequences of functions to be determined. This definition is analogous to the definition in the univariate case (A.1).

Chapter 5

Concluding remarks and discussion

5.1 Conclusions

In this thesis we have presented several methods to investigate, assess and validate single-particle atmospheric dispersion models. The type of model that plays a central role in this thesis is the stochastic trajectory model or Lagrangian particle dispersion model (LPDM). This type of model is an invaluable tool in decision-making analysis and is often used for modelling the transport of an air pollutant in the turbulent ABL. A large part of the research that was carried out in this thesis has been focussed on the development of the random flight models (RFMs), which model the velocity field associated with turbulent eddies in the atmosphere by an Ornstein-Uhlenbeck process with a finite decorrelation time. These models are compared with their simpler diffusive approximation known as random displacement models (RDMs) that correspond to zero decorrelation time of the RFM.

In Chapter 2, we have developed a protocol for the quantitative evaluation of SDE numerical schemes, applied to the problem of dispersion in a one-dimensional

(vertical) idealised atmospheric boundary layer (ABL), modelled by RFMs. In our protocol, we have introduced a new method in solving the complementary FPE of the stochastic model, using a standard finite-difference discretisation in physical space and a Hermite function expansion in the vertical velocity space. Consequently the accurate solutions of the FPE were used to benchmark the distribution obtained from an ensemble of RFM solutions calculated using different numerical schemes with a fixed time-step. The weak convergence behaviour of solutions obtained in our model test problems was investigated, and we have found that all the schemes tested attain their formal convergence rates at early times in the model before the reflection becomes important. Thereafter, the convergence was limited to the effectiveness of the implementation of reflection boundary conditions. The best performing scheme with respect to accuracy as a function of time-step was Platen's explicit order 3.0 weak scheme. However this scheme could be computationally expensive to implement for models of higher dimensions and operationally, the use of the relatively simple "small-noise" scheme of Honeycutt was recommended instead. Legg and Raupach's "long-step" scheme (LEGGRAUP here) which is currently used for global operations was also assessed, and was found to have convergence as poor as the Euler-Maruyama scheme. This was underlined by all experiments, due to the conceptual error in its derivation, which we have corrected in the development of a new scheme named LONGSTEP. The new scheme LONGSTEP performs very well in the case of constant decorrelation time profile but no better than LEGGRAUP for other spatially varying profiles; hence we recommended that both long-step schemes to be avoided in operational use. If computational restraints require the use of moderate to long time-steps, solutions of the RDM approximation of the RFM was more accurate rather than those of the existing schemes designed for long time-steps mentioned above.

In Chapter 3, we revisited the problem of shear dispersion in the ABL to gain a better understanding of how the long-time dispersion behaviours differ between the

RFMs and RDMs. Analytical, semi-analytical and numerical results of the effective horizontal diffusivities were compared, using an interpolation parameter that generated a range of interpolation models between the RDM, RFM with profiles for stable and neutral conditions in the ABL. We found that the effective diffusivity of the more realistic RFM was slightly larger, but overall quite similar to that of the RDM. Under typical ABL conditions, evolution of the low concentrations in the tails of the tracer spreading cloud, measured by the rate function which controlled the large-deviation decay rate, were found to be quite identical between the RFMs and RDMs, except in the downstream tail regions where there are increased transport compared to the RDM. The results of Chapter 3 are interesting because they were not obvious at the outset. Our results have confirmed the RDM's capability to accurately model the late-time shear dispersion in the turbulent ABL, and therefore provided more support to the findings made in Chapter 2 suggesting that in one-dimensional problems, the simpler and easy to implement RDM can be used accurately, instead of the RFM.

In Chapter 4, the problem widely considered in many atmosphere-ocean applications, that is of converting discrete trajectory ensemble of solutions into smooth probability distributions, known as the kernel density estimation was discussed. Here we considered a two-dimensional advection-diffusion (or RDM), which was a simpler model set up than the RFM mainly focused in Chapters 2 and 3. A simple model flow, representative of large-scale chaotic advection on isentropic surfaces in the atmosphere, is investigated at high Pèclet number. This model problem was selected for the purpose of investigating methods of kernel density estimators (KDE) because accurate solutions of the advection-diffusion PDE (or FPE) used as benchmark particle concentration solutions, were easily accessible in the model set up. We emphasised the fact that the KDE by Silverman and his asymptotic analysis to obtain the optimal bandwidth was the most reliable and convenient bandwidth selection method for any type of model. In the context of the particular RDM

problem examined in Chapter 4, a new approach to construct a more accurate KDE was developed, that exploits the fact that we are solving SDEs. We called this new estimator the dynamic kernel density estimator (DKDE) and the algorithm entails a diffusion switch off period in the stochastic simulation, which itself controls the kernel's size and local orientation of the DKDE. The elliptic shaped DKDE showed squared L_2-norm error results five times lower than those of the circular shaped DKDE and the KDE by Silverman, with higher accuracy convergence as a function of number of particles.

5.2 Future research

In the first part of this thesis, the emphasis has been on the testing and evaluation of numerical schemes for RFMs modelling dispersion in the ABL, for which purpose a rigorous framework was developed in order to quantitatively assess the numerical schemes investigated. As our recommendations were based only on the limited set of schemes which we have studied, it is hoped that the newly developed protocol could provide useful insights to other researchers into developing and testing novel methods for RFMs. What still remains to be done from a practical point of view of such development is the careful treatment of reflection boundary conditions. It would be useful to verify the model's behaviour in more complex physical situations such as in the top of the convective boundary layer represented by a sharp change of turbulence strength across the interface.

With respect to shear dispersion problems in Chapter 3, the interpolation methods discussed, to obtain the analytical and semi-analytical results for the RFMs and RDMs, could prove beneficial in correcting the effective diffusivities in the RDM to be made as closely realistic as the RFM. Future work could include the effect of non-uniqueness in more than one dimensional RFMs on the long-time dispersion behaviours. Another path that could be taken is to consider the three-dimensional

dispersion in the ABL in order to understand the effect of the turning of the mean wind with height, e.g. in Ekman layers which are typically observed in neutral conditions.

The final chapter of this thesis introduces a new method of kernel density estimation, whose efficiency, as it turns out relies heavily on the switch time period in the stochastic simulation. Several improvements to this method can be tried. Most notably, the asymptotic properties of the integrated square bias in the mean integrated square error can be used as a guide in the choice of the optimal switch time interval as a function of sample size. As a starting point, an expression for the integrated bias of the circular DKDE could be derived by considering the (next order) elliptic DKDE as the exact Green's function solution in (4.26). Similarly for the approximate properties of the elliptic DKDE, the exact solution can be obtained by solving the higher order equation in the WKBJ series solution of the advection-diffusion equation. We suggest suitable solution for the higher-order term is one that has been used as a running theme in this thesis, namely to a series solution that is based on the Hermite polynomial expansion.

Appendix A

Properties of (probabilists') Hermite polynomials

In this appendix we detail some useful properties of the probabilists' Hermite polynomials $\mathrm{He}_k(\omega)$, defined by

$$\mathrm{He}_k(\omega) = (-1)^k \, \mathrm{e}^{\omega^2/2} \frac{\mathrm{d}^k}{\mathrm{d}\omega^k} \mathrm{e}^{-\omega^2/2}. \tag{A.1}$$

We concentrate on those identities necessary to derive equations (2.11) and (3.35), all can be obtained easily from results found in the classical book of Abramowitz and Stegun (1965, see Chapter 22). First, the Hermite polynomials are solutions of Hermite's equation

$$\left(\frac{\partial^2}{\partial \omega^2} - \omega \frac{\partial}{\partial \omega} \right) \mathrm{He}_k(\omega) = -k \mathrm{He}_k(\omega), \tag{A.2}$$

from which it follows that the Hermite functions satisfy

$$\left(\frac{\partial^2}{\partial \omega^2} + \omega \frac{\partial}{\partial \omega} + 1 \right) \left(\frac{\mathrm{He}_k(\omega) \mathrm{e}^{-\omega^2/2}}{\sqrt{2\pi}} \right) = -k \, \frac{\mathrm{He}_k(\omega) \mathrm{e}^{-\omega^2/2}}{\sqrt{2\pi}} \tag{A.3}$$

Second, because Hermite's equation can be written as an eigenvalue problem with a self-adjoint linear operator, the Hermite polynomials can be shown to satisfy an orthogonality relation, specifically

$$\int_{-\infty}^{\infty} \mathrm{He}_j(\omega)\mathrm{He}_k(\omega)\frac{\mathrm{e}^{-\omega^2/2}}{\sqrt{2\pi}}\mathrm{d}\omega = k!\ \delta_{jk}, \tag{A.4}$$

where δ_{jk} is the Kronecker delta. Notice that a special case of (A.4), for $j = 0$, is the integral identity

$$\int_{-\infty}^{\infty} \mathrm{He}_k(\omega)\mathrm{e}^{-\omega^2/2}\ \mathrm{d}\omega = 0, \quad (k \geq 1). \tag{A.5}$$

Thirdly and fourthly, the following differentiation and recursion relations can be obtained

$$\frac{\mathrm{d}}{\mathrm{d}\omega}\mathrm{He}_k(\omega) = k\mathrm{He}_{k-1}(\omega) \tag{A.6}$$

$$\omega\mathrm{He}_k(\omega) = \mathrm{He}_{k+1}(\omega) + k\mathrm{He}_{k-1}(\omega). \tag{A.7}$$

The results (A.3)-(A.7) are used in the derivations of (2.11) and (3.35) in this thesis.

Appendix B

Asymptotic solution of effective diffusivity

The details[1] to find effective diffusivity in the calculation of §3.3.2 are as follows. Inserting the expansion (3.28) into (3.7), at leading order in ε,

$$\mathcal{L}p_0 = \delta\left(\omega\Sigma_w p_0\right)_z + \delta(\Sigma'_w p_0)_\omega, \tag{B.1}$$

where the linear operator $\mathcal{L}$ acts on functions $f(\lambda,\omega)$ as follows

$$\mathcal{L}f \equiv T_u^{-1}\left(f_\lambda + \lambda f\right)_\lambda + T_w^{-1}\left(f_\omega + \omega f\right)_\omega . \tag{B.2}$$

The leading-order equation has the 'well-mixed' solution

$$p_0 = P(\bar{x},\bar{t})\exp\left(-\tfrac{1}{2}(\lambda^2+\omega^2)\right), \tag{B.3}$$

where $P(\bar{x},\bar{t})$ is at this order an undetermined function of the 'long' space and time variables $(\bar{x},\bar{t})$.

[1]The contents of this section are contributed by J.G. Esler.

At $O(\varepsilon)$ in the expansion

$$\mathcal{L}p_1 - \delta(\omega\Sigma_w p_1)_z - \delta(\Sigma'_w p_1)_\omega = \delta^2 u p_{0\bar{x}} + \delta\lambda\Sigma_u p_{0\bar{x}}. \tag{B.4}$$

To proceed a particular integral needs to be found for equation (B.4). A solution can be sought based on a Hermite polynomial (Gram-Charlier type A) expansion

$$p_1 = \sum_{k=0}^{\infty} \mathrm{He}_k(\omega)\Big(C_k(z) + \lambda D_k(z)\Big) P_{\bar{x}}(\bar{x},\bar{t}) \exp\left(-\tfrac{1}{2}(\lambda^2+\omega^2)\right). \tag{B.5}$$

Here $\mathrm{He}_k(\cdot)$ denotes the kth (probabilists') Hermite polynomial defined by (A.1) and the $\{C_k(z)\}$ and $\{D_k(z)\}$ are sequences of functions to be determined. In Appendix A, the leading terms in (B.4) are evaluated, and it is shown that $C_k \sim O(\delta^k)$ and $D_k \sim O(\delta^{k+1})$. Note that the full solution for p_1 also includes a complementary function, which has an identical form to the 'well-mixed' solution for p_0 given above, however it is easily shown that only the particular integral contributes to the effective diffusivity.

It is at $O(\varepsilon^2)$ in the expansion that the effective diffusivity can be calculated. The equation for p_2 is

$$\mathcal{L}p_2 - \delta(\omega\Sigma_w p_2)_z - \delta(\Sigma'_w p_2)_\omega = p_{0\bar{t}} + \delta^2 u p_{1\bar{x}} + \delta\lambda\Sigma_u p_{1\bar{x}}. \tag{B.6}$$

At this order it is not necessary to solve explicitly for p_2. Instead, the *solvability condition* of (B.6) can be used to obtain the effective horizontal diffusivity. The solvability condition is simply that the integral of the right-hand side, over the entire (λ,ω,z) domain, must be zero. That is,

$$\int_{\mathcal{D}} \left(p_{0\bar{t}} + u p_{1\bar{x}} + \delta^{-1}\lambda\Sigma_u p_{1\bar{x}}\right)\, \mathrm{d}z\, \mathrm{d}\lambda\, \mathrm{d}\omega = 0, \tag{B.7}$$

where the integral is over the domain $\{\mathcal{D} :\ (\lambda,\omega) \in \mathbb{R}^2,\ z \in [0,1]\}$. Evaluating

this integral, exploiting the orthogonality properties of the Hermite polynomials in Appendix A, the one-dimensional diffusion equation is obtained

$$P_{\bar{t}} = \kappa_{\text{eff}} P_{\bar{x}\bar{x}}, \tag{B.8}$$

where the effective diffusivity is given by

$$\begin{aligned} \kappa_{\text{eff}} &= -\left[uC_0 + \delta^{-1}\Sigma_u D_0\right] \\ &= \left[FC_0' - \delta^{-1}\Sigma_u D_0\right] \\ &= \kappa_{\text{eff}}^{(1)} + \kappa_{\text{eff}}^{(2)}. \end{aligned} \tag{B.9}$$

where, as above, square brackets denote the vertical average of a quantity over the boundary layer, and $F(z)$ is the integral of the mean wind profile as in (3.2). In direct analogy with Saffman's (1962) result (3.2), the two terms $\kappa_{\text{eff}}^{(1)}$ and $\kappa_{\text{eff}}^{(2)}$ refer to the two separate terms in the vertical average, with the much larger first term $\kappa_{\text{eff}}^{(1)}$ being due to shear dispersion, and the smaller second $\kappa_{\text{eff}}^{(2)}$ with direct horizontal diffusion.

It is evident from (B.9) that only C_0' and D_0 are needed to calculate κ_{eff}, which guides our approach to solving (B.4). First note that the boundary conditions require $C_k(0) = C_k(1) = 0$ and $D_k(0) = D_k(1) = 0$ for k odd. Inserting the expansion (B.5) into equation (B.4), the following hierarchy is obtained for the $\{C_k\}$,

$$\begin{aligned} 0 &= \delta(\Sigma_w C_1)' + \delta^2 u, && (k=0), \\ -\frac{kC_k}{T_w} &= \delta\Sigma_w C_{k-1}' + \delta(k+1)(\Sigma_w C_{k+1})', && (k \geq 1). \end{aligned} \tag{B.10}$$

The first equation can be integrated to obtain

$$C_1(z) = -\delta\Sigma_w^{-1} F(z). \tag{B.11}$$

Notice that the boundary conditions are satisfied because $F(0) = F(1) = 0$. Rearranging the $k = 1$ equation

$$\begin{aligned} C_0' &= \frac{F}{\kappa_w} - 2\frac{(\Sigma_w C_2)'}{\Sigma_w} \\ &= \frac{F}{\kappa_w} - \frac{\delta^2}{\Sigma_w}\left(\kappa_w\left(\frac{F}{\Sigma_w}\right)'\right)' + \frac{3\delta\left(\Sigma_w T_w\left(\Sigma_w C_3\right)'\right)'}{\Sigma_w}. \end{aligned} \tag{B.12}$$

where the $k = 2$ equation of (B.10) has been used to to substitute for C_2.

Inserting the above expression for C_0' into equation (B.9) for $\kappa_{\text{eff}}^{(1)}$, integrating by parts, and using the fact that $C_3(0) = C_3(1) = 0$, gives

$$\kappa_{\text{eff}}^{(1)} = \left[\frac{F^2}{\kappa_w} + \delta^2\kappa_w\left(\frac{F}{\Sigma_w}\right)'^2 + 3\delta C_3\Sigma_w\left(\frac{\kappa_w}{\Sigma_w}\left(\frac{F}{\Sigma_w}\right)'\right)'\right].$$

Using the $k = 3$ equation of (B.10) to substitute for C_3, and integrating by parts again, results in (after some working)

$$\kappa_{\text{eff}}^{(1)} = \left[\frac{F^2}{\kappa_w} + \delta^2\kappa_w\left(\frac{F}{\Sigma_w}\right)'^2 - \frac{\delta^4}{2}\kappa_w\left(\frac{\kappa_w}{\Sigma_w}\left(\frac{F}{\Sigma_w}\right)'\right)'^2\right] + O(\delta^6),$$

from which the first part of result (3.32) follows upon substitution of $\delta\Sigma_w$ for Σ_w. The explicit horizontal diffusivity $\kappa_{\text{eff}}^{(2)}$ can be handled in a similar fashion. The corresponding hierarchy is

$$\begin{aligned} -\frac{D_0}{T_u} &= \delta(\Sigma_w D_1)' + \delta\Sigma_u, && (k = 0), \\ -\frac{T_w + kT_u}{T_u T_w} D_k &= \delta\Sigma_w D_{k-1}' + \delta(k+1)(\Sigma_w D_{k+1})', && (k \geq 1). \end{aligned} \tag{B.13}$$

Following the same procedure as above

$$\begin{aligned}\kappa_{\text{eff}}^{(2)} &= -\delta^{-1}\left[\Sigma_u D_0\right] \\ &= \left[\Sigma_u^2 T_u + \Sigma_w D_1 (\Sigma_u T_u)'\right],\end{aligned}$$

where the second expression is obtained by substituting for D_0 from (B.13) and integrating by parts. It follows from the $k = 1$ equation of (B.13) that

$$\Sigma_w D_1 = \delta^2 \frac{T_u T_w}{T_u + T_w} \Sigma_w^2 (\Sigma_u T_u)' + O(\delta^4),$$

from which

$$\kappa_{\text{eff}}^{(2)} = \left[\kappa_u + \delta^2 \frac{\kappa_w T_u}{T_u + T_w} \left(\frac{\kappa_u}{\Sigma_u}\right)'^2\right] + O(\delta^4).$$

The second part of result (3.32) follows upon substitution of $\delta\sigma_i$ for Σ_i and $\delta^{-2}\tau_i$ for T_i $(i = u, w)$.

Appendix C

List of abbreviations

ABL	Atmospheric boundary layer
SDE	Stochastic differential equations
PDE	Partial differential equation
ODE	Ordinary differential equation
FPE	Fokker-Planck equation
LPDM	Lagrangian particle displacement model
RFM	Random flight model
RDM	Random displacement model
pdf	Probability density function
WMC	Well-mixed condition
DMC	Direct Monte-Carlo
GWTW	Go-with-the-winners
MISE	Mean integrated square error

AMISE	Asymptotic mean integrated square error
KDE	Kernel density estimator
DKDE	Dynamic kernel density estimator
FLEXPART	Flexible Particle Dispersion Model
NAME	Numerical Atmospheric dispersion Modelling Environment

Bibliography

M. Abramowitz and I. Stegun. *Handbook of Mathematical Functions*. Dover Publications, 1965. 1064pp.

E. Anderson, C. Bischof Z. Bai, S. Blackford, J. Demmel, J. Dongarra, J. Du Croz, A. Greenbaum, S. Hammarling, A. McKenney, and D. Sorensen. *LAPACK User's Guide*. Third Edition, SIAM Publications, Philadelphia, 1999.

D. Anfossi, G. Tinarelli, S. Trini Castelli, M. Nibart, C. Olry, and J. Commanay. A new lagrangian particle model for the simulation of dense gas dispersion. *Atmospheric Environment*, 44(6):753 – 762, 2010. doi: http://dx.doi.org/10.1016/j.atmosenv.2009.11.041.

R Aris. On the dispersion of a solute in a fluid flowing through a tube. *Proc. Roy. Soc. A.*, 235:67–77, 1956.

L Arnold. *Stochastic Differential Equations: Theory and Applications*. John Wiley and Sons, 1974.

E. Balkovsky and A. Fouxon. Universal long-time properties of Lagrangian statistics in the Batchelor regime and their application to the passive scalar problem. *Phys. Rev. E*, 60(4):4164, 1999.

G Berthet, J G Esler, and P H Haynes. A Lagrangian perspective of the tropopause

and the ventilation of the lowermost stratosphere. *J. Geophys. Res.*, 112:D18102, 2007. doi: 10.1029/2006JD008295.

M. S. Borgas and B. L. Sawford. A family of stochastic models for two-particle dispersion in isotropic homogeneous stationary turbulence. *Journal of Fluid Mechanics*, 279:69–99, 1994. ISSN 1469-7645. doi: 10.1017/S0022112094003824.

M. S. Borgas, T. K. Flesch, and B. L. Sawford. Turbulent dispersion with broken reflectional symmetry. *J. Fluid Mech.*, 332:141?156, 1997.

B. A. Boughton, J. M. Delaurentis, and W. E. Dunn. A stochastic model of particle dispersion in the atmosphere. *Boundary-Layer Meteorology*, 40(1):147–163, 1987. doi: 10.1007/BF00140073. URL `http://dx.doi.org/10.1007/BF00140073`.

G. P. Brasseur, B. Khattatov, and S. Walters. Modeling. In G. P. Brasseur, J. J. Orlando, and G. S. Tyndall, editors, *Atmospheric Chemistry and Global Change*, pages 423–462. Oxford University Press, New York, 1999.

P. M. Burrage and K. Burrage. A variable stepsize implementation for stochastic differential equations. *SIAM Journal on Scientific Computing*, 24(3):848–864, 2003.

P. M. Burrage, R. Herdiana, and K. Burrage. Adaptive stepsize based on control theory for stochastic differential equations. *Journal of Computational and Applied Mathematics*, 170(2):317 – 336, 2004. ISSN 0377-0427. doi: http://dx.doi.org/10.1016/j.cam.2004.01.027.

M. Cassiani, P. Franzese, and U. Giostra. A {PDF} micromixing model of dispersion for atmospheric flow. part ii: application to convective boundary layer. *Atmospheric Environment*, 39(8):1471 – 1479, 2005. doi: http://dx.doi.org/10.1016/j.atmosenv.2004.11.019.

M. Cassiani, A. Stohl, and J. Brioude. Lagrangian stochastic modelling of dispersion in the convective boundary layer with skewed turbulence conditions and a vertical density gradient: Formulation and implementation in the FLEXPART model. *Boundary-Layer Meteorol.*, 154:367–390, 2015.

M A Cassiani, A Stohl, and S Eckhardt. The dispersion characteristics of air pollution from the world's megacities. *Atmos. Chem. Phys.*, 13:9975–9996, 2012. doi: doi:10.5194/acp-13-9975-2013.

F. Cérou and A. Guyader. Adaptive multilevel splitting for rare event analysis. *Stochastic Analysis and Applications*, 25(2):417–443, 2007.

R. Courant, K. Friedrichs, and H. Lewy. On the partial difference equations of mathematical physics. *IBM J. Res. Dev.*, 11(2):215–234, March 1967. doi: 10.1147/rd.112.0215.

R A D'Amours, A Malo, R Servranckx, D Bensimon, S Trudel, and J-P Gauthier-Bilodeau. Application of the atmospheric lagrangian particle dispersion model mldp0 to the 2008 eruptions of okmok and kasatochi volcanoes. *J. Geophys. Res.*, 115:D00L11, 2010. doi: 10.1029/2009JD013602.

S. K. Das and P. A. Durbin. A lagrangian stochastic model for dispersion in stratified turbulence. *Physics of Fluids*, 17(2), 2005. doi: http://dx.doi.org/10.1063/1.1849184.

A. F. de Baas and I. Troen. A stochastic equation for dispersion in inhomogeneous conditions. *Physica Scripta*, 40(1):64, 1989. URL `http://stacks.iop.org/1402-4896/40/i=1/a=008`.

P. de Haan. On the use of density kernels for concentration estimations within particle and puff dispersion models. *Atmospheric Environment*, 33(13):2007 – 2021, 1999. ISSN 1352-2310. doi: http://dx.doi.org/10.1016/S1352-2310(98)00424-5.

B J Devenish, D J Thomson, F Marenco, S J Leadbetter, H Ricketts, and H F Dacre. A study of the arrival over the United Kingdom in April 2010 of the Eyjafjallajokull ash cloud using ground-based lidar and numerical simulations. *Atmos. Environ.*, 48:152–164, 2011. doi: doi:10.1016/j.atmosenv.2011.06.033.

R. R. Draxler, G. D. Hess, Air Resources Laboratory (U.S.), and Environmental Research Laboratories (U.S.). *Description of the HYSPLIT-4 Modeling System.* NOAA technical memorandum ERL ARL. National Oceanic and Atmospheric Administration, 1997.

P. A. Durbin. Stochastic differential equations and turbulent dispersion. *NASA Reference Publication*, 110:,69, 1983.

J. G. Esler. Adaptive stochastic trajectory modelling in the chaotic advection regime. *J. Fluid Mech.*, 769:1–25, 2015.

T K Flesch, J D Wilson, and E Yee. Backward-time Lagrangian stochastic dispersion models and their application to estimate gaseous emissions. *J. Appl. Meteorol.*, 34:1320–1332, 1995.

C W Gardiner. *Stochastic Methods: A Handbook for the Natural and Social Sciences.* Springer, Berlin, 4 edition, 2009. 447pp.

J. R. Garratt. *The Atmospheric Boundary Layer.* Cambridge Atmospheric and Space Science Series. Cambridge University Press, 1994.

P. Grassberger. Prune-enriched Rosenbluth method: simulations of θ polymers of chain length up to 1000000. *Phys. Rev. E*, 56:3682–3693, 1997.

P. Grassberger. Go with the winners: a general Monte-Carlo strategy. *Comp. Phys. Comm.*, 147:64–70, 2002.

S R Hanna. *Applications in air pollution modelling.* D. Reidel Publishing Company, Dordrecht, Holland, 1982.

P H Haynes. Transport and mixing of atmospheric pollutants. In H. K. Moffatt and E. F. Shuckburgh, editors, *Environmental Hazards: The Fluid Mechanics and Geophysics of Extreme Events*. World-Scientific, 2011.

P. H. Haynes and J. Vanneste. Dispersion in the large-deviation regime. Part I: shear flows and periodic flows . *J. Fluid Mech.*, 745:321–350, 2014.

P H Haynes, D Poet, and E F Shuckburgh. Transport and mixing in dynamically consistent flows. *J. Atmos. Sci.*, 64:3640–3651, 2007.

T. Hiroaki and C. Masamichi. Development of an atmospheric dispersion model for accidental discharge of radionuclides with the function of simultaneous prediction for multiple domains and its evaluation by application to the chernobyl nuclear accident. *Journal of Nuclear Science and Technology*, 45(9):920–931, 2008.

B. Holmquist. The d-variate vector hermite polynomial of order k. *Linear Algebra and its Applications*, 237:155 – 190, 1996. ISSN 0024-3795.

R. L. Honeycutt. Stochastic runge-kutta algorithms. i. white noise. *Phys. Rev. A*, 45:600–603, 1992. doi: 10.1103/PhysRevA.45.600.

F Hourdin and O Talagrand. Eulerian backtracking of atmospheric tracers. I: Adjoint derivation and parametrization of subgrid-scale transport. *Q. J. R. Meteorol. Soc.*, 132:567–583, 2006.

P. J. Hurley, W. L. Physick, and A. K. Luhar. Tapm: a practical approach to prognostic meteorological and air pollution modelling. *Environmental Modelling and Software*, 20(6):737 – 752, 2005. doi: http://dx.doi.org/10.1016/j.envsoft.2004.04.006.

K. Itô. *On Stochastic Differential Equations*. American Mathematical Society, 1951. Memoirs of the American Mathematical Society Number 4.

P James, A Stohl, C Forster, S Eckhardt, P Seibert, and A Frank. A 15-year climatology of stratosphere-troposphere exchange with a Lagrangian particle dispersion model: 1. methodology and validation. *J. Geophys. Res.*, 108:8519, doi:10.1029/2002JD002637, 2003a.

P James, A Stohl, C Forster, S Eckhardt, P Seibert, and A Frank. A 15-year climatology of stratosphere-troposphere exchange with a Lagrangian particle dispersion model: 2. Mean climate and sea- sonal variability. *J. Geophys. Res.*, 108:8522, doi:10.1029/2002JD002639, 2003b.

A R Jones, D J Thomson, M Hort, and B Devenish. The U.K. Met Office's next-generation atmospheric dispersion model, NAME III. In C Borrego and A-L Norman, editors, *Air Pollution Modelling and its Application XVII (Proceedings of the 27th NATO/CCMS International Technical Meeting on Air Pollution Modelling and its Application)*, pages pp. 580–589, Berlin, 2007. Springer.

J. C. Kaimal and J. J. Finnigan. *Atmospheric boundary layer flows: their structure and measurement*. Oxford University Press, 1994.

A.-K. Kassam and L. N. Trefethen. Fourth-order time stepping for stiff PDEs. *SIAM J. Sci. Comput*, 26:1214–1233, 2005.

P E Kloeden and E Platen. *Numerical Solution of Stochastic Differential Equations*. Springer-Verlag, Berlin, 4th edition, 1992. 636pp.

B. Langmann, A. Folch, M. Hensch, and V. Matthias. Volcanic ash over europe during the eruption of eyjafjallajökull on iceland, april-may 2010. *Atmospheric Environment*, 48:1–8, 2012.

B J Legg and M R Raupach. Markov-chain simulation of particle dispersion in inhomogeneous flows: The mean drift velocity induced by a gradient in Eulerian velocity variance. *Bound. Layer Met.*, 24:3–13, 1982.

B Legras, I Pisso, G Berthet, and F Lefevre. Variability of the Lagrangian turbulent diffusion in the lower stratosphere. *Atmos. Chem. Phys.*, 5:1605–1622, 2005.

R. B. Lehoucq, D.C. Sorensen, and C. Yang. *ARPACK Users' Guide: Solution of Large-Scale Eigenvalue Problems with Implicitly Restarted Arnoldi Methods*. SIAM Publications, Philadelphia, 1998.

J Lin, D Brunner, C Gerbig, A Stohl, A Luhar, and P Webley. *Lagrangian Modeling of the Atmosphere*. American Geophysical Union, Washington, 2013. 349pp.

J. C. Lin, C. Gerbig, S. C. Wofsy, A. E. Andrews, B. C. Daube, K. J. Davis, and C. A. Grainger. A near-field tool for simulating the upstream influence of atmospheric observations: The stochastic time-inverted lagrangian transport (stilt) model. *Journal of Geophysical Research: Atmospheres*, 108(D16):n/a–n/a, 2003. doi: 10.1029/2002JD003161.

A. K. Luhar and R. E. Britter. A random walk model for dispersion in inhomogeneous turbulence in a convective boundary layer. *Atmospheric Environment (1967)*, 23(9):1911 – 1924, 1989. ISSN 0004-6981. doi: http://dx.doi.org/10.1016/0004-6981(89)90516-7. URL `http://www.sciencedirect.com/science/article/pii/0004698189905167`.

A. J. Majda and P. R. Kramer. Simplified models for turbulent diffusion: theory, numerical modelling and physical phenomena. *Physics Reports*, 314:237, 1999.

G Maruyama. Continuous markov processes and stochastic equations. *Rend Circ Math Palermo*, 4:48–90, 1955.

G N Milstein and M V Tretyakov. *Stochastic Numerics for Mathematical Physics*. Springer Berlin Heidelberg, 2004. 594 pp.

H. Mohd. Ramli and J. G. Esler. Quantitative evaluation of numerical integration schemes for lagrangian particle dispersion models. *Geoscientific Model*

Development, 9(7):2441–2457, 2016. doi: 10.5194/gmd-9-2441-2016. URL http://www.geosci-model-dev.net/9/2441/2016/.

A. S. Monin and A. M. Yaglom. *Statistical Fluid Mechanics: Mechanics of Turbulence. : Vol.: 1.* MIT Press, 1977. URL https://books.google.co.uk/books?id=hdtTnQEACAAJ.

B Øksendal. *Stochastic Differential Equations: An introduction with applications*. Springer-Verlag, Berlin, 6th edition, 2007. 369pp.

J.M. Ottino. Mixing, chaotic advection, and turbulence. *Ann. Rev. Fluid Mech.*, 22:207, 1990.

E. Parzen. On estimation of a probability density function and mode. *The annals of mathematical statistics*, 33(3):1065–1076, 1962.

G. A. Pavliotis and A. Stuart. *Multiscale methods: averaging and homogenization*. Springer Science & Business Media, 2008.

R. T. Pierrehumbert. Chaotic mixing of tracer and vorticity by modulated travelling Rossby waves. *Geophys. Astrophys. Fluid Dyn.*, 58:285–319, 1991.

H C Rodean. *Stochastic Lagrangian Models of Turbulent Diffusion*. American Meteorological Society, Chicago, 1996. 84pp.

M. Rosenblatt. Remarks on some nonparametric estimates of a density function. *The Annals of Mathematical Statistics*, 27(3):832–837, 1956.

M. W. Rotach, S. Gryning, and C. Tassone. A two-dimensional lagrangian stochastic dispersion model for daytime conditions. *Quarterly Journal of the Royal Meteorological Society*, 122(530):367–389, 1996. ISSN 1477-870X. doi: 10.1002/qj.49712253004. URL http://dx.doi.org/10.1002/qj.49712253004.

D Ryall and R Maryon. Validation of the UK Met. Offices NAME model against the ETEX dataset. *Atmos. Environ.*, 32:42654276, 1998.

P G Saffman. The effect of wind shear on horizontal spread from an instantaneous ground source. *Q. J. Roy. Meteorol. Soc.*, 88:382–393, 1962.

B. L. Sawford. Rotation of trajectories in lagrangian stochastic models of turbulent dispersion. *Boundary-Layer Meteorology*, 93(3):411–424, 1999.

B. L. Sawford and F. M. Guest. Uniqueness and universality of Lagrangian stochastic models of turbulent dispersion. In *8th Symposium on Turbulence and Diffusion*, pages 96–99, 1988.

D. W. Scott. *Multivariate density estimation: theory, practice, and visualization*. John Wiley & Sons, 2015.

P Seibert and A Frank. Source-receptor matrix calculation with a Lagrangian particle dispersion model in backward mode. *Atmos. Chem. Phys.*, 4:51–63, 2004.

B W Silverman. *Density estimation for statistics and data analysis*. Chapman and Hall, London, UK, 1986. 176pp.

F B Smith. Role of wind shear in horizontal diffusion of ambient particles. *Q. J. Roy. Meteorol. Soc.*, 91:318–329, 1965.

R Smith. An analytical approach to shear dispersion and tracer age. *Bound. Layer Met.*, 117:383–415, 2005.

D. Spivakovskaya, A.W. Heemink, G. N. Milstein, and J.G.M. Schoenmakers. Simulation of the transport of particles in coastal waters using forward and reverse time diffusion. *Adv. Water Res.*, 28(9):927 – 938, 2005. ISSN 0309-1708. doi: http://dx.doi.org/10.1016/j.advwatres.2005.03.005. URL `http://www.sciencedirect.com/science/article/pii/S0309170805000783`.

D Spivakovskaya, A W Heemink, and E Deleersnijder. Lagrangian modelling of multi-dimensional advection-diffusion with space-varying diffusivities: theory and idealized test cases. *Ocean Dynamics*, 57:189–203, 2007.

A Stohl, M Hittenberger, and G Wotawa. Validation of the lagrangian particle dispersion model flexpart against large scale tracer experiments. *Atmos. Environ.*, 32:4245–4264, 1998.

A Stohl, C Forster, A Frank, P Seibert, and G Wotawa. Technical note: The Lagrangian particle dispersion model FLEXPART version 6.2. *Atmos. Chem. Phys.*, 5:2461–2474, 2005.

A. Stohl, J. Kim, S. Li, S. O'Doherty, J. Mhle, P. K. Salameh, T. Saito, M. K. Vollmer, D. Wan, R. F. Weiss, B. Yao, Y. Yokouchi, and L. X. Zhou. Hydrochlorofluorocarbon and hydrofluorocarbon emissions in East Asia determined by inverse modeling. *Atmos. Chem. Phys.*, 10:3545–3560, 2010.

A. Stohl, A. J. Prata, S. Eckhardt, L. Clarisse, A. Durant, S. Henne, N. I. Kristiansen, A. Minikin, U. Schumann, P. Seibert, K. Stebel, H. E. Thomas, T. Thorsteinsson, K. Tørseth, and B. Weinzierl. Determination of time- and height-resolved volcanic ash emissions and their use for quantitative ash dispersion modeling: the 2010 eyjafjallajkull eruption. *Atmospheric Chemistry and Physics*, 11(9):4333–4351, 2011. doi: 10.5194/acp-11-4333-2011.

A Stohl, P Seibert, and G Wotawa. The total release of xenon-133 from the Fukushima Dai-ichi nuclear power plant accident. *J. Environ. Radioact.*, 112: 155–159, 2012. doi: doi:10.1016/j.jenvrad.2012.06.001.

R. L. Stratonovich. *Topics in the Theory of Random Noise, vol. 2.* CRC Press, New York, 1967. translated from Russian by R. A. Solverman.

R. B. Stull. *An Introduction to Boundary Layer Meteorology*. Atmospheric Sciences Library 13. Springer Netherlands, 1 edition, 1988.

A. Szepessy, R. Tempone, and G. E. Zouraris. Adaptive weak approximation of stochastic differential equations. *Communications on Pure and Applied Mathematics*, 54(10):1169–1214, 2001.

A D Taylor. Puff growth in an Ekman layer. *J. Atmos. Sci.*, 39:837–850, 1982.

G I Taylor. Dispersion of soluble matter in solvent flowing slowly through a tube. *Proc. London Math. Soc. Ser. 2*, 20:196?211, 1921.

G I Taylor. Dispersion of soluble matter in solvent flowing slowly through a tube. *Proc. R. Soc. Lond. A*, 219:186–203, 1953.

H. Tennekes. The exponential lagrangian correlation function and turbulent diffusion in the inertial subrange. *Atmospheric Environment (1967)*, 13(11):1565–1567, 1979.

D J Thomson. Criteria for the selection of stochastic models of particle trajectories in turbulent flows. *J. Fluid Mech.*, 180:529—556, 1987.

D. J. Thomson and J. D. Wilson. *History of Lagrangian Stochastic Models for Turbulent Dispersion*, pages 19–36. American Geophysical Union, 2013. doi: 10.1029/2012GM001238.

D J Thomson, W L Physick, and R H Maryon. Treatment of interfaces in random walk dispersion models. *J. Appl. Meteor.*, 36:1284–1295, 1997.

A Tocino and R Ardanuy. Runge-Kutta methods for numerical solution of stochastic differential equations. *J. Comp. Appl. Math.*, 138:219–241, 2002.

H. Touchette. The large deviation approach to statistical mechanics. *Physics Reports*, 478(1):1–69, 2009.

J B Tyldesley and C E Wallington. Effect of wind shear and vertical diffusion on horizontal dispersion. *Q. J. Roy. Meteorol. Soc.*, 91:158–174, 1965.

M Uliasz. *Lagrangian particle modeling in mesoscale applications*, pages 71–102. Computational Mechanics Publications, Southampton, 1994.

G. K. Vallis. *Atmospheric and Oceanic Fluid Dynamics*. Cambridge University Press, Cambridge, U.K., 2006.

N G Van Kampen. *Stochastic Processes in Physics and Chemistry*. North Holland, Personal Library, 3 edition, 2007. 646pp.

M P Wand and M C Jones. *Kernel Smoothing*. Chapman and Hall, London, UK, 1994. 224pp.

J. C. Weil and R. P. Brower. An updated gaussian plume model for tall stacks. *Journal of the Air Pollution Control Association*, 34(8):818–827, 1984.

J D Wilson and T K Flesch. Flow boundaries in random flight dispersion models: enforcing the well-mixed condition. *J. Appl. Meteorol.*, 32:1695–1707, 1993.

J. D. Wilson and T. K. Flesch. Trajectory curvature as a selection criterion for valid lagrangian stochastic dispersion models. *Boundary-Layer Meteorology*, 84 (3):411–425, 1997.

J. D. Wilson and B. L. Sawford. Review of lagrangian stochastic models for trajectories in the turbulent atmosphere. *Boundary-Layer Meteorology*, 78:191–210, 1996.

J D Wilson and E Yee. A critical examination of the random displacement model of turbulent dispersion. *Bound. Layer Met.*, 125:399–416, 2007.

J D Wilson, T K Flesch, and G E Swaters. Dispersion in sheared Gaussian homogeneous turbulence. *Bound. Layer Met.*, 62:281–290, 1993.

C. S. Witham, M. C. Hort, R. Potts, R. Servranckx, P. Husson, and F. Bonnardot. Comparison of vaac atmospheric dispersion models using the 1 november 2004 grimsvötn eruption. *Meteorol. Appl.*, 14:27–38, 2007.

I. Wohltmann and M. Rex. The lagrangian chemistry and transport model atlas: validation of advective transport and mixing. *Geoscientific Model Development*, 2(2):153–173, 2009. doi: 10.5194/gmd-2-153-2009.

T. Yamada and S. Bunker. Development of a nested grid, second moment turbulence closure model and application to the 1982 ascot brush creek data simulation. *Journal of Applied Meteorology*, 27(5):562–578, 1988.